Electromagnetic Metamaterials for Antenna Applications

by

Adesoji Sajuyigbe

Department of Electrical and Computer Engineering
Duke University

Date: _____

Approved:

_____
David R. Smith, Advisor

_____
Steven A. Cummer

_____
Qing H. Liu

_____
Tuan Vo-Dinh

_____
William T. Joines

Dissertation submitted in partial fulfillment of the requirements for the degree of Doctor of Philosophy in the Department of Electrical and Computer Engineering in the Graduate School of Duke University
2010

Abstract

(Electromagnetic Metamaterials, Antennas)

Electromagnetic Metamaterials for Antenna Applications

by

Adesoji Sajuyigbe

Department of Electrical and Computer Engineering
Duke University

Date: _____

Approved:

_____
David R. Smith, Advisor

_____
Steven A. Cummer

_____
Qing H. Liu

_____
Tuan Vo-Dinh

_____
William T. Joines

An abstract of a dissertation submitted in partial fulfillment of the requirements for the degree of Doctor of Philosophy in the Department of Electrical and Computer Engineering
in the Graduate School of Duke University
2010

Abstract

This dissertation examines the use of artificial structured materials – known as metamaterials – in two antenna applications in which conventional dielectric materials are otherwise used. In the first application, the use of metamaterials to improve the impedance matching of planar phased array antennas over a broad range of scan angles is explored. A phased array antenna is composed of an array of antenna elements and enables long-distance signal propagation by directional radiation. The direction of signal propagation is defined as the scan angle. The power transmission ratio of a phased array is the ratio of the radiated power to the input power, and depends on the scan angle. The variation in the power transmission ratio is due to the different mutual coupling contributions between antenna elements at different scan angles. An optimized stack of dielectric layers, known as a wide-angle impedance matching layer (WAIM), is used to optimize the power transmission ratio profile over a broad range of scan angles. In this work, the use of metamaterials to design anisotropic WAIMs with access to a larger range of constitutive parameters – including magnetic permeability – to offer an improved power transmission ratio at a broad range of scan angles is investigated.

In the second antenna application, a strategy to create maximally transmissive and minimally reflective electromagnetic radome materials using embedded metamaterial inclusions is introduced. A radome is a covering used to protect an antenna from weather elements or provide structural function such as the prevention of aero-

dynamic drag. A radome should be made from a fully transparent and non-refractive material so that radiated fields from and to the enclosed antenna are not disrupted. The aim of this research was to demonstrate that embedded metamaterial inclusions can be used to isotropically adjust the dielectric properties of a composite material to a desired value. This strategy may lead to the creation of a structural material with electromagnetic properties close to air, thus reducing the detrimental scattering effects often associated with conventional radome materials.

Chapter 1 introduces the concept of metamaterials and discusses the use of sub-wavelength metallic structures to artificially engineer constitutive parameters such as permeability of permittivity. In Chapter 2, the analytical formulations that enable the characterization of the transmission performance of a planar phased array covered with anisotropic impedance matching layers are developed. Chapter 3 discusses the design rules that must govern the design parameters of anisotropic WAIMs realizable using metamaterials, and also presents examples of anisotropic impedance matching layers that provide a maximum power transmission ratio for most scan angles. In addition, numerical and experimental results on a metamaterial placed over a phased array are presented. In Chapter 4, the feasibility of using metamaterials to realize a minimally transparent and fully transmissive radome material is numerically investigated. In Chapter 5, experimental results that corroborate earlier numerical simulation results are analyzed.

To the one who set light into motion.

Contents

List of Tables

List of Figures

Acknowledgements

This dissertation would not be possible but for my parents, who made the brave and generous decision to send their seventeen-year-old to college in faraway America, shouldering the costs of his five undergraduate years. I am also immensely thankful to my siblings: Ṣọ́lá, Bósè, Ṣeun, Michael, and Emmanuel. Hearing the voice of family, from various locations across the vast Atlantic, has been a fuel to my energy.

I owe my deepest gratitude to several personalities that made my time at Duke much more than just about school. In the interest of brevity (which I have never been accused of) my thanks goes to the following people: Tom Hand, Ṣọ́lá Ọláọ́de, Chris Khoury, Audrey Lan, Steven Odaibo, Jeffrey Coles, Patrick Alexander, Allison Curseen, Reggie Patterson, Ayo Atewologun, Aboyewa Uduaghan, Mike Stanton, Charles Jonassaint, Ifeoma Ilo, Afabwaje Jatau, Ikwo Oboho, Kémi Adéyerí, Ufuoma Akoroda, Lánre Jimoh, Opé Johnson, Daniel Devougas, Udoka Uzoka, Meg Mahon, Scott Yuan, and many others. Your collaboration, friendship, and the many things we did together (Nigerian food and get-togethers, movies, golf, ministry nights, traveling to Europe, innumerable debates that distracted us from schoolwork, living in the same apartment, pondering aloud, laughing too loudly, eating massive Chipotle burritos on warm summer nights, et cetera.) smoothed many of grad-school's bumps. You have enriched me. One thing I am certain of is that, for me, our time in Durham will stay memorable till the day our hairs turn gray.

I am heartily thankful to Reggie and Bomi Roberson, Scott and Jennie Hawkins

of ICF, Steve and Christie Hinkle of GCF, and the endless list of solid friends I met through Cambridge Christian Fellowship at Duke. Your friendship, mentorship, and presence in my life has been like an oasis in a desert. You have been family to me.

My acknowledgement goes to several other good friends. Chigo and Ezechi Wachuku, my California family and support away from home. Ezechi: you are my brother from another mother, and I appreciate your solid support. Emeka Egwuatu, Kim Duch and Tosin Ladeinde: your unquenchable lightheartedness and friendship buffered college life in San José.

I wish to thank many of my fellow Duke research colleagues. Jonah Gollub, Ruopeng Liu, Da Huang, Bogdan Popa, Jack Mock, Jeff Allen, Aloyse Degiron, David Schurig, Vinh Nguyen, Gary Tsai, Tong Ren, Manus Ross, Stéphane Larouche, Fabrizia Ghezzo, Nathan Kundtz, Yaroslav Urzhumov and Ekaterina Pouterina: your support has catalyzed my growth as a researcher. Special thanks to Alec Rose, Nathan Kundtz and Jeff Allen for providing their help in proofreading portions of this document.

I would also like to thank Duke University for providing an environment that was conducive to having a balanced graduate school experience. Duke enabled me to broaden myself as a thinker, talker, and doer.

I am indebted to Dr. Ray Kwok of San José State Univeristy: your teaching and projects triggered in me an interest in electromagnetics.

My appreciation goes to Dr. Gary Ybarra for taking a chance by accepting me to Duke and funding my first year during which I also taught engineering and science to kids at Rogers Herr Middle School. I am grateful that through this program I became more sensitive to the many needs of the communities around me.

Also, I am highly grateful to Dr. David R. Smith, who gave me a chance to dabble, four years ago, in a project that has grown to be the chief content of this dissertation. Thank you for your support and belief in my ability.

1

Introduction to Metamaterials and its Applications

1.1 Electromagnetic Metamaterials

Electromagnetic metamaterials are artificially structured materials composed of periodic arrays of – typically resonant – subwavelength metallic structures whose electric or magnetic response provides the freedom to design dielectric or magnetic properties that might not exist in conventional materials. By changing the geometrical parameters of the constituent structure of a metamaterial, the realized dielectric or magnetic properties can be engineered. As a result, metamaterials enable the design of materials with choice electromagnetic properties.

1.1.1 What is a Material?

In the strict chemistry sense, a material is a piece of matter that is made up of a sea of periodically-arranged atoms and molecules. All materials can be classified into two categories: conductors or insulators (dielectrics). Conductors are materials that contain free charges (electrons) which move with applied current, whereas dielectrics consist of bound positive and negative charges that respond to electromagnetic fields by aligning charge pairs along the direction of the applied field. The molecular or

atomic structure of a dielectric material dictates how freely its charges will respond to an introduced electromagnetic wave. The geometrical orientation of the constituent hydrogen (positively-charged) and oxygen (negatively-charged) atoms in water, H_2O, for instance, sets up a peculiar dipolar response to any impinging electric field. The measure of the polarizability of a material to an applied electric field is known as the electric susceptibility, χ_e, while the averaged response of a sea of molecules or atoms to applied electric fields is quantified in a term known as the electric polarization vector, $\mathbf{P}$, which can be related to the permittivity of free space, ϵ_0, the applied electric field, $\mathbf{E}_a$, and the electric flux density $\mathbf{D}$, as shown in (1.1) [12]

$$\begin{aligned} \mathbf{D} &= \epsilon_0 \mathbf{E}_a + \mathbf{P} \\ \mathbf{D} &= \epsilon_0 \mathbf{E}_a + \epsilon_0 \chi_e \mathbf{E}_a \Longrightarrow \epsilon_0 (1 + \chi_e) \mathbf{E}_a \end{aligned} \tag{1.1}$$

We also proceed to define a *relative permittivity* term, ϵ_r, for any material, by rewriting $\mathbf{P}$ in terms of its relationship with the applied electric field, $\mathbf{E}_a$, and the electric susceptibility, χ_e. The permittivity of a material can be said to be a measure of how much the material 'permits' a wave to perturb its charges. In electromagnetics, ϵ_r (also known as the dielectric constant) is used to designate the averaged response of a material to applied electric fields.

$$\epsilon_r = 1 + \chi_e \tag{1.2}$$

In a similar vein, the magnetic permeability of a material is obtained from the averaged response of its sea of magnetic dipoles (very small current loops). Magnetic permeability, μ_r, is expressed in terms of magnetic susceptibility, χ_e, by

$$\mu_r = 1 + \chi_m \tag{1.3}$$

Electric permittivity and magnetic permeability are sufficient descriptors and predictors of the electromagnetic characteristics of any material, and these parameters are admissible into Maxwell's equations, the set of vector equations that govern the propagation of electromagnetic waves in space. The source-free Maxwell's equations are:

$$\begin{aligned} \nabla \times \mathbf{H} &= \epsilon \frac{\partial \mathbf{E}}{\partial t} \\ \nabla \times \mathbf{E} &= -\mu \frac{\partial \mathbf{H}}{\partial t} \\ \nabla \cdot \epsilon \mathbf{E} &= \rho \\ \nabla \cdot \mu \mathbf{H} &= 0 \end{aligned} \tag{1.4}$$

1.1.2 Metamaterials: Mimicking conventional materials

Metamaterials are designer materials that are made up of arrays of "model atoms" that can be used to generate a magnetic and/or dielectric response [13]. The electromagnetic response of atoms or molecules in conventional materials are replicated in metamaterials by using periodic arrays of small subwavelength metallic loop or wire-like structures with resistive-inductive-capacitive (RLC) properties to artificially generate a bulk electric or magnetic response. Depicted in Figure 1.1a, a simple example of one such "model atom" structure is the SRR (split ring resonator) particle initially proposed by Pendry [14]. By virtue of its geometry, the SRR possesses RLC properties: its loop possesses an intrinsic inductance and resistance, and its capacitive gap possesses a static capacitance. We know from circuit theory that an RLC circuit resonates at a frequency at which its current flow is maximum and in-phase with the applied signal. The working of an SRR is similar: the loop current induced by a piercing magnetic field is in phase with the oscillation of an applied electromagnetic field until the resonant frequency is reached, immediately beyond which the

induced loop current becomes out of phase with the increasing EM wave oscillation. The response of a large array of SRRs to an applied electromagnetic wave can be quantified and related to effective permeability by

$$\mu_{eff}(\omega) = 1 - \frac{F\omega^2}{\omega^2 - \omega_0^2 - i\omega\gamma} \tag{1.5}$$

The resonance frequency, ω_0, filling factor, F, and damping factor γ of an SRR-based metamaterial can be modified by changing the RLC and unit cell properties of the SRR, thus enabling one to engineer at will the relative permittivity, μ_{eff}, of the metamaterial at a given frequency. We must note that the engineered μ_{eff} for the discussed planar SRR particle is strictly in the direction perpendicular to the plane of the loop (i.e. $\mu_z = \mu_{eff}$, $\mu_x = 1$, $\mu_y = 1$).

We have discussed how designer materials with adjustable magnetic permeability can be created; to implement materials with adjustable dielectric properties, Pendry et al [15] introduced the idea of using arrays of thin conducting wires to create materials with a frequency dependent permittivity at microwave frequencies. As can be seen in (1.6), the frequency-dependent permittivity is chiefly dependent on the plasma frequency, ω_p, a parameter which refers to the frequency at which the permittivity changes from negative to positive. In a metal or plasma, this frequency marks the transition from opacity (below ω_p) to transparency (above ω_p). This explains why metals are opaque to light at frequencies below the ultraviolet and are transparent to light at frequencies beyond the ultraviolet (e.g. x-rays). The wire structure shown in Figure 1.1c is also considered a plasma medium (if the electric field vector is strictly along the length of the wires), with a plasma frequency that is depressed down to microwave frequencies. The plasma frequency of a wire medium can be changed by adjusting the interwire spacing and wire thickness of the constituent wire structure.

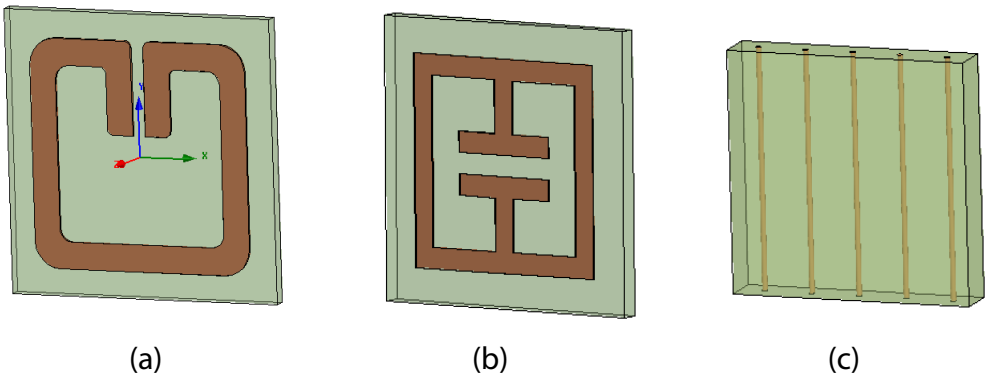

FIGURE 1.1: (a) Split ring resonator (SRR) particle (b) Electric inductive-capacitive (ELC) resonator particle (c) One-dimensional wire structure array.

$$\epsilon_{eff}(\omega) = 1 - \frac{{\omega_p}^2}{\omega^2 + i\omega\gamma} \tag{1.6}$$

Another structure that can be used to create a metamaterial that generates an electric response is the electric inductive-capacitive resonator [8], also referred to as ELC resonator for short. Depicted in Figure 1.1b, this "model atom" generates an artificially adjustable permittivity by mimicking the dipolar electric response of charge pairs. The ELC is composed of a capacitive region flanked by a pair of symmetric inductive loops. An electric field coupled to the capacitive gap region induces opposite sense currents in the loops thereby making the net magnetic response zero. Along the gap region, the electric field induces the aggregation of positive charges on one end of the gap and negative charges on the other end of the gap, thereby creating an electric dipole. The RLC characteristics of the ELC structure determines how well the charge pair around the capacitive gap oscillates in tune with an introduced electric field, the magnitude of which dictates the effective permittivity of the ELC metamaterial medium.

1.1.3 Some Recent Applications

There has probably been hundreds of proposed metamaterial applications since Pendry's SRR and wire structures were first used to create a negative index material in an experiment performed at UC-San Diego in 2000 [16]. To acquaint the reader with a representative snippet of the range of constitutive properties obtainable using metamaterials, the following will be discussed in this subsection: negative-index materials, near-zero refractive index materials, gradient-index materials, and transformation optics materials.

Negative Index Materials

In recent years, the field of metamaterials has generated a lot of interest. The prospect of obtaining a negative index of refraction, a fascinating never-before-seen property that physicists believed would enable the observation of unique phenomena not possible using conventional materials, initially fueled interest in the area of metamaterials. Veselago [17] predicted that in a negative index material (NIM), refraction would occur at negative angles [1], energy would flow in a direction opposite to the direction of wavefront propagation (phase velocity), and the doppler effect would be reversed. A negative index material can be created by combining a negative ϵ material with a negative μ material. Such a medium has been implemented with a combination magnetically resonant SRR and electrically excitable wire (or ELC) media [16] [18]. The exotic properties predicted by Veselago have indeed been experimentally observed [19–21]. Figure 1.2, for example, shows the experimentally measured fields of plane waves propagating through a positive and negative index prism respectively. It can be seen that the beam through the negative index material is bent in the a direction opposite to the beam refracted through the positive index prism.

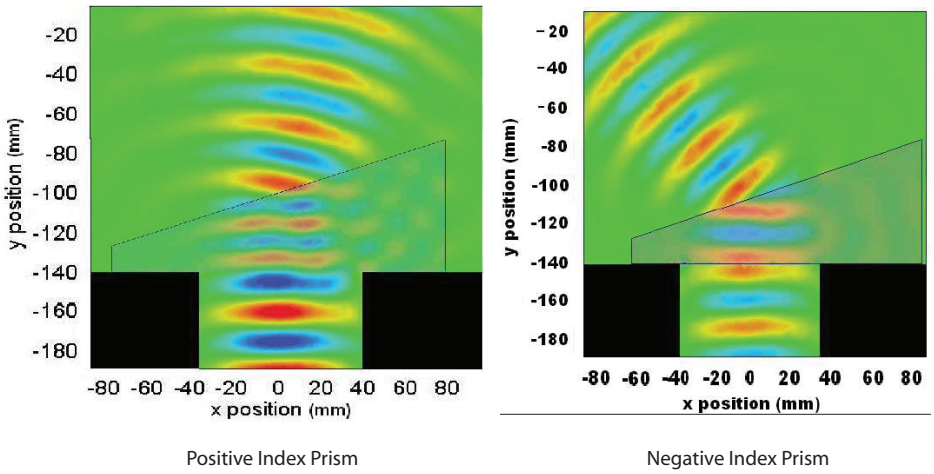

FIGURE 1.2: *(left)* Refraction through a positive index material *(right)* Refraction through a negative index material. From [1].

Near-Zero Refractive Index

One of the unusual properties achievable with the use of metamaterials is the possibility of obtaining an epsilon-near-zero (ENZ) permittivity material. The consequence of this feature is that an ENZ material would impose very little phase variation on electromagnetic waves traversing it. Silveirinha et al. [22] and Liu et al. [2] both demonstrated that ENZ materials can be used to enable wave tunneling through waveguide bends with electrically small cross-sections. Based on full wave simulations and experimental data obtained, these authors showed that electromagnetic waves introduced into an electrically small cross-section filled with ENZ material was able to fully propagate to the other side of the cross-section. Without an ENZ material filling the electrically small waveguide bend, incident fields would be perfectly reflected back to the feed.

Figure 1.4 shows a full cross-section of the experimental setup. Liu et al. designed their ENZ material by patterning complementary SRR (CSRR) structures (CSRRs are electrically resonant according to Babinet's principle [11]), which couple to out-

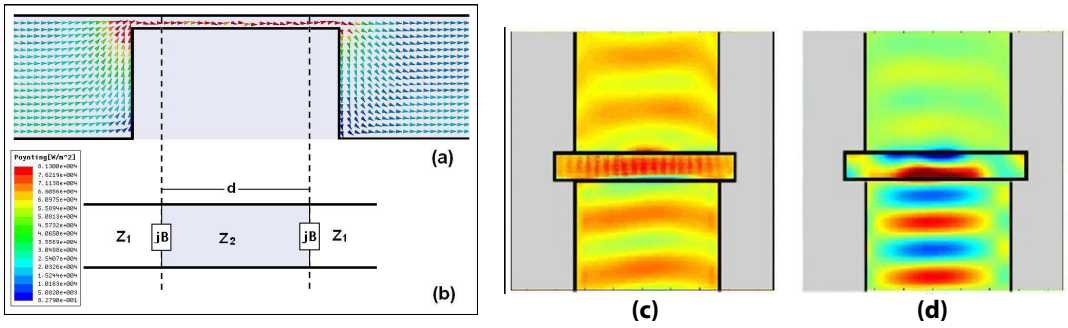

FIGURE 1.3: (a) Cross-section of parallel plate waveguide showing poynting vector squeezing through electrically small cross-section (b) Transmission line model of setup (c) Top view of spatially mapped fields tunneling fields in the presence of ENZ material (b) Top view of spatially mapped fields in the absence of ENZ material. From [2].

of-plane electric fields, onto the bottom plate of the channel. The introduction of an ENZ material sufficiently raises the characteristic impedance of the thin intervening channel, thus enabling wavefronts to squeeze through and appear on the other side of the channel.

Gradient Index Materials and Transformation Optics

One of the most celebrated applications of metamaterials has come out of the area of gradient index metamaterials and transformation optics. Gradient index metamaterials are created by designing metamaterial composites whose averaged constitutive responses vary as a function of position. This feature enables the design of metamaterials with inhomogenous permittivity and/or permeability, a feature that has proved useful in the design of quasi-optical beam deflectors, focussing lens, and transformation optics devices such as concentrators, invisibility cloaks, and so forth [4,5,23–29]. To obtain a varying index, Smith et al. [30] proposed incrementally introducing modifications to the geometrical parameters of the constituent SRR unit cells, such that the permeability of the medium, and thus its refractive index, varies linearly as a

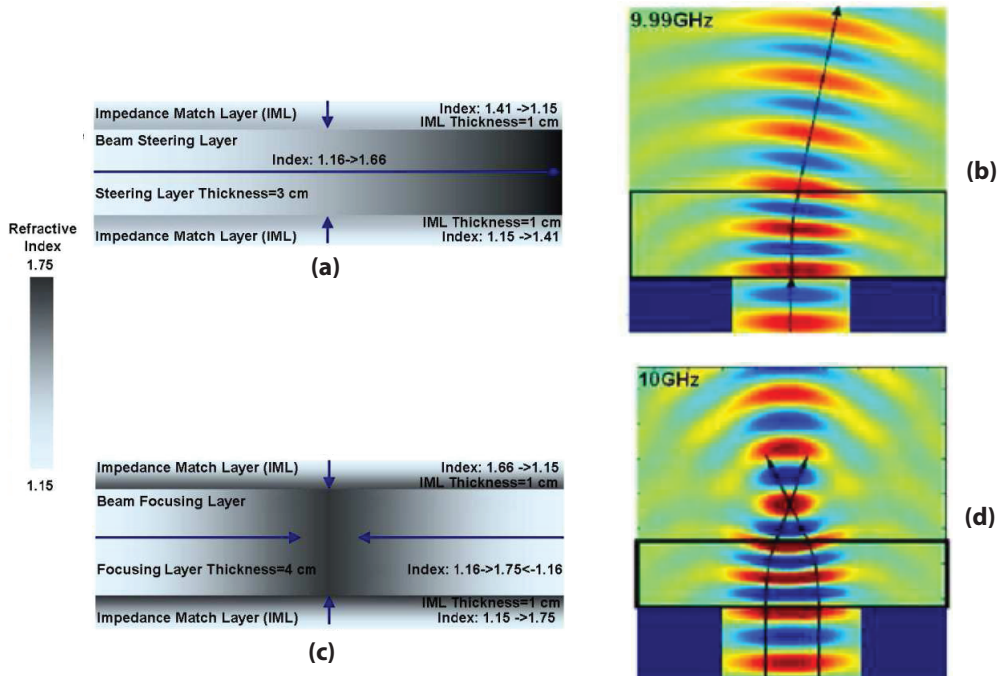

FIGURE 1.4: *Beam steering lens* (a) gradient-index distribution (b) measured spatial field distribution. *Beam focussing lens* (c) gradient-index distribution (b) measured spatial field distribution. Retrieved from [3]

function of spatial coordinates. A beam focussing lens, for example, is realized by creating a rectangular metamaterial slab with a symmetric refractive index distribution along its longitudinal axis, such that the refractive index is maximum at the center of the slab but changes (with a changing gradient) to a minimum at the longitudinal ends [3]. Similarly, a metamaterial-based beam deflector is a planar slab that, upon receiving a plane wave on one side, transmits out of its other side a deflected plane wave, so long as the index distribution of the slab varies monotonically along the longitudinal direction of the slab. Figure 1.4 shows the index distribution of both a focusing lens and beam deflector and presents the measured field distribution inside and outside each gradient index slab.

The possibility of creating materials with inhomogeneous permittivity or permeability gradients has generated interest in a new area called transformation optics.

Transformation optics is a metamaterials-inspired mathematical technique that incorporates Maxwell's equations to manipulate the flow of electromagnetic fields by transforming the grid of a region of space (and its accompanying uniform constitutive properties) into a new grid with another coordinate system (with a new set of inhomogeneous constitutive properties). For instance, a solid cylindrical region of space (occupied by air) can be transformed to a cylindrical shell, thereby creating a cylindrical "void" in its center. In Figure 1.5a), the "void" region is the inner cylinder R_1, and the shell occupies the region between R_1 and R_2. By performing the aforementioned transformation, Schurig et al. [23] experimentally demonstrated cloaking using the transformation optics technique initially proposed by Pendry et al. [31]. The shell region requires inhomogeneous material properties (spatial gradients in permittivity and permeability tensors) and was experimentally implemented using metamaterials.

As shown in Figure 1.5a, by rerouting the path of incident rays through the transformation optics media but around the inner cylindrical "void", any object placed in the "void" region is not visible to incident rays of light, thus creating an illusion of invisibility. Much like the human eye is only able to see objects based on the scattering of light rays, radars or electromagnetic detectors are only able to see objects based on the scattering profile of an object. Rerouting the trajectory of light around objects eliminates or significantly reduces scattering thereby making these objects unnoticeable to radars or electromagnetic detectors. Transformation optics materials used for this purpose are termed cloaks.

A second illustration of metamaterial-inspired cloaking is the use of a transformation optics material to hide the presence of a bump on a conducting surface. Figure 1.5b shows the scattering due to a presence of a small bump on a conducting sheet, without a cloak covering. It can be seen that the curvature of the small bump causes incident light rays to scatter off to different directions, whereas without the bump

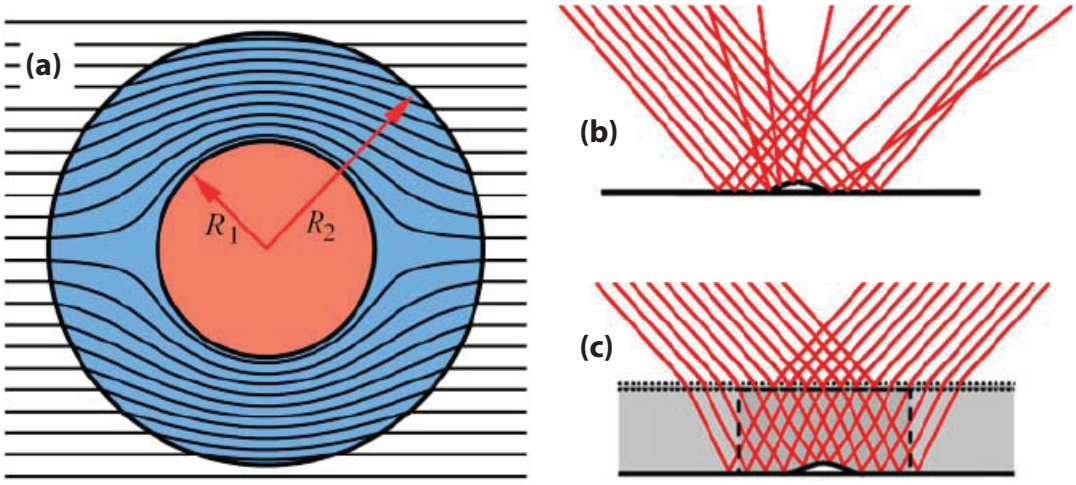

FIGURE 1.5: (a) Ray-traced fields propagating through cloak material around concealed cylinder. (b) Ray-traced fields reflected off a conducting sheet with bump. (c)Ray-traced fields reflected off a conducting sheet with cloak covering bump. Adapted from [4, 5]

the incident rays would scatter symmetrically. The shaded region of free space delimited by dashed lines in Figure 1.5c is transformed to have new spatial and material properties such that light rays introduced to the region would exhibit the scattering properties of a flat conducting sheet, as a result concealing the bump. Experimental results demonstrating the use of a metamaterial cloak to conceal a bump on a conducting sheet have been reported [5].

Transformation optics and graded-index techniques have given rise to the development of a new class of structures which have been used to design devices such as beam splitters/shifters [32], concentrators [33], and so forth [34] [35] [36].

The range of metamaterial applications thus far discussed exemplifies some of the ways in which metamaterial designs can be used to achieve structured materials with loosened ϵ and μ constitutive properties.

In this dissertation, two engineering applications, in which metamaterials may provide the opportunity for an improved performance, are explored. The unifying

theme of the research work in this dissertation is to examine the utility of incorporating the use of metamaterials into devices for which a conventional dielectric would otherwise be used. The first application is the phased array antenna, in which a stack of dielectric layers is used for impedance matching purposes; the second is the electromagnetic radome, which are structures – made from electromagnetically transparent materials, often dielectrics – used to cover antennas for protection against the adverse effects of weather or other environmental elements.

1.2 Dissertation Work: Engineering Applications of Metamaterials

1.2.1 Phased Array Antennas

Phased array antennas provide the advantage of enabling long-distance signal propagation by directionally radiating power. Composed of a periodic arrangement of closely-spaced identical antenna elements, a phased array antenna (henceforth referred to as "phased array" or "array") produces a highly directional radiation that is electronically steered by changing the phase gradient across the array of elements. Phased arrays are very useful in several communication systems applications because, given their capability to bundle and rapidly steer electromagnetic radiation, they can be used to transmit information over longer distances than other antenna configurations.

Ideally, an electronically-steered phased array antenna would radiate the same amount of power irrespective of the steer angle. In reality however, due to different mutual coupling contributions between phased array antenna elements at different scan (steer) angles [37], the power radiated as a function of scan varies, sometimes to extreme values [38]. Mutual coupling occurs because individual antenna elements are closely spaced, which is a necessity in order to generate one highly directional beam. One approach to mitigate this effect is to place layers of dielectric materials on the array surface in order to match the impedance of the array to free space over as

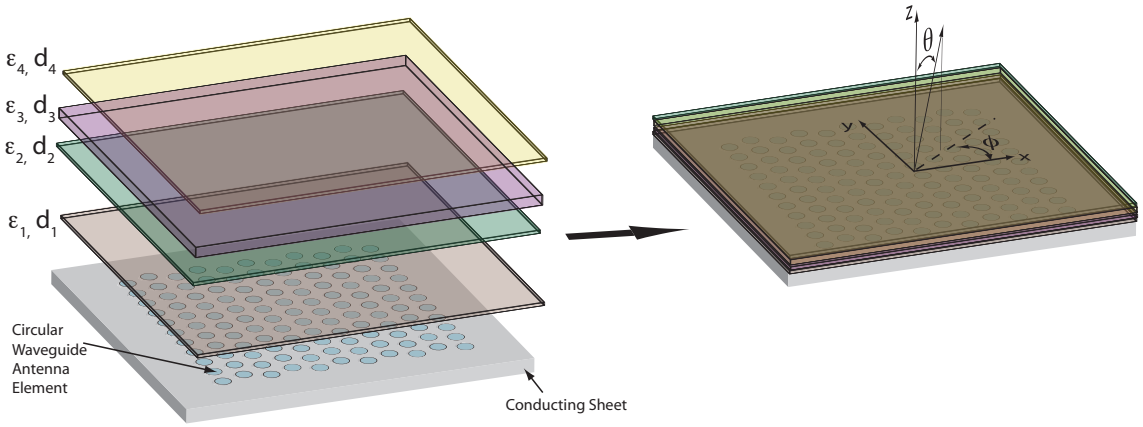

FIGURE 1.6: Planar phased array consisting of circular waveguide antenna elements *(left)* before placement of WAIMs. *(right)* with stack of dielectric WAIM layers flush with array surface.

large a range of scan angles as possible [39]. The optimized stack of dielectric layers is referred to as a wide-angle impedance match (WAIM) layer. Figure 1.6 shows a rendering of the placement of dielectric WAIM layers over a planar phased array antenna composed of circular waveguide elements openings cut out of a conducting material.

WAIM structures formed from layers of dielectric materials have proved beneficial in addressing the impedance mismatch associated with phased array antennas. However, given that available materials exhibit a fairly restricted range of dielectric constants, it might be expected that access to a larger range of constitutive properties—including magnetic permeability values—would offer further advantages for the design of WAIM layers.

Metamaterials, or structured materials, have the advantage that they can be designed with permittivity and permeability values over a continuum of values [14, 15], and provides access to material properties such as anisotropy that are typically not readily available in most usable WAIM dielectric materials. This greater freedom po-

tentially presents opportunities to obtain more comprehensive impedance matching for phased array antennas; heuristically, anisotropic materials, implementable using metamaterials, should improve the ease of matching array antennas over a broader range of scan angles.

In this dissertation, the concept of using anisotropic materials – by which metamaterials can be described – as wide angle impedance matching layers is introduced. First, analytical formulations to describe the performance of a phased array in the presence of an anisotropic layer are developed, then an optimization is performed to prescribe anisotropic material properties to match the power transmission performance of the array over a broad range of scan angles. Thereafter, a numerical and experimental investigation is performed to confirm that metamaterials can be modeled as an equivalent anisotropic continuous material when placed over the surface of a phased array antenna.

1.2.2 Antenna Enclosures: Electromagnetic Radomes

An electromagnetic radome is a covering to protect an antenna from potentially detrimental elements such as wind perturbations, aerodynamic drag, and so forth. Radome are typically made from dielectric materials. In order to not disrupt radiated fields from and to the enclosed antenna, a radome, ideally, should be made from a fully transparent and non-refractive material. Since radomes and other structures that enclose radiating systems are designed for their mechanical integrity, they are usually made from ceramics or composites that have inherently high dielectric values [40]. Due to differences in curvature between the inner and outer surfaces of radomes, refraction in radome materials introduces deflections to exiting local plane waves. Boresight error [40] [41] is a quantitative measure of such deflections.

A radome is non-refractive when its index is matched to air (n_{radome}=n_{air}) and is fully transparent when impedance-matched to air (Z_{radome}=Z_{air}). To exhibit both

characteristics, the radome material would need to be impedance-matched and index-matched to free space for all angles of TE and TM-polarized local plane wave incidence. From an electromagnetic standpoint, the solution to this problem is trivial: make the radome out of air. Since such a solution precludes the presence of an actual radome, a more practical solution is necessary.

Radomes are made from a limited range of dielectric materials because mechanical viability is a chief desired feature. Typically, the thickness of the radome dielectric is adjusted so that it is perfectly impedance-matched (Fabry-Perot resonance) at a certain angle of incidence and acceptably matched at other angles. Index matching is thus traded off for impedance matching thereby resulting in a highly transmissive radome with boresight error features.

In this dissertation, a technique to obtain strongly transmissive and minimally refractive radome materials is numerically and experimentally investigated. This concept is actualized by embedding electrically resonant metamaterial particles inside a host dielectric, so that the permittivity of the composite material can be depressed to close to unity (n_{air}=1) in several directions of TE and TM-polarized local plane wave incidence. The aim of this strategy is to create a structural material with electromagnetic properties close to air, thus reducing the detrimental scattering effects associated with radome materials. A numerical and experimental study on the proposed metamaterial composite, composed of embedded inclusions termed three-dimensionalized electric-inductive-capacitive resonators, was performed to analyze its overall properties over a range of plane wave incidence angles and TE and TM polarizations.

1.3 Contributions of this Dissertation

By developing analytical formulations to describe the performance of phased array antennas in the presence of anisotropic impedance matching layers, and perform-

ing quasi-analytical, numerical and experimental studies on the feasibility of using metamaterials to implement homogenous anisotropic impedance matching materials, this dissertation has contributed to the foundational work in the area of phased array antenna impedance matching using anisotropic materials and/or metamaterials. Further, through the use of a three-dimensionally-resonant electric particle, this dissertation proposes a strategy in which embedded inclusions may be used to enable the creation of strongly transparent and minimally refractive antenna coverings, thus preventing refractive errors and reflections by depressing the refractive index of a material composite to close to the parameters of free space.

The phased array antenna work was a product of collaboration with Manus Ross and Dr. Steven A. Cummer, formerly and currently of Duke University respectively, and Tai Lam of Boeing Research & Technology in Seattle, WA. The electromagnetic metamaterial radome work was the product of collaboration with Bryan Justice (formerly of Duke University) and Dr. Anthony F. Starr, both of SensorMetrix Inc. in San Diego, CA.

Some of the excerpts of this dissertation have either been published or are awaiting review for publication. These are:

Introduction of the concept of phased array impedance matching using anisotropic materials, implementable using metamaterials:
Sajuyigbe, S.; Cummer, S.A.; Smith, D.R.; , "Utilization of metamaterials for wide angle impedance matching (WAIM) in phased array antennas," *Antennas and Propagation Society International Symposium, 2009. APSURSI '09. IEEE* , vol., no., pp.1-4, 1-5 June 2009

Integration of anisotropic parameters into array performance characterization, op-

timization study on use of anisotropic materials to realize wide-angle impedance matching, and numerical study on use of homogeneous anisotropic model to represent planar metamaterial sheet:
Sajuyigbe, S.; Ross, M.; Geren, P.; Cummer, S.A.; Tanielian, M. H.;Smith, D.R., "Wide Angle Impedance Matching of Phased Array Antennas, using Metamaterials," Submitted to *IET Microwaves, Antennas and Propagation*, 2009

Experimental study investigating modeling of a metamaterial as an anisotropic impedance matching layer:
Sajuyigbe, S.; Lam, T. A.; Tanielian, M. H.; Smith, D.R.; "Experimental Characterization of Phased Array Antenna with a Metamaterial Matching Layer," Submitted to *Antennas and Wireless Propagation Letters, IEEE*, 2010

Numerical study on metamaterial composite for antenna enclosures:
Sajuyigbe, S.; Justice, B.J.; Starr, A.F.; Smith, D.R.; , "Design and Analysis of Three-Dimensionalized ELC Metamaterial Unit Cell," *Antennas and Wireless Propagation Letters, IEEE* , vol.8, no., pp.1268-1271, 2009

Experimental study on metamaterial composite for antenna enclosures:
Sajuyigbe, S.; Justice, B.J.; Starr, A.F.; Overfelt, P. L.; Smith, D.R.; , "Experimental Characterization of Metamaterial Composite with Embedded Three-Dimensionalized ELC Inclusions," Submitted to *Antennas and Wireless Propagation Letters, IEEE*, 2010

2

Phased Array Antenna Wide Angle Impedance Matching

The initial foray into phased array antenna research arose from the need for highly directional antennas with rapidly steerable beams. Before the advent of phased array antennas, mechanically rotated dish antennas were used to provide directional beams that were only as steerable as the speed of the antenna rotation. Phased arrays, however, provide agility, precision, speed, and automation to radar and communication systems. A phased array antenna consists of an array of identical antenna elements such as microstrip patches, dipoles, waveguide apertures, and so forth. The conception of the theory behind phased array antennas is fairly old, but its implementation only began in the late 1950s, primarily at MIT Lincoln Laboratory [42, 43], after the initial development of phase shifters and computers – one of the two technologies on which the performance of phased array antennas would hinge.

Input power may be coupled into a phased array in a number of ways: all the elements in the array can be fed by the same power feed, or altenatively, each element with a different power feed. When all fed with the same feed, the input power line

is connected to a power divider network that splits the power evenly among all the elements. Between each power split and its connecting antenna element is a phase shifter to impose a phasing on the element's signal. The phase gradient across the surface of an array determines the angle of steer. The relative phase difference provided by phase shifters correct the path difference caused by the inter-element spacing. This results in constructive interference at the intended scan angle but destructive interference at all other angles. Today, phase shifters are connected to computers, which rapidly determine and adjust the phase gradient across the array in order to precisely steer the radiating beam in the desired direction.

One of the metrics by which the performance of a phased array antenna is judged is the array's ability to radiate its input power to every possible scan angle. As discussed in the previous chapter, the fractional amount of power transmitted out of a phased array antenna varies with scan due to mutual coupling between the elements. For planar arrays (i.e. conformal to a flat planar surface), one remediation strategy is to place layers of dielectric materials on the surface of the antenna in order to optimize the transmitted power ratio at all angles of scan. These materials are termed wide-angle impedance matching layers (WAIMs).

Dielectric WAIMs have proved highly useful in addressing the impedance mismatch problems in phased array antennas but are limited in their use because only a limited set of dielectric materials are available in nature for this purpose. As a result it becomes difficult (or impossible) to completely match a phased array at all the desired scan angles if the necessary dielectric properties are not available.

For this dissertation work, the use of metamaterials to mitigate the impedance variation and mismatch problem in planar phased arrays was explored. The numerically analyzed array consists an arrangement of circular waveguides that open out of a conducting sheet, as shown in Figure 2.1. An experimental implementation of a similar phased array antenna with WAIMs layers is shown in Figure 2.2.

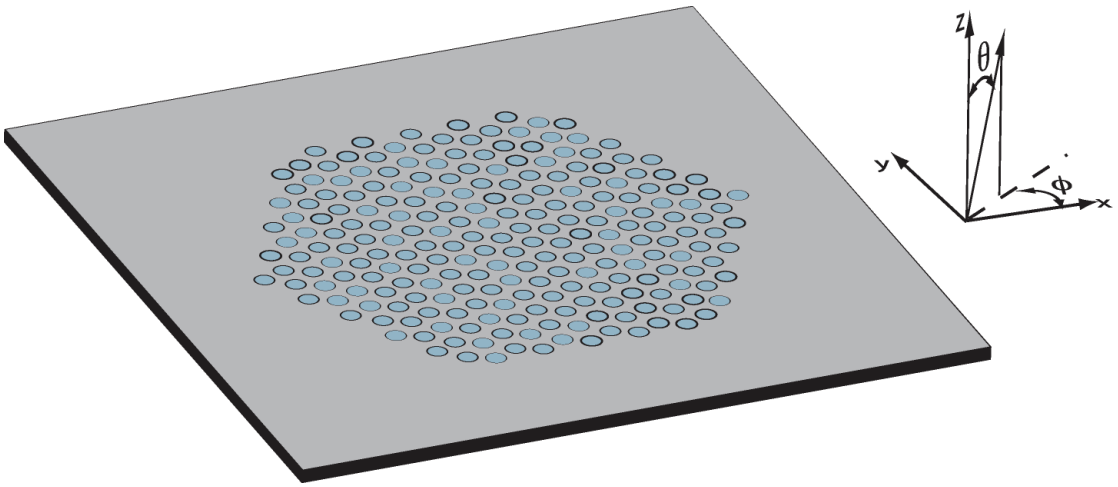

FIGURE 2.1: Sample rendering of a planar phased array of circular waveguide apertures opened out of a conducting sheet.

2.1 Phased Array Impedance Variation

The ability of a phased array to radiate its input power is quantified in its reflection coefficient, $\Gamma(\theta, \phi)$, which is dependent on the disparity between the mode impedance of the propagating waveguide mode and the radiation impedance at the outlet (aperture) of each waveguide element of the array. Signals that are not radiated to the desired scan angles (θ and ϕ) are typically reflected back into the waveguide elements and down into the feed system, or are transmitted out as surface waves that propagate along the surface of the array but not to the angle of interest [38]. The appearance of surface waves may result in a phenomenon known as scan blindness, an occurrence in which no power is radiated to the desired angle of scan. Although no power is actually reflected, because power is hoarded away from the direction of scan, the reflection coefficient at the intended scan angle appears to be large. For an array of infinite extent[1], all elements, which we can assume to radiate identically, radiate the input power into free space [42, 45] as

[1] An array with over one thousand elements can be estimated to behave as an infinite array [44]

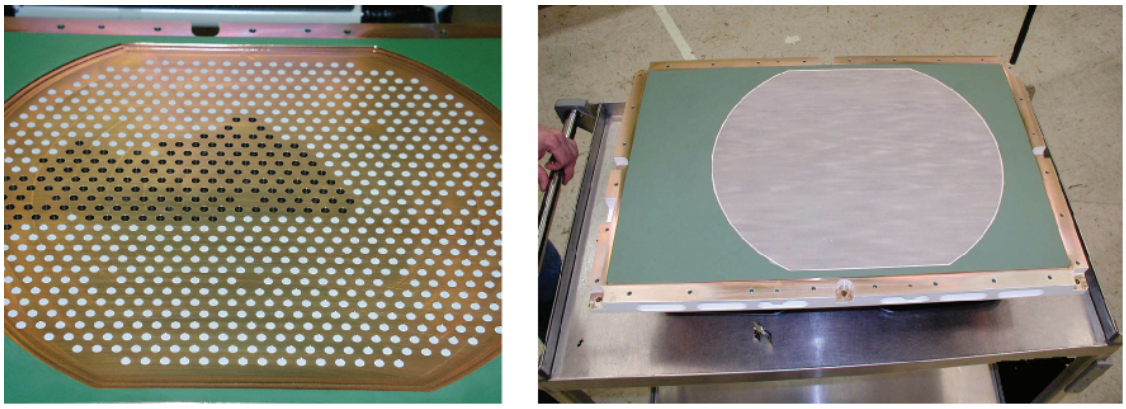

FIGURE 2.2: (a) Picture of phased array antenna composed of radiating circular waveguide elements, some of which are yet to be loaded with dielectric plugs. (b) Same antenna, with dielectric WAIM covering. [Pictures courtesy Boeing Research & Technology, Seattle, WA]

$$\frac{P_{\mathrm{r}}(\theta,\phi)}{P_{\mathrm{i}}} = (1 - |\Gamma(\theta,\phi)|^2) f(\theta) \tag{2.1}$$

where,

$$\Gamma(\theta,\phi) = \frac{Y_{\mathrm{feed}} - Y_{\mathrm{in}}(\theta,\phi)}{Y_{\mathrm{feed}} + Y_{\mathrm{in}}(\theta,\phi)} \tag{2.2}$$

$f(\theta)$ is a physical limitation that represents the reduction in effective aperture cross section as the beam is steered to angles away from the normal, which varies based on geometric considerations as $\cos\theta$, $(\cos\theta)^{\frac{3}{2}}$, or $(\cos\theta)^2$, depending on the azimuthal plane of scan and the mode distribution of the antenna element [46]. To

maximize the radiated power, we must minimize $\Gamma(\theta, \phi)$, preferably forcing it to zero at all scan angles θ and azimuthal planes ϕ. Aided by computational tools, phased array system engineers minimize or force $\Gamma(\theta, \phi)$ to zero at select scan angles by placing dielectric layers over the array surface [39]. Well-chosen dielectric layers modify $\mathrm{Y_{in}}(\theta, \phi)$, the radiation admittance[2] of the antenna system, to a value close to Y_{feed} in order to minimize the disparity between both admittances[3]. This is typically done by performing an optimization to vary the dielectric values and thicknesses of one or more dielectric layers until an acceptable $\mathrm{Y_{in}}$ is achieved[4] over all scan angles. In the next sections, we shall visit some of the analytical approaches for computing the active element admittance of phased arrays, so that we can perform impedance matching optimizations with anisotropic WAIMs and compare the performance achievable with conventional dielectric WAIMs. Metamaterials are used primarily to implement anisotropic materials.

2.2 Active Element Admittance

The active element admittance of an infinite array is defined as the admittance at the aperture-air interface of a single element at the center of the array when all of the elements in the array are radiating [42]. The active element admittance includes all of the interactions due to other elements in the array and is a function of inter-element spacing, aperture geometry, lattice topology, frequency of operation, and the scan angle. The disparity between the active element admittance and the waveguide propagating mode admittance indicates the level of impedance mismatch of the array, which varies as a function of scan angle.

[2] $\mathrm{Y_{in}}(\theta, \phi)$ is referred to as *active element admittance* in the literature.

[3] For an array of circular waveguide apertures, $\mathrm{Y_{feed}}$ is the admittance looking into the waveguide and feed system. Since the feed system is generally matched to the admittance of the dominant propagating mode, $\mathrm{Y_{feed}}$ is the mode admittance of the propagating $\mathrm{TE_{11}}$ mode.

[4] For the sake of notational brevity, I represent the active element admittance as $\mathrm{Y_{in}}$ instead of $\mathrm{Y_{in}}(\theta, \phi)$.

Various approaches for analytically computing the active element admittance of phased arrays have been explored in the literature [6,37,42,43,45,47–49]. Because it is considerably less difficult to find the active element admittance of an infinite array, most approaches make the infinite array assumption due to its simplicity in describing very large – but finite – arrays. In an infinite array, all elements possess identical radiation and active admittance characteristics because each element receives the same amount of mutual coupling as all other elements. The infinite array assumption is a valid for very large arrays since most elements would be at the central region of such an array. In the central region of a very large array, each element can be assumed to be in a nearly infinite array environment. Edge elements, however, possess different admittance and radiation characteristics than central elements because they are not completely surrounded by other elements hence have different mutual coupling. The active element admittance of one unit element of a phased array can thus be used to estimate the active element admittance of the whole array, provided the array is large enough. Figure 2.1 shows the typical geometry of an planar array of circular waveguides radiating out of a conducting sheet, and Figure 2.3 depicts the unit element lattice of our sample planar array.

The approaches used to calculate *active element admittance* can be grouped into two categories: the "one-mode model" approach [6, 43, 47], and the "multi-mode model" approach [37,42,49]. For a planar waveguide-aperture phased array, the one-mode model approach derives $\mathrm{Y_{in}}(\theta, \phi)$ based on the assumption that the transmitted power ratio depends solely on the dominant waveguide mode, while the multi-mode model solves the complete elemectromagnetic problem thereby determining that the transmitted power ratio is dependent on the dominant waveguide mode as well as the reactive contributions from non-propagating waveguide modes that are in the cutoff regime.

The multi-mode model is developed by enforcing the tangential boundary con-

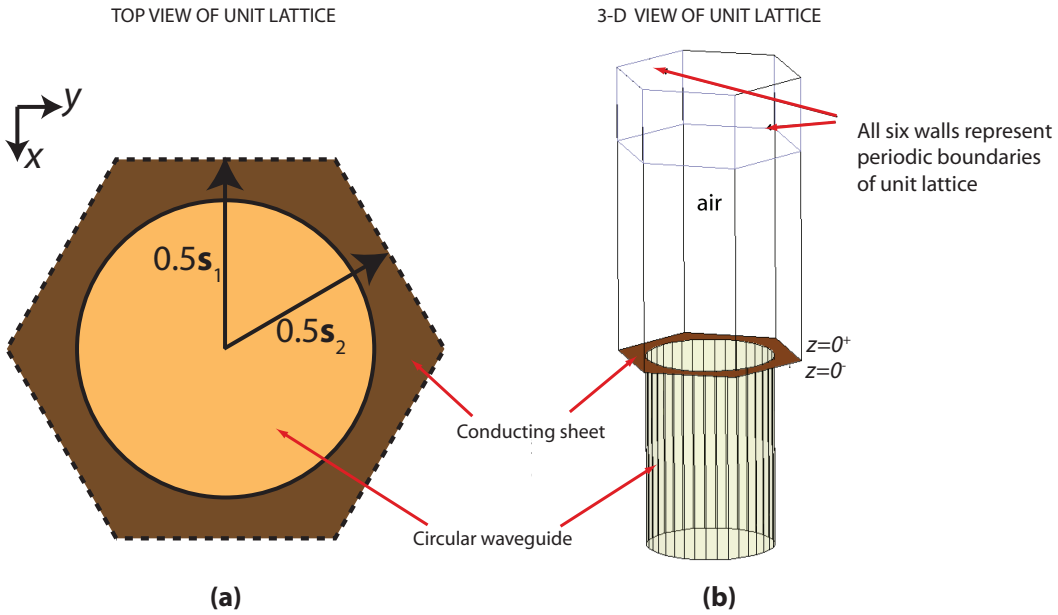

FIGURE 2.3: (a) Top view of phased array unit cell, with lattice position vectors $\mathbf{s}_1$ and $\mathbf{s}_2$ (b) 3D rendering of phased array unit cell showing feed waveguide

ditions on the array aperture junction (the array surface), thereby culminating in an expression for $\mathrm{Y}_{\mathrm{in}}(\theta, \phi)$ that captures all power transmission ratio curve features that the one-mode model could not predict. More rigorous and thorough, the multi-modal approach incorporates the influence of a cascade of waveguide modes (the propagating and an infinity of nonpropagating modes), each mode influencing the excited spatial harmonics (free-space modes) at the array surface. The one-mode model is considered to be a first-order approximation of the more rigorous multi-mode model and is referred to as the *grating lobe series*. Though it may be surprising that nonpropagating modes contribute to the active element admittance, each cut-off waveguide mode reactively cross-interacts with the propagating mode as well as with all other nonpropagating waveguide modes. The cross-interaction parameters encapsulate the relationship between waveguide modes in the waveguide side of the array surface, and the free space harmonics excited above the array surface. In other

words, this technique takes into account the influence of all waveguide modes on the excitation of spatial harmonics just beyond the aperture. Though different from the one-mode model, the multi-modal model takes the form of a combination of several grating lobe series.

In this work the multi-modal formulation derived by Borgiotti [49] is utilized to solve for the active element admittance of a planar phased array fed with circular waveguide elements. By enforcing the electric and magnetic boundary conditions at the $z = 0$ plane (see Figure 2.3), Borgiotti's approach clearly incorporates both the contribution of higher order waveguide modes in the waveguide and higher order evanescent free space modes just above the aperture discontinuity. The canonical form of the resulting expression for $\mathrm{Y_{in}}(\theta, \phi)$ is straightforwardly implementable for planar arrays regardless of waveguide antenna element design.

2.2.1 Grating Lobe Series

Before adapting the multi-modal model to the calculation of $\mathrm{Y_{in}}(\theta, \phi)$ for anisotropic WAIMs, we shall first use the one-mode model to derive $\mathrm{Y_{in}}(\theta, \phi)$ because, this approach, though incomplete, provides fundamental physical insight into the interactions and spatial harmonic excitations at the array surface. For the sake of illustration and simplicity, we derive $\mathrm{Y_{in}}(\theta, \phi)$ for a planar one-dimensional array of radiating parallel plate waveguide apertures, as performed by Parad [6]. Figure 2.4 depicts a $(2|p|_{\max} + 1)$-element array of parallel-plate waveguides, each of which is infinitely long in the $\hat{y}$-direction.

Because a uniform TEM mode is the fundamental propagating mode in an infinitely long parallel-plate waveguide, the electric field distribution across each aperture is strictly x-polarized and uniform within each aperture. Across the planar phased array, a phase gradient, $e^{-jpk_x d}$, is imposed upon each aperture in order to ensure that the resulting plane wave in the far field propagates with transverse

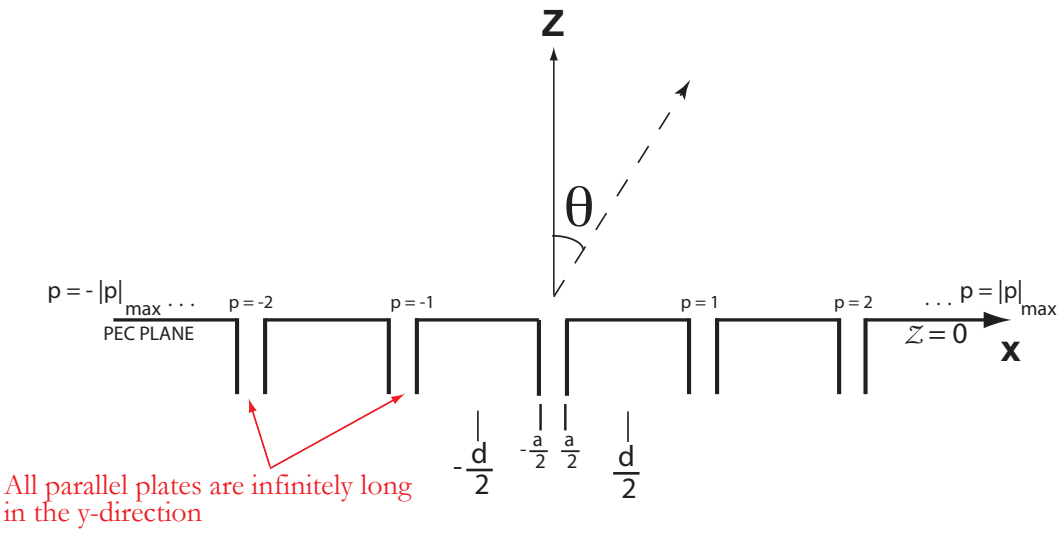

FIGURE 2.4: Cross-sectional profile of unidimensional $(2|p|_{\max}+1)$-element parallel-plate array with infinitely long apertures in the $\hat{y}$ direction, radiating into the two-dimensional $x-z$ plane. Adapted from [6]

wavenumber k_x. Note that $k_x = k_0 \sin\theta\cos\phi$, but since we are restricted to the $x-z$ plane on which $\phi = 0°$, then $k_x = k_0 \sin\theta$,

In this method, we approximate the fields on the surface of the array shown in Figure 2.4, which we shall henceforth refer to as the $z = 0$ plane, which can be expressed as

$$E_x(x,0) = \begin{cases} E_0 e^{-jpdk_x x} & \text{for } -\frac{a}{2} + pd < x < \frac{a}{2} + pd \\ 0 & \text{elsewhere} \end{cases}$$

$$E_z = 0 \tag{2.3}$$

As the field profile along the $z = 0$ plane is periodic, we can rewrite it in a form that resembles a complex Fourier series summation. The tangential electric field can be rewritten as

$$E_x(x,0) = \frac{aE_0}{d} \sum_{p=-\infty}^{+\infty} \frac{\sin\frac{a}{2}(k_x + p\frac{2\pi}{d})}{\frac{a}{2}(k_x + p\frac{2\pi}{d})} \cdot e^{-j(k_x + p\frac{2\pi}{d})x} \tag{2.4}$$

The equation in (2.4) expresses the fields across the $z = 0$ plane as the summation of a spatial harmonics expansion ($e^{-j(k_x+p\frac{2\pi}{d})x}$), each term weighted by the Fourier transform of the uniform field distribution over the parallel plate waveguide aperture. The array is assumed to be infinitely long, with $|p|_{\max} = \infty$. Spatial harmonics are modes that exist in free space, some of these propagate (homogeneous plane waves), and some do not (inhomogenous or evanescent plane wave modes). The first spatial harmonic, i.e. p=0, is a propagating plane wave while the other terms in (2.4) are nonpropagating. The term *grating lobe* refers to the evanescent plane wave modes that occur at the surface of a planar phased array antenna. In other words, according to the grating lobe series we can consider (2.4) to be a profile of the grating lobes excitable by an array of apertures with uniform field distribution and phasing $e^{-j(k_x+p\frac{2\pi}{d})x}$.

To obtain a grating lobe series derivation of the active element admittance from (2.4), the contribution of all the grating lobes to $\mathrm{Y_{in}}$ must be quantified. The input admittance of a TM-polarized plane wave mode of index p can be easily derived from Maxwell's equations, and we shall present it in canonical form as

$$Y_p = \frac{1}{\eta\cos\theta} = \left[\eta\sqrt{1 - (\frac{k_x + p\frac{2\pi}{d}}{k_0})^2}\right]^{-1} \tag{2.5}$$

We shall also express the power within each waveguide below the aperture in terms of the active element admittance as,

$$P_{\text{waveguide}} = \frac{1}{2}(E_0 a)(E_0 a)^* Y_{\text{in}}^* \tag{2.6}$$

and the power radiated out of the aperture (from the lattice region of length d in the x-direction and arbitrary length l in the y-direction) as

$$P_{\text{cell}} = \frac{1}{2}\int_0^l \int_{-d/2}^{d/2} E_x H_y^* dxdy = \frac{1}{2}\int_0^l \int_{-d/2}^{d/2} E_x (E_x Y_p)^* dxdy \tag{2.7}$$

Equating (2.6) with the result of (2.7) and rearranging for $\mathrm{Y_{in}}$, yields

$$Y_{\text{in}} = \frac{2P^* l}{a^2|E_0|^2} = \frac{l}{d}\sum_{n=-\infty}^{+\infty} Y_p \cdot \left[\frac{\sin\frac{a}{2}\left(k_x + p\frac{2\pi}{d}\right)}{\frac{a}{2}\left(k_x + p\frac{2\pi}{d}\right)}\right]^2 \tag{2.8}$$

The expression in (2.8) is known as the *grating lobe series* or *one-mode* model because it utilizes a weighted summation of the admittance contribution of the excited spectrum of free space modes, weighted by the Fourier transform of the aperture field distribution of a waveguide aperture at the array surface. As an aside, there should only be one visible free space mode – the propagating plane wave – in a phased array. The visibility or non-visibility of a free space mode in the setup of Figure 2.4 is dependent upon the spacing, d, and the spatial harmonic index, p. In (2.9), when $d < \frac{\lambda}{2}$, there is a visible lobe at $p = 0$, but other values of n will cause a value of $k_x + p\frac{2\pi}{d}$ larger than $\frac{\omega}{c}$ at some angles, thereby creating an imaginary k_z (i.e. a grating lobe or evanescent plane wave mode).

$$k_z = \sqrt{\frac{\omega^2}{c^2} - \left[k_x + p\frac{2\pi}{d}\right]^2} \tag{2.9}$$

We have now calculated $\mathrm{Y_{in}}$ using the incomplete but physically insightful approach known as the grating lobe series. This one-mode model is not an accurate approximation. In the next section, we present the multi-modal approach, which we will ultimately use to calculate $\mathrm{Y_{in}}$ for a 2D array of circular waveguide apertures with anisotropic WAIM-layer coverings.

2.2.2 Multi-Modal Model

Now that we have derived the active element admittance using the one-mode model, we shall take a look at the multi-modal model for a practical bidimensional planar phased array radiating into three-dimensional space. A detailed derivation of Y_{in} for the multi-modal model is done in Appendix A.

Analytical Meaning of Multi-Modal Model

An important component of the multi-modal model, known as the self- or cross-grating lobe series, is presented in (2.16), but first, the following terms are defined: $\mathbf{u}_\circ$ is the scan vector representing the direction of steer:

$$\mathbf{u}_\circ = \hat{x}\frac{2\pi}{\lambda_0}\sin\theta\cos\phi + \hat{y}\frac{2\pi}{\lambda_0}\sin\theta\sin\phi \tag{2.10}$$

$\mathbf{u}_{\circ pq}$ is the scan vector plus the collection of grating lobes, and is represented as:

$$\mathbf{u}_{\circ pq} = \mathbf{u}_{\circ pq} = \mathbf{u}_\circ + p\mathbf{t}_1 + q\mathbf{t}_2 \tag{2.11}$$

where $\mathbf{t}_1$ and $\mathbf{t}_2$ are reciprocal lattice vectors and are directly related to the array unit cell lattice vectors by:

$$\mathbf{t}_1 = 2\pi\frac{\mathbf{s}_2 \times \mathbf{s}_3}{\mathbf{s}_1 \cdot \mathbf{s}_2 \times \mathbf{s}_3} \qquad \mathbf{t}_2 = 2\pi\frac{\mathbf{s}_3 \times \mathbf{s}_1}{\mathbf{s}_1 \cdot \mathbf{s}_2 \times \mathbf{s}_3} \tag{2.12}$$

$$\tag{2.13}$$

ξ_i is the Fourier transform of the antenna element mode(s) across the surface area, A, of the antenna element, and is related to the mode field distribution as:

$$\xi_i(\mathbf{u}) = \frac{1}{2\pi}\iint_A \mathbf{e}_i(\mathbf{x})e^{\mathbf{u}\cdot\mathbf{x}}d\mathbf{x} \tag{2.14}$$

where $\mathbf{e}_i$ represents the field distribution of the i^{th} mode of the antenna element. (For instance, i=0 mode for an array of circular antenna elements is the TE_{11} mode,

and the i=1 mode is the next higher order mode, etc.). Since the mode field distribution is a two-dimensional vector along the x-y surface of the antenna element aperture, $\mathbf{e}_i$ can either be expressed as a sum of the $\hat{x}$ and $\hat{y}$ field components or $\hat{\rho}$ and $\hat{\psi}$ field components, the former representing rectangular coordinates and the latter representing cylindrical coordinates. It turns out that, using cylindrical coordinates, it is mathematically convenient to relate the Fourier transform of the antenna element mode(s) to the admittance of the spatial harmonics. The mode Fourier transform term ξ_i can therefore be expressed as:

$$\xi_i(\mathbf{u}) = \frac{1}{2\pi} \iint_A \mathbf{e}_i(\mathbf{x}) e^{\mathbf{u}\cdot\mathbf{x}} = \hat{\rho}\xi_{i\rho} + \hat{\psi}\xi_{i\psi} \tag{2.15}$$

$\mathrm{Y_{TE}}$ and $\mathrm{Y_{TM}}$ relate the transverse admittance of the spatial harmonics excited at $z = 0^+$ to the electric field from the antenna elements.

See Appendix A, and in Appendix B for more detail on the above expressions.

$$Y_{ki}(\mathbf{u}_\circ) = \frac{4\pi^2}{C} \sum_{\mathbf{u}_{\circ pq}} [\xi_{i\rho}(\mathbf{u}_{\circ pq}) \xi^*_{k\rho}(\mathbf{u}_{\circ pq}) Y_{\mathrm{TM}}(|\mathbf{u}_{\circ pq}|) + \xi_{i\psi}(\mathbf{u}_{\circ pq}) \xi^*_{k\psi}(\mathbf{u}_{\circ pq}) Y_{\mathrm{TE}}(|\mathbf{u}_{\circ pq}|)] \tag{2.16}$$

When $i = k = 0$, (2.16) is exactly equivalent to the grating lobe series discussed in Section 2.2.1. For other $i = k$ values, the equation represents the self-grating lobe series due to that i^{th} mode. For $i \neq k$, (2.16) is the cross grating lobe series.

Y_{ki} is the mutual admittance between mode k and mode i. For instance, $\mathrm{Y_{05}}$ is the mutual admittance between the fundamental progapating antenna element mode and the fifth excited higher order mode. This term quantifies the reactive (or real) exchange of power between modes excited at the aperture. (Real power is typically not exchanged between the excited modes if the antenna element is designed to

support only one propagating mode.) Though real power may not be exchanged, the reactive relationship between modes affects the input impedance seen by the power-carrying fundamental propagating mode. In essence, each mode can be thought of as a port. The scalar input admittance $\mathrm{Y_{in}}$ is the equivalent admittance seen by the input port (the fundamental mode) when looking out into the interactive relationship between all of the other ports (an infinity of higher order modes).

The multi-modal model utilizes Y_{ki} for several values of i and k (i and k are waveguide mode indices, for instance, $i = 0$ refers to the fundamental mode, while $i = 1$ refers to the first cutoff mode and so forth) to calculate the overall active element admittance of an array. The various values of Y_{ki} can be related to $\mathrm{Y_{in}}$ as presented in (A.29). The interrelationship is illustrated in the set of equations below:

$$\begin{aligned} Y_{\mathrm{in}} V_0 - \sum_{i=0}^{N-1} V_i Y_{0i}(\mathbf{u}_\circ) &= 0 \\ Y_k V_k + \sum_{i=0}^{N-1} V_i Y_{ki}(\mathbf{u}_\circ) &= 0 \end{aligned} \tag{2.17}$$

Note that V_i is a weighting term that represents the voltage across a mode $\mathbf{e}_i$. It does not directly come into play in the calculation of the active element admittance.

In order to accurately calculate $\mathrm{Y_{in}}$, it is imperative to take into account as many as possible waveguide modes (from $i = 0$ to $i = N - 1$) and free space harmonics modes (from $p = q = -|p|_{\max}$ to $p = q = |p|_{\max}$). If we for instance, only want to take into account the fundamental propagating waveguide mode, then we set $N = 1$, which means that our set of simultaneous equations in (2.17) would reduce to (2.18), which is simply the grating lobe series.

$$N = 1 \quad \text{results in} \quad Y_{\mathrm{in}} = Y_{00} \tag{2.18}$$

When more waveguide modes are taken into account, say the fundamental and two higher order modes, we set $N = 3$, and 2.17 becomes:

$$\begin{aligned} N = 3 \quad \text{results in} \quad & Y_{\text{in}}V_0 - Y_{00}V_0 - Y_{01}V_1 - Y_{02}V_2 = 0 \\ & Y_1V_1 + Y_{10}V_0 + Y_{11}V_1 + Y_{12}V_2 = 0 \\ & Y_2V_2 + Y_{20}V_0 + Y_{21}V_1 + Y_{22}V_2 = 0 \end{aligned} \tag{2.19}$$

which can be rewritten as:

$$\begin{aligned} (Y_{\text{in}} - Y_{00})V_0 - Y_{01}V_1 - Y_{02}V_2 = 0 \\ Y_{10}V_0 + (Y_{11} + Y_1)V_1 + Y_{12}V_2 = 0 \\ Y_{20}V_0 + Y_{21}V_1 + (Y_{22} + Y_2)V_2 = 0 \end{aligned} \tag{2.20}$$

We know from linear algebra that the determinant of the preceding equation must equal zero. A manipulation of the determinant results in the expression for Y_{in} in (2.22).

$$\begin{vmatrix} Y_{\text{in}} - Y_{00} & -Y_{01} & -Y_{02} \\ Y_{10} & Y_{11} + Y_1 & Y_{12} \\ Y_{20} & Y_{21} & Y_{22} + Y_2 \end{vmatrix} = 0 \tag{2.21}$$

Rearranging 2.21,

$$Y_{\text{in}} = \frac{\begin{vmatrix} -Y_{00} & -Y_{01} & -Y_{02} \\ Y_{10} & Y_{11} + Y_1 & Y_{12} \\ Y_{20} & Y_{21} & Y_{22} + Y_2 \end{vmatrix}}{\begin{vmatrix} Y_{11} + Y_1 & Y_{12} \\ Y_{21} & Y_{22} + Y_2 \end{vmatrix}} \tag{2.22}$$

Equation (2.22) expresses that the active element admittance derives from the grating lobe series Y_{00}, the cross grating lobe series (Y_{01}, Y_{11}, Y_{20}, Y_{21}, Y_{21}), and the

mode admittance Y_1 for the first higher-order mode and Y_2 for the second higher-order mode. Once these higher-order modes have been identified, the mode admittances are straightfoward to find. For a circular waveguide, the mode admittance of each mode is a well known quantity.

Multi-Modal Model using Multi-Port Analogy

In this subsection, we shall attempt to provide a circuit model analogy for the multi-modal model represented in (2.17). Because an infinity of higher-order waveguide modes are excited at the aperture-discontinuity of each phased array antenna element, we shall assign an electrical port to account for each of these modes.

An arbitrary electrical network of admittance matrix Y', currents I' and voltages V' may be represented by the multi-port Y-matrix:

$$[I'] = [Y'][V'] \tag{2.23}$$

which can be fully written as:

$$\begin{bmatrix} I'_1 \\ I'_2 \\ . \\ . \\ . \\ I'_{N-1} \\ I'_N \end{bmatrix} = \begin{bmatrix} Y'_{11} & Y'_{12} & . & . & . & Y'_{1,N-1} & Y'_{1,N} \\ Y'_{21} & . & . & . & . & . & . \\ . & . & . & . & . & . & . \\ . & . & . & . & . & . & . \\ . & . & . & . & . & . & . \\ Y'_{N-1,1} & . & . & . & . & . & Y'_{N-1,N} \\ Y'_{N,1} & . & . & . & . & . & Y'_{N,N} \end{bmatrix} \begin{bmatrix} V'_1 \\ V'_2 \\ . \\ . \\ . \\ V'_{N-1} \\ V'_N \end{bmatrix} \tag{2.24}$$

The graphical network of excited higher-order waveguide modes – according to (2.17) – in a phased array waveguide element can be represented with a Y-matrix of the form shown in (2.25).

$$\begin{bmatrix} 0 \\ 0 \\ . \\ . \\ . \\ 0 \\ 0 \end{bmatrix} = \begin{bmatrix} Y_{\text{in}} - Y_{00} & -Y_{01} & . & . & . & -Y_{0,N-2} & -Y_{0,N-1} \\ Y_{10} & Y_{11} + Y_1 & Y_{12} & . & . & Y_{1,N-2} & Y_{1,N-1} \\ Y_{20} & Y_{21} & Y_{22} + Y_2 & Y_{23} & . & Y_{2,N-2} & Y_{2,N-1} \\ . & . & . & . & . & . & . \\ . & . & . & . & . & . & . \\ . & . & . & . & . & . & . \\ Y_{N-1,0} & Y_{N-1,1} & . & . & . & . & Y_{N-1,N-1} + Y_{N-1} \end{bmatrix} \begin{bmatrix} V_0 \\ V_1 \\ . \\ . \\ . \\ V_{N-2} \\ V_{N-1} \end{bmatrix} \tag{2.25}$$

2.3 Step-by-Step Methodology for calculating $\mathrm{Y_{in}}$ using Multi-Modal Model

A brief summary of the steps to find $\mathrm{Y_{in}}$ for a central element in a very large array is delineated below.

Step 1. Define the lattice vectors $\mathbf{s}_1$ and $\mathbf{s}_2$.

Step 2. Find the reciprocal lattice vectors $\mathbf{t}_1$ and $\mathbf{t}_2$ from $\mathbf{s}_1$ and $\mathbf{s}_2$.

Step 3. Utilize $\mathbf{t}_1$ and $\mathbf{t}_2$ to construct a general expression for $\mathbf{u}_{\circ pq}$.

Step 4. Determine the number of waveguide modes, N, and spatial harmonics modes ($|p|_{\max}$=$|q|_{\max}$) that will be included in the computation (the higher the better).

Step 5. Obtain/derive general expressions for the transverse admittance of TE and TM spatial harmonics modes.

Step 6. Obtain expressions for the Fourier transform of all the waveguide modes taken into consideration, including the fundamental, and incorporate $\mathbf{u}_{\circ pq}$ expression. See Section A.4 of Apendix A

Step 7. Calculate the matrix of self and cross-grating lobe series terms Y_{ki} for all the waveguide modes considered, and calculate the mode admittance Y_k for all the cutoff modes considered.

Step 8. Determine system of equations using (2.17), inserting the results of Step 7

as the coefficients of the voltage terms.

Step 9. Solve for Y_{in} by setting the determinant of the system of equations to zero.

2.4 Calculation of Y_{in} for Two-dimensional Planar Phased Array of Circular Waveguides

Let us use the previous derivations of *active element admittance* to compute Y_{in} for the typical but arbitrary planar phased array configuration represented by the unit element lattice depicted in Figure 2.5. We utilize the grating lobe series, multi-model approach and the numerical solver HFSS to calculate the active element admittance as a function of scan. (The reader may ask: Why go through the hassle of an analytical derivation when numerical solvers like *Ansoft* HFSS or CST Microwave Studio can be used? Well, it is true that these numerical software are precise and can handle arbitrary geometry, however, full-wave simulations are time-consuming and are not appropriate for the kind of rapid optimization that we will later use to prescribe optimized anisotropic WAIM layers for a planar phased array antenna system.)

The lattice vectors of the planar array whose unit lattice is shown in Figure 2.5 can be written in terms of lattice parameter $d = 2 \times 0.21" = 0.42" = 1.0668 \times 10^{-2}$ m to be:

$$\mathbf{s}_1 = d\hat{x}$$

$$\mathbf{s}_2 = d(\hat{x}\sin 30^\circ + \hat{y}\cos 30^\circ) = d\left(\frac{1}{2}\hat{x} + \frac{\sqrt{3}}{2}\hat{y}\right) \tag{2.26}$$

We then obtain $\mathbf{t}_1$ and $\mathbf{t}_2$ (from (A.4) of Appendix A), yielding:

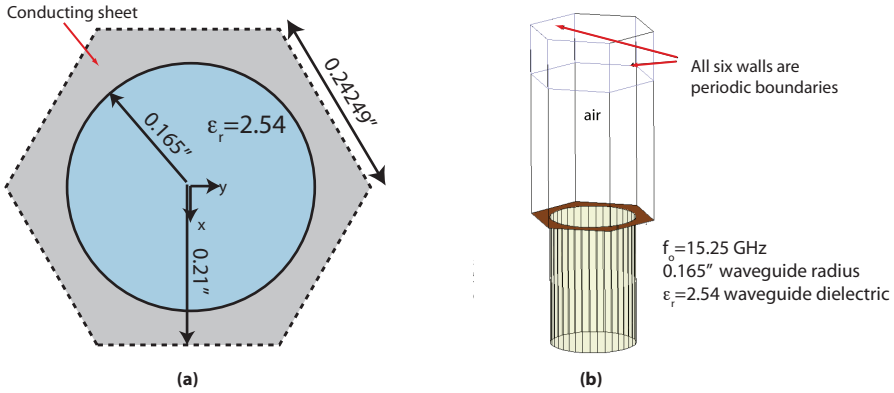

FIGURE 2.5: Unit element lattice and dimensions of waveguide-aperture planar phased array of interest. (a) Top view (b) 3D View. (The circular waveguide elements of the planar phased array are assumed fed with a $\hat{y}$-polarized feed which excites a propagating TE_{11} mode that is primarily polarized along the $\hat{y}$-direction.)

$$\mathbf{t}_1 = \frac{2\pi}{d}\left(\hat{x} - \frac{1}{\sqrt{3}}\hat{y}\right)$$
$$\mathbf{t}_2 = \frac{2\pi}{d}\left(\frac{2}{\sqrt{3}}\hat{y}\right) \tag{2.27}$$

(2.27) leads to

$$\mathbf{u}_{\circ pq} = \mathbf{k}_t = \hat{x}\left(\frac{2\pi}{\lambda}\sin\theta\cos\phi + p\frac{2\pi}{d}\right) + \hat{y}\left(\frac{2\pi}{\lambda}\sin\theta\sin\phi + \frac{2\pi}{d}\left[q\frac{2}{\sqrt{3}} - p\frac{1}{\sqrt{3}}\right]\right) \tag{2.28}$$

$\mathbf{u}_{\circ pq}$ is the effective transverse wavenumber of the planar phased array system and we may thus also refer to it as[5]. We introduce the representation $\mathbf{k}_t$ because it notationally signifies the effective transverse wavevector of the lattice of grating

[5] Later in this document, I interchangeably refer to the lattice of grating lobes as $\mathbf{u}_{\circ pq}$ or $\mathbf{k}_t$ $\mathbf{k}_t$depending on if my aim is to emphasize that the parameter represents the lattice of grating lobes or the effective transverse wavenumber of the array antenna

lobes. The expression for $\mathbf{u}_{\circ pq}$ implies that the spatial harmonics modes that exist across the two-dimensional $z = 0^+$ array surface take the form:

$$e^{-j\mathbf{u}_{\circ pq}\cdot\mathbf{x}} = e^{-j\left[(k_0 \sin\theta\cos\phi + p\frac{2\pi}{d})x + (k_0 \sin\theta \sin\phi + \frac{2\pi}{d}\left[q\frac{2}{\sqrt{3}} - p\frac{1}{\sqrt{3}}\right])y\right]} \tag{2.29}$$

$\mathbf{u}_{\circ pq}$ can also be rewritten as:

$$\mathbf{u}_{\circ pq} = \mathbf{k}_t = \hat{x}u + \hat{y}v \tag{2.30}$$

Where,

$$\begin{aligned} |\mathbf{k}_t| &= \sqrt{u^2 + v^2} \\ u &= k_x + p\frac{2\pi}{d} \\ v = k_y + \frac{2\pi}{d}\left[q\frac{2}{\sqrt{3}} - p\frac{1}{\sqrt{3}}\right] \\ k_x &= k_0 \sin\theta\cos\phi \\ k_y &= k_0 \sin\theta\sin\phi \end{aligned} \tag{2.31}$$

2.4.1 Calculation of Y_{in} without Dielectric Sheet, using the Grating Lobe Series

We shall first use the grating lobe series to calculate $\mathrm{Y_{in}}$ by only taking the fundamental propagating waveguide mode into account, i.e. $N = 1$. To implement the grating lobe series, we follow the steps outlined in Section 2.3

In order to converge at a grating lobe series sum that takes most of the contributive spatial harmonics modes into account, we found that taking forty-nine modes into account enables a convergence of thte $\sum\sum_{\mathbf{u}_{\circ pq}}$ sum, i.e. $p = -3, -2, -1, 0, 1, 2, 3$ and $q = -3, -2, -1, 0, 1, 2, 3$.

Next, we utilize the admittance of free space modes as derived in Appendix B. For TM and TE polarized free space modes, respectively, the generalized transverse

admittance for free space plane waves with transverse wavenumber k_x expressed as:

$$Y_{\mathrm{TE}}(k_x) = \sqrt{\frac{\epsilon_0\epsilon_r}{\mu_0\mu_r} - \frac{k_x^2}{\omega^2\epsilon_0^2\epsilon_r^2}} \tag{2.32}$$

$$Y_{\mathrm{TM}}(k_x) = \left[\sqrt{\frac{\mu_0\mu_r}{\epsilon_0\epsilon_r} - \frac{k_x^2}{\omega^2\epsilon_0^2\epsilon_r^2}}\right]^{-1} \tag{2.33}$$

given that $\epsilon_r = 1$, $\mu_r = 1$, $\omega = 2\pi f = 2\pi(15.25 \times 10^9)$ *radians/s*.

Since the admittances will be acting on the lattice of grating lobes, $\mathbf{k}_t$, we shall rewrite them in the form:

$$Y_{\mathrm{TE}}(|\mathbf{k}_t|) = \sqrt{\frac{\epsilon_0\epsilon_r}{\mu_0\mu_r} - \frac{|\mathbf{k}_t|^2}{\omega^2\epsilon_0^2\epsilon_r^2}} \tag{2.34}$$

$$Y_{\mathrm{TM}}(|\mathbf{k}_t|) = \left[\sqrt{\frac{\mu_0\mu_r}{\epsilon_0\epsilon_r} - \frac{|\mathbf{k}_t|^2}{\omega^2\epsilon_0^2\epsilon_r^2}}\right]^{-1} \tag{2.35}$$

We then utilize the generalized form of the Fourier transforms of the radial and circumferential components of the circular waveguide antenna element modes as developed by Borgiotti [49], and presented in Section A.4 of Appendix A, for the circular waveguide modes in consideration. If we consider a to be the waveguide radius, for TE_{mn} waveguide modes the Fourier transforms are:

$$\xi_\rho(\mathbf{k}_t) = mj^{(m-1)}\frac{\sqrt{2/\pi}}{\sqrt{(x'_{mn})^2 - m^2}} \cdot \frac{\sin m\gamma}{|\mathbf{k}_t|} J_m(r|\mathbf{k}_t|) \tag{2.36}$$

$$\xi_\psi(\mathbf{k}_t) = j^{(m-1)}\frac{\sqrt{2/\pi}}{\sqrt{(x'_{mn})^2 - m^2}} \cdot \frac{a\cos m\gamma}{1 - (\frac{a|\mathbf{k}_t|}{x_{mn}})^2} \cdot J'_m(a|\mathbf{k}_t|) \tag{2.37}$$

and for TM_{np}, the Fourier transforms are:

$$\xi_\rho(\mathbf{k}_t) = -j^{(m-1)} \sin m\gamma \frac{|\mathbf{k}_t|\sqrt{2/\pi}}{(\frac{x_{mn}}{a})^2 - |\mathbf{k}_t|^2} J_m(r|\mathbf{k}_t|) \tag{2.38}$$

$$\xi_\psi(\mathbf{k}_t) = 0 \tag{2.39}$$

Where,

$$\cos m\gamma = \mathrm{Re}\left[\left(\frac{\hat{x}\cdot\mathbf{k}_t + \hat{y}\cdot j\mathbf{k}_t}{|\mathbf{k}_t|}\right)^m\right] \tag{2.40}$$

$$\sin m\gamma = \mathrm{Im}\left[\left(\frac{\hat{x}\cdot\mathbf{k}_t + \hat{y}\cdot j\mathbf{k}_t}{|\mathbf{k}_t|}\right)^m\right] \tag{2.41}$$

$\xi_{i\psi}$ in (2.16) represents the Fourier transform of the TE polarized component (with respect to the z-direction) of the i^{th} TE_{mn} or TM_{mn} mode away from the fundamental propagating circular waveguide mode, while $\xi_{i\rho}$ is the same for the TM polarized component of the same mode. Accordingly, $\xi_{0\psi}$ or $\xi_{0\rho}$ would each represent the TE and TM polarized components of the fundamental TE_{11} mode. Note that the expression for ξ_ψ in (A.30) is printed incorrectly in [49] but is displayed here in its corrected form. x_{mn} and x'_{mn} represent the $\mathrm{n}^t h$ root of J_m and J'_m Bessel functions.

To find $\mathrm{Y_{in}}$ using the one-mode model (i.e. N = 1), the system of equations in (2.17) reduce to (2.18). Given that the $i = 0$ mode is the TE_{11} mode, therefore $m = 1$ and $n = 1$, and we are able to obtain $\xi_{0\rho}$ and $\xi_{0\psi}$ from (2.36) and (**??**), by setting $m = 1$ and $n = 1$ in both equations.

The active element admittance derived from a grating lobe series analysis – truncating the sum at forty-nine spatial harmonics terms – yields:

$$Y_{\mathrm{in}} = Y_{00} = \frac{4\pi^2}{C}\sum_{p=-3}^{+3}\sum_{q=-3}^{+3}[\xi_{0\rho}(\mathbf{k}_t)\xi^*_{0\rho}(\mathbf{k}_t)Y_{\mathrm{TM}}(\mathbf{k}_t) + \xi_{0\psi}(\mathbf{k}_t)\xi^*_{0\psi}(\mathbf{k}_t)Y_{\mathrm{TE}}(\mathbf{k}_t)] \tag{2.42}$$

2.4.2 Calculation of Y_{in} without Dielectric Sheet, using Multimodal model

The number of waveguide modes taken into account in the calculation of $\mathrm{Y_{in}}$ determines the number of equations (see (2.17)) needed to be solved. In addition, the incorporation of, say, N waveguide modes will require the computation of N^2 self- and cross-grating lobe series terms (in addition to $\mathrm{N}-1$ higher order waveguide mode admittances) in order to adequately formulate the necessary set of equations. For instance, the incorporation of three waveguide modes would require the computation of $\mathrm{Y_{00}}$, $\mathrm{Y_{01}}$, $\mathrm{Y_{02}}$, $\mathrm{Y_{10}}$, $\mathrm{Y_{11}}$, $\mathrm{Y_{12}}$,$\mathrm{Y_{20}}$, $\mathrm{Y_{21}}$, $\mathrm{Y_{22}}$ – nine in total– and the calculation of higher order mode admittances $\mathrm{Y_1}$ and $\mathrm{Y_2}$.

The first three unique waveguide modes – in order of increasing cutoff frequency – of the array waveguide element (depicted in Figure 2.5) are the $\mathrm{TE_{11}}$, $\mathrm{TM_{01}}$, and $\mathrm{TE_{21}}$ modes, but, due to the symmetry of circular waveguide modes, the cross-polarized replicas of certain modes are excited as higher order modes at the array surface. For instance, a 90° orthogonal counterpart of the $\mathrm{TE_{11}}$ mode is excited at the array surface if the array is not cross-fed (even if cross-fed, this implies that there will be cross-interaction between both modes at the array surface). As a result, cross-polarized modes are higher order modes that should be taken into account when a multimodal model is used. For the circular waveguide in consideration, the first ten modes in order of excitation are: $\mathrm{TE_{11}}$, $\mathrm{TE_{11}}$ (90° cross-polarized), $\mathrm{TM_{01}}$, $\mathrm{TE_{21}}$, $\mathrm{TE_{21}}$ (45° cross-polarized), $\mathrm{TM_{11}}$, $\mathrm{TM_{11}}$ (90° cross-polarized), $\mathrm{TE_{01}}$, $\mathrm{TE_{31}}$, $\mathrm{TE_{31}}$ (30° cross-polarized). In general, TE_{mn} or TM_{mn} modes are cross-polarizable (when $m \neq 0$) by $\frac{180^\circ}{2m}$. An inspection of the several waveguide mode field configuration patterns shown in page 480 of Balanis [12] may help to shed light on mode symmetry and cross-polarized modes. For instance, the cross-polarized counterpart of an $\hat{x}$ polarized $\mathrm{TE_{11}}$ mode is a $\hat{y}$-polarized $\mathrm{TE_{11}}$ mode. The cross-polarized counterpart of the $\mathrm{TE_{21}}$ mode is rotated by 45°.

The mode admittance of a given mode and its cross-polarized counterpart are the same, however, the modifications in (2.44) should be made to the field distribution Fourier transform.

$$\text{Cross-polarized modes:} \quad \cos m\gamma = \text{Re}\left[\left(\frac{\hat{x}\cdot\mathbf{k}_t + \hat{y}\cdot j\mathbf{k}_t}{|\mathbf{k}_t|}\right)^m e^{j\frac{180^\circ}{2m}}\right] \tag{2.43}$$

$$\sin m\gamma = \text{Im}\left[\left(\frac{\hat{x}\cdot\mathbf{k}_t + \hat{y}\cdot j\mathbf{k}_t}{|\mathbf{k}_t|}\right)^m e^{j\frac{180^\circ}{2m}}\right] \tag{2.44}$$

A MATLAB script was written compute the active element admittance based on the formulation of (2.17). Figure 2.6 depicts results obtained when the one-mode and multi-mode approximations are used; these results are also compared to results obtained using the the full-wave solver HFSS. We presume the HFSS results to be the exact solution. Note that the HFSS solution was done by performing a 3D simulation of a single element lattice of the planar array, and then setting master-slave periodic boundary conditions on all the walls of the region above the aperture plane (as depicted in Figure 2.5).

An inspection of the viewgraphs in Figure 2.6 would seem to suggest that the one-mode model is acceptably accurate for modeling Y_{in}. In particular, the results of the one-model and the exact simulated solution seem to agree very closely particularly at the $\phi = 0^\circ$ and $\phi = 90^\circ$ planes; a qualitative disagreement only occurs at the $\phi = 45^\circ$ plane, when the scan angle θ exceeds 60°. The general agreement between the one-mode model and the exact solution, however, typically disappears when a dielectric layer is placed directly on the array surface. This is because the grating lobe admittances (Y_{TE} or Y_{TM}) change in the presence of one or more dielectric layers, thereby causing higher order waveguide modes to play a stronger role in the interaction that occurs on the array surface. In the next section, we discuss the incorporation of dielectric layers into Y_{TE} and Y_{TM}.

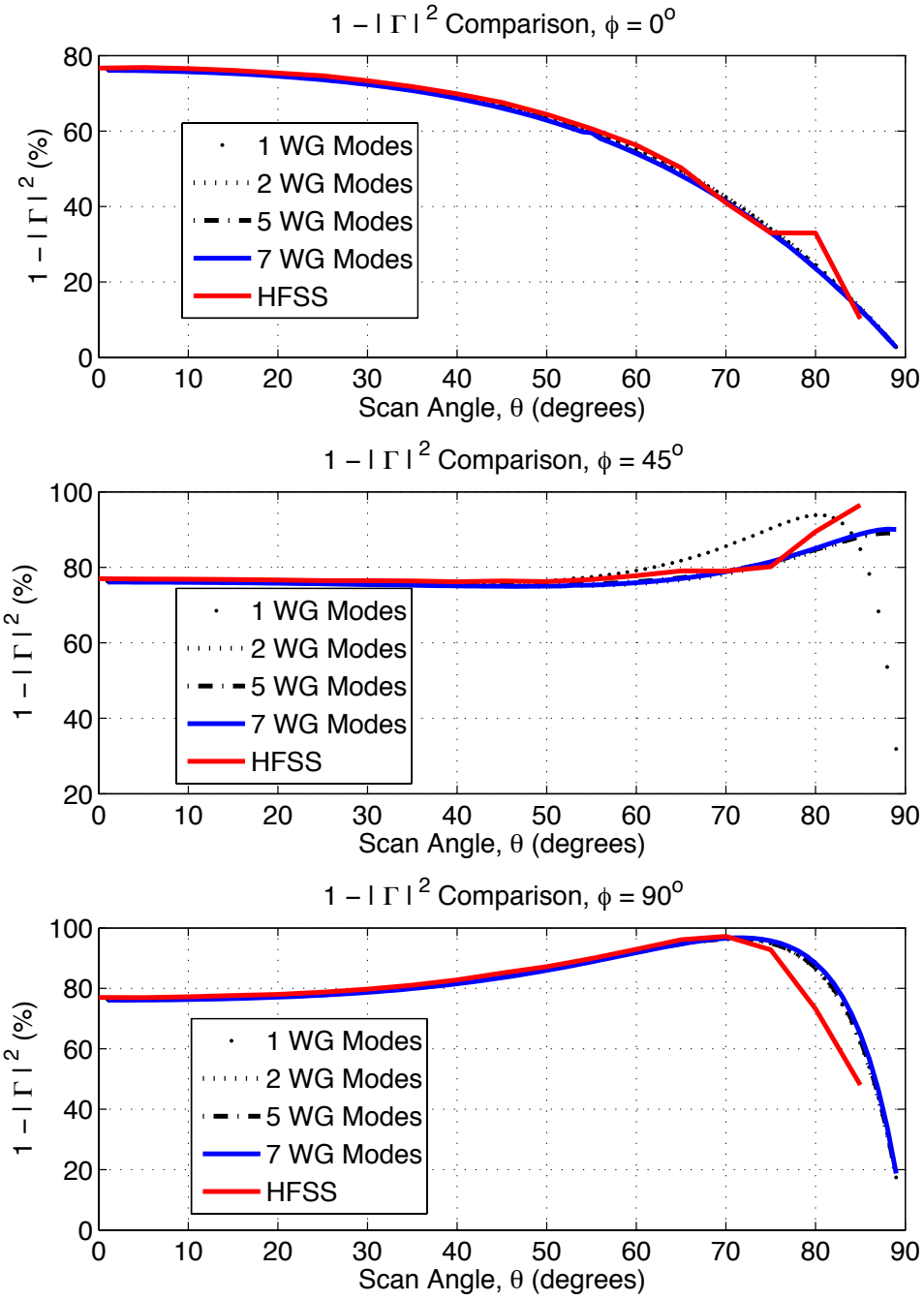

FIGURE 2.6: $(1 - |\Gamma|^2)$ results obtained using one-mode and multi-mode active element admittance models for planar array without WAIM layer(s). *(top)* $\phi = 0°$ *(mid)* $\phi = 45°$ *(bottom)* $\phi = 90°$ plane

2.4.3 *Calculation of Y_{in} with arbitrary dielectric WAIM layer*

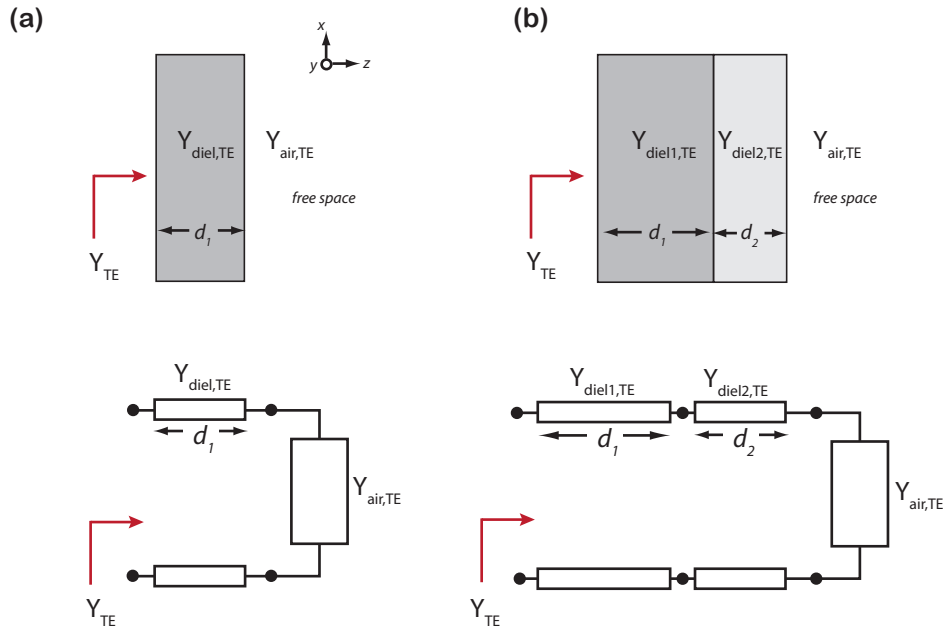

FIGURE 2.7: Transmission line equivalent of transverse admittance looking into (a) one dielectric sheet and free space half-space (b) two dielectric sheets and free space

In the presence of one or more dielectric layers, the spatial harmonic mode admittance Y_{TE} (or Y_{TM}) can be formulated using the well-known transmission line impedance transformation equations. These equations are used by engineers to transform the impedance of one end of a transmission line system to another region of the circuit so that the effective impedance of the system can be quantified and impedance-matched. For a transmission line system with load admittance $Y_{air,TE}$ connected to a transmission line of length d and characteristic admittance $Y_{diel,TE}$ (as shown in Figure 2.7a), the effective admittance Y_{TE} is:

$$Y_{\mathrm{TE}}(|\mathbf{k}_t|) = Y_{\mathrm{diel,TE}} \frac{Y_{\mathrm{air,TE}} + jY_{\mathrm{diel,TE}} \tan |\mathbf{k}_t| d_1}{Y_{\mathrm{diel,TE}} + jY_{\mathrm{air,TE}} \tan |\mathbf{k}_t| d_1} \tag{2.45}$$

$\mathrm{Y_{air,TE}}$ and $\mathrm{Y_{diel,TE}}$ in Figure 2.7a are the transverse admittances that can be obtained by plugging in the constitutive parameters of air ($\epsilon_r = 1$, $\mu_r = 1$) and the dielectric material (ϵ_r =?, $\mu_r = 1$, d_1 =?) each into (B.14) of Appendix B. To calculate $\mathrm{Y_{TE}}$ (or $\mathrm{Y_{TM}}$) in the presence of a two-layer (or multi-layer) dielectric WAIM topology (as shown in Figure 2.7b), (2.45) is applied recursively. Note that $|\mathbf{k}_t|$ represents the lattice of grating lobes $|\mathbf{u}_{opq}|$, thus, as many transverse admittance values as there are grating lobes must be calculated for each scan angle; e.g. if we are taking forty-nine grating lobe terms into account ($|p|_{\max} = |q|_{\max} = 3$), then we must also compute forty-nine $\mathrm{Y_{TE}}$ (or $\mathrm{Y_{TM}}$) terms per scan angle.

In Figure 2.8 are viewgraphs for $(1 - |\Gamma|^2)$ obtained for the planar phased array in the presence of a dielectric WAIM sheet with relative permittivity $\epsilon_r = 3$, and thickness $d_1 = 4.3mm$ placed directly on the array surface. A cursory inspection of the results show that the one-mode model, vis-a-vis the multi-modal models, poorly agrees with full-wave simulations. In particular, a stark disagreement occurs between the one-model or two-model model and the exact solution at all azimuthal planes, especially beyond $\theta = 30^\circ$ on the $\phi = 0^\circ$ plane. This suggests that several waveguide modes must be taken into consideration in order to obtain accurate results. We can see from Figure 2.8 that the inclusion of the first seven waveguide modes ($\mathrm{TE_{11}}$, $\mathrm{TE_{11}}$ cross-polarized, $\mathrm{TM_{01}}$, $\mathrm{TE_{21}}$, $\mathrm{TE_{21}}$ cross-polarized, $\mathrm{TM_{11}}$, $\mathrm{TM_{11}}$ cross polarizes) clearly delivers accurate results.

In a similar vein, Figure 2.9 depicts viewgraphs of $(1 - |\Gamma|^2)$ performance of the planar phased array in the presence of two dielectric WAIM sheets. The results obtained using the one-mode model and the multimode models are consistent with Figure 2.8.

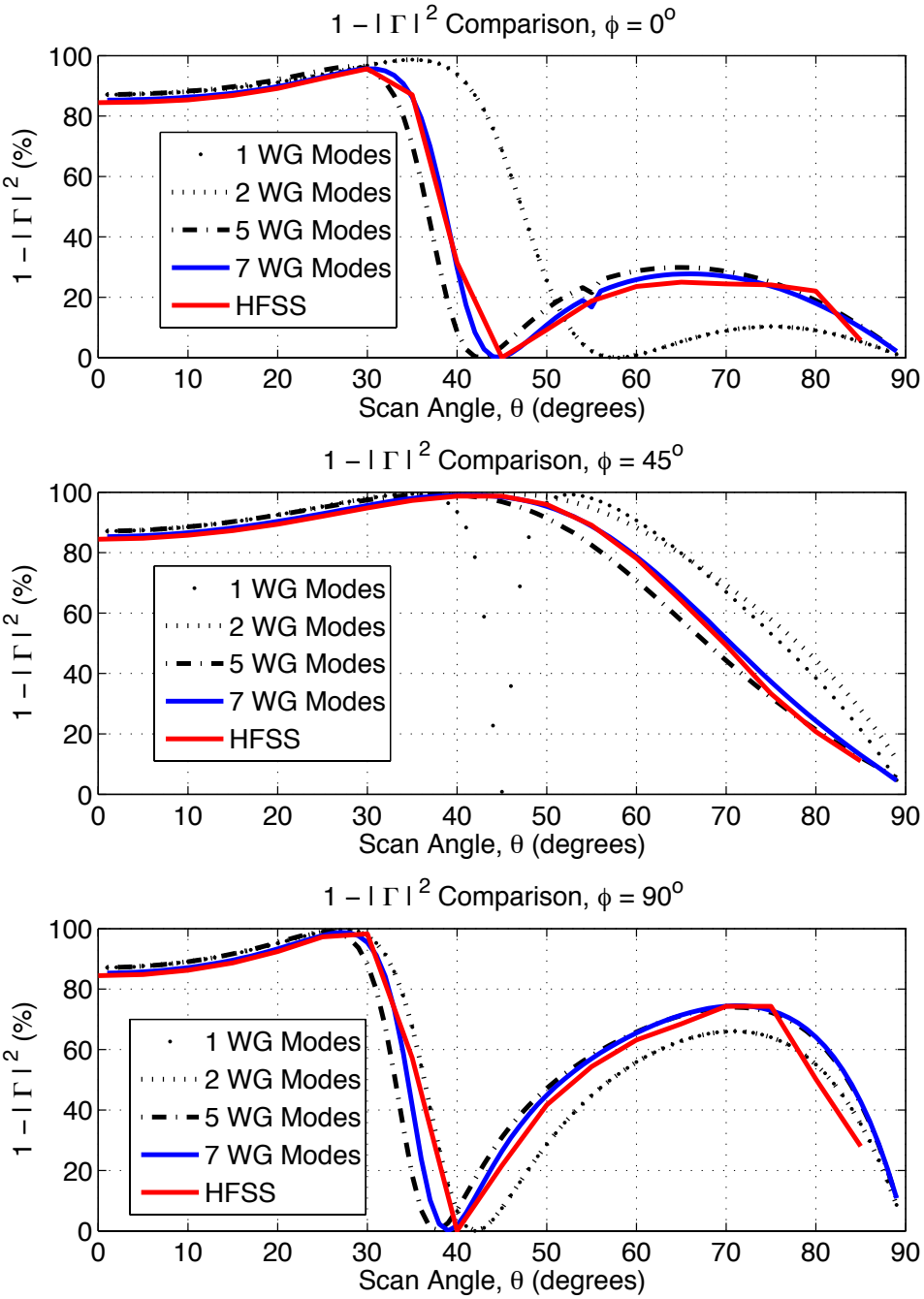

FIGURE 2.8: $(1 - |\Gamma|^2)$ results obtained using one-mode and multi-mode active element admittance models for planar array with dielectric WAIM sheet with parameters $\epsilon_r = 3$, $d_1 = 4.3mm$ placed on the array surface. *(top)* $\phi = 0°$ (H-Plane) *(mid)* $\phi = 45°$ (D-Plane) *(bottom)* $\phi = 90°$ (E-Plane)

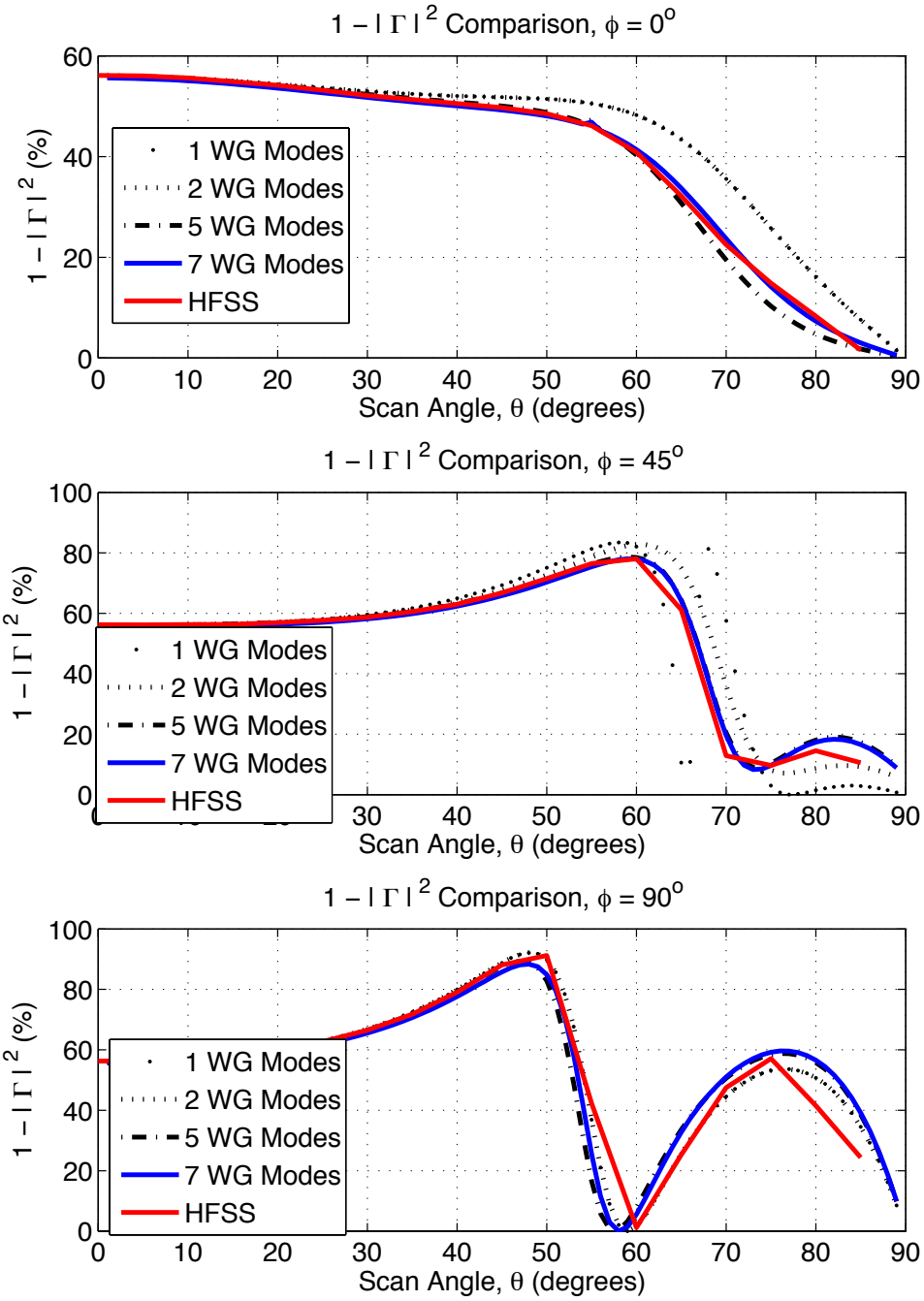

FIGURE 2.9: $(1 - |\Gamma|^2)$ results obtained using one-mode and multi-mode active element admittance models for planar array with two dielectric WAIM sheets with the layer directly placed on the array surface having parameters $\epsilon_r = 1.6$, $d_1 = 3mm$, and the top layer having parameters $\epsilon_r = 3$, $d_2 = 3mm$. *(top)* $\phi = 0°$ (H-Plane) *(mid)* $\phi = 45°$ (D-Plane) *(bottom)* $\phi = 90°$ (E-Plane)

2.5 Calculating Y_{in} in the presence of anisotropic WAIM layers

2.5.1 Obtaining anisotropic media using transparent crystals

Before we delve into the calculation of the active element admittance, let us first discuss the different ways to obtain anisotropic materials. Anisotropic materials are available in nature especially in the form of uniaxial (e.g. calcite) or biaxial crystals, which, in the words of Born and Wolf [50], *have less than three crystallographically-equivalent, mutually-orthogonal directions*. Isotropic crystals have a cubic system such that $\epsilon_x = \epsilon_y = \epsilon_z = \epsilon_r$; uniaxial crystals have two crystallographically-equivalent mutually-orthogonal directions such that $\epsilon_x = \epsilon_y \neq \epsilon_z$, while biaxial crystals have no mutually-orthogonal directions that are crystallographically equivalent ($\epsilon_x \neq \epsilon_y \neq \epsilon_z$). The dispersion surface (not shown) of an isotropic material is spherical while it is ellipsoidal for a biaxial material and spheroidal for a uniaxial material. A sphere has an infinite number of optical axes (an optical axis is a line along which there is rotational symmetry), a spheroid has one optical axis, and an ellipsoid has two optical axes. An inspection of the dispersion relation of uniaxial materials derived in (B.5) and (B.11) of Appendix B show equations that are structurally spheroidal. The dispersion relation of isotropic materials, which has spherical form, can be obtained from (B.5) and (B.11) by setting all the permittivity values to ϵ_r and all the permeability values to μ_r.

2.5.2 Implementing artificial anisotropic electromagnetic media using metamaterials

Apart from the anisotropic crystals available in nature, the field of metamaterials enables the capability to design artificial electromagnetic materials that are anisotropic to magnetic or electric fields. As we have discussed in the first chapter, a metamaterial is made up of arrays of subwavelength resonant structures that, by coupling to an applied electric or magnetic field, can excite in itself an average electric or

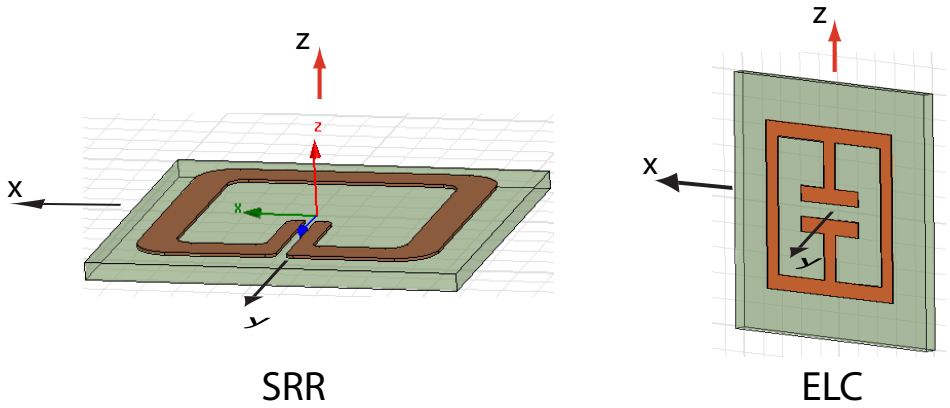

FIGURE 2.10: SRR and ELC denoting axis of excitation in red.

magnetic constitutive response. In principle, the complete electromagnetic behavior of a metamaterial can be described by a bulk permittivity and/or permeability that can be calculated using standard parameter retrieval techniques [7,51]. Because most metamaterial structures are made to couple to electric or magnetic fields in just one or two directions, they are by nature anisotropic. For example, a simple SRR possesses a magnetic response only in the direction perpendicular to its plane, while a simple ELC has a strong electric response in the direction along its capacitive gap. Figure 2.10 depicts an SRR and ELC and indicates the direction of artificial magnetic and electric constitutive parameters. The effective performance of an SRR media would engender an anisotropic permeability; this is because the magnetic response occurs only in the $\hat{z}$ direction. Such media would have an permittivity of the form $\epsilon_x = \epsilon_y = \epsilon_z = \epsilon_r$, and a permeability of the form $\mu_x = \mu_y = 1 \neq \mu_z$. For the ELC media represented in Figure 2.10, the constitutive description is of the form $\epsilon_x = \epsilon_y = \epsilon_r \neq \epsilon_z$ and $\mu_x = \mu_y = \mu_z = 1$.

Anisotropic media implemented using metamaterials provide flexibility because they may be designed to have engineerable constitutive parameters in every direction. It is remarkable that, in comparison to uniaxial crystals, metamterials can be used to

obtain artificial materials that are simulataneously uniaxial to magnetic and electric fields, i.e. $\epsilon_x = \epsilon_y \neq \epsilon_z$ and $\mu_x = \mu_y \neq \mu_z$. A material with an engineerable permittivity and permeability can be obtained by using a metamaterial unit cell that simultaneously engenders a magnetic and electric response, or by integrating a magnetic particle and electric particle in the same unit cell. The possibility of designing materials with sophisticated anisotropic properties motivates the effort to explore the use of anisotropic WAIM layers for impedance-matching planar phased array antennas.

2.5.3 Incorporating Anisotropy into One-Mode or Multi-Modal model

To implement the one-mode or multimodal model for a planar array with one or more anisotropic layers, the effective spatial harmonic transverse admittances, $\mathrm{Y_{TE}}$ and $\mathrm{Y_{TM}}$, are the only parameters that are modified. To incorporate anisotropic layers, the *characteristic* transverse admittance of the anisotropic material is calculated, and thereafter the transmission line impedance transformation equation is used to exactly transform the impedance from the load (air) through the anisotropic layer to the array surface. The procedure visually illustrated in Figure 2.7 is repeated, with the exception that the admittance of the anisotropic material(s) have a different form.

The *characteristic* transverse admittance of spatial harmonics propagating in an infinitely thick uniaxial anisotropic material is derived in Appendix B. These admittances can be expressed as:

$$Y_{\mathrm{TE}}(|\mathbf{k}_t|) = \sqrt{\frac{\epsilon_0\epsilon_y}{\mu_0\mu_x} - \frac{|\mathbf{k}_t|^2}{\omega^2\mu_0^2\mu_x\mu_z}} \tag{2.46}$$

and,

$$Y_{\mathrm{TM}}(|\mathbf{k}_t|) = \left[\sqrt{\frac{\mu_0\mu_y}{\epsilon_0\epsilon_x} - \frac{|\mathbf{k}_t|^2}{\omega^2\epsilon_0^2\epsilon_x\epsilon_z}}\right]^{-1} \tag{2.47}$$

The analysis of uniaxial anisotropic materials (instead of fully anisotropic materials where $\mu_x \neq \mu_y \neq \mu_z$ and/or $\epsilon_x \neq \epsilon_y \neq \epsilon_z$) is doubly convenient because these materials are not impossible to implement using metamaterials, and because they are also less complex to integrate with the grating lobe or cross-grating lobe series that make up the one-mode and multimodal admittance models. Apart from the extreme difficulty inherent in making fully anisotropic metamaterials, using uniaxial materials makes it straightforward to derive spatial harmonic admittance terms $\mathrm{Y_{TE}}$ and $\mathrm{Y_{TM}}$ from Maxwell's equations. (We set the constitutive parameters in the plane of the array surface are equal, i.e. $\epsilon_x = \epsilon_y$ and $\mu_x = \mu_y$.)

2.5.4 Accuracy of Multi-Modal model

As can be seen from comparing the accuracy of the one-mode model in Figure 2.6 with the one-model in Figure 2.8, the number of modes needed in order to obtain an accurate approximation of $\mathrm{Y_{in}}$ depends on the material placed on the array surface. We find that more modes may need to be taken into account when anisotropic layers with certain properties are used. For instance, for a material with $\epsilon_x = \epsilon_y = 1.95$, $\epsilon_z = 1$, $\mu_x = \mu_y = 1$, $\mu_z = 3.78$ and $d_1 = 4.1mm$, the results (shown in Figure 2.11) do not converge rapidly as the number of modes is increased, unlike the results shown in Figure 2.12 which are essentially of the same material except that μ_z has been changed from $\mu_z = 3.78$ to $\mu_z = 1$. This expectedly suggests that the constitutive nature of an anisotropic WAIM layer determines the influence of higher order modes on the active element admittance of the planar phased array. Our analyses of the use of the multi-modal model to analyze anisotropic materials show that a higher number of waveguide modes may need to be taken into account to obtain accurate

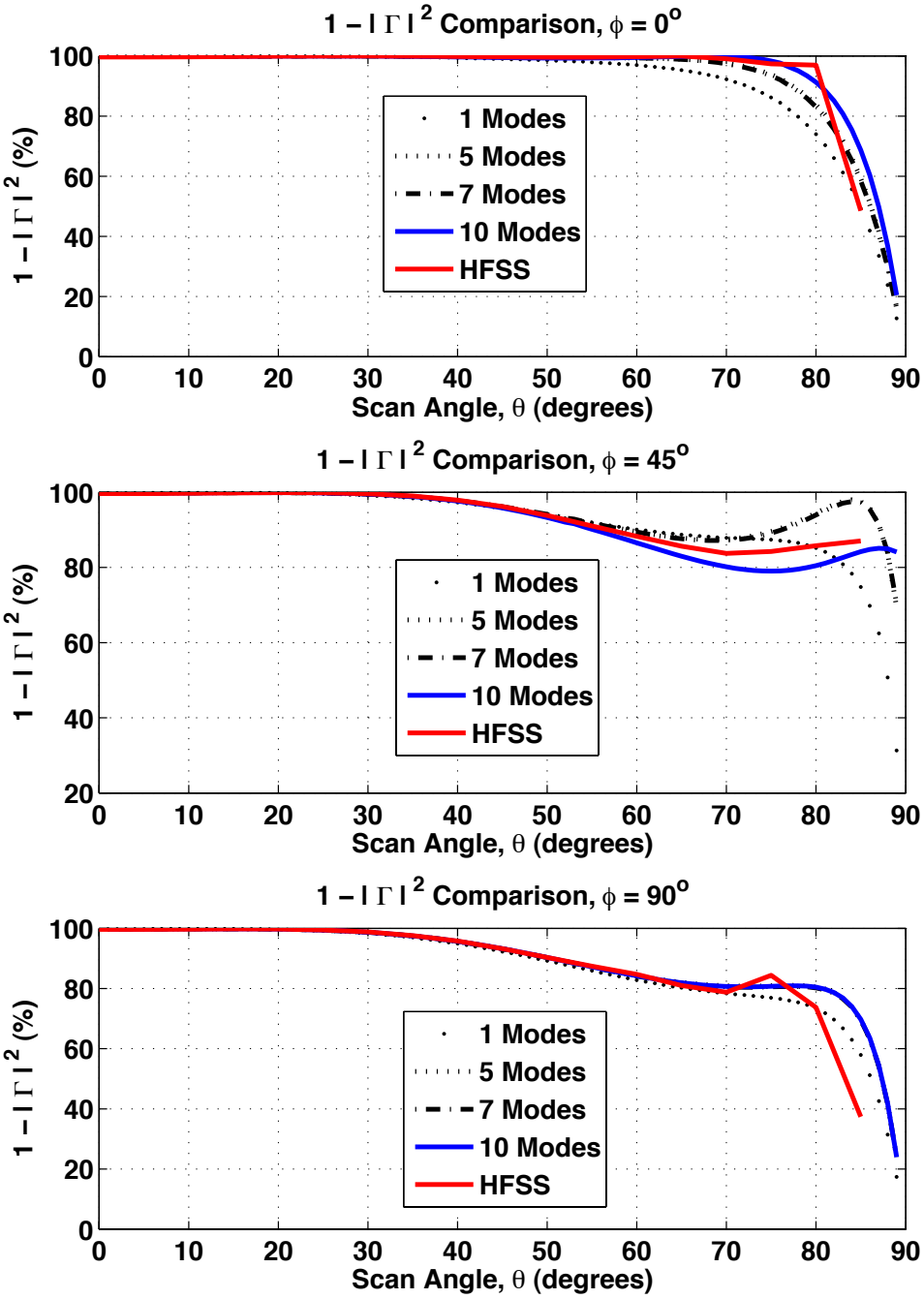

FIGURE 2.11: $(1 - |\Gamma|^2)$ results obtained using one-mode and multi-mode active element admittance models for planar array with one anisotropic WAIM layer with parameters $\epsilon_x = \epsilon_y = 1.95$, $\epsilon_z = 1$, $\mu_x = \mu_y = 1$, $\mu_z = 3.78$ and $d_1 = 4.1mm$ placed on the array surface. *(top)* $\phi = 0°$ (H-Plane) *(mid)* $\phi = 45°$ (D-Plane) *(bottom)* $\phi = 90°$ (E-Plane)

results.

We especially observed that anisotropic materials made up of a mix of positive and negative values for constitutive parameters (e.g. *indefinite* media [52, 53]) when used as WAIMs pose a convergence problem to the grating and cross-grating lobe series. This is because these materials natively support evanescent plane wave modes, and this implies that one would need to include an unrealistically large number of grating lobes (i.e. really large values for $|p|_{\max}$ and $|q|_{\max}$). Comparisons of results from HFSS simulations and the multimodal MATLAB model do not show consistent agreement even when a large number of grating lobes and waveguide modes are included. In addition, the HFSS simulations do not seem to converge gracefully, and whenever HFSS results seem to converge, we found that the use of *indefinite* media as anisotropic WAIM layers predisposes the phased array to total scan blindness at multiple angles, a phenomenon which can occur when the transmitted energy is trapped either as a surface wave on the surface of the planar array or inside a WAIM placed on the surface of the array. In order to obtain highly accurate results, it is important to use a high number of waveguide modes. Based on the findings discussed in this section, we generally decided to use between ten and fourteen waveguide modes to characterize the performance of the planar phased array of waveguide apertures.

2.6 Conclusion

In this chapter we discussed the characterization of a planar array of circular waveguide arrays through a decomposition of the free space modes into homogenous and inhomogenous (grating lobe series), quantifying their role in the mutual cross-interaction between higher-order waveguide modes excited on the array surface. The matrix of mutual admittances calculated was subsequently used to calculate the radiation admittance at the aperture junction of a waveguide element at the center of a very large array. This analysis was performed with the assumption that the circular waveguide

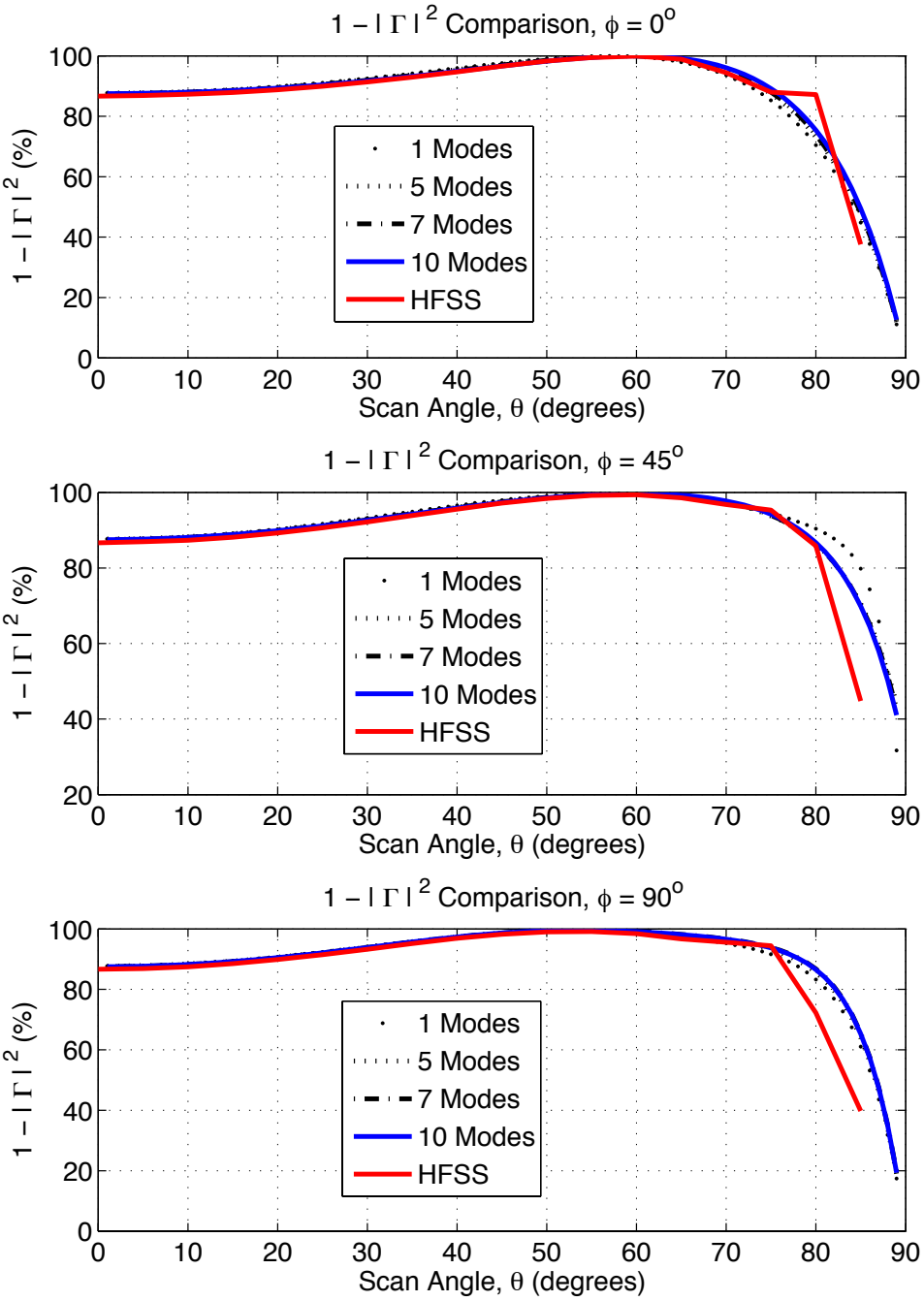

FIGURE 2.12: $(1 - |\Gamma|^2)$ results obtained using one-mode and multi-mode active element admittance models for planar array with one anisotropic WAIM layer with parameters $\epsilon_x = \epsilon_y = 1.95$, $\epsilon_z = 1$, $\mu_x = \mu_y = 1$, $\mu_z = 1$ and $d_1 = 4.1mm$ placed on the array surface. *(top)* $\phi = 0°$ (H-Plane) *(mid)* $\phi = 45°$ (D-Plane) *(bottom)* $\phi = 90°$ (E-Plane)

elements of the planar phased array are fed with a $\hat{y}$-polarized feed which excites a propagating TE_{11} mode that is primarily polarized along the $\hat{y}$-direction. For an array consisting of cross-fed waveguides (i.e. fed with orthogonal feeds, thus resulting in both $\hat{x}$ and $\hat{y}$-polarized TE_{11} modes carrying power), the active element admittance for each mode must be calculated separately, however, these admittances may not be the same if the array does not have a square lattice geometry. To calculate the active element admittance for the $\hat{x}$-polarized TE_{11} mode, the Fourier transform of that mode field distribution (ξ_ρ and ξ_ψ) and its accompanying higher order modes should be rotated by -90°.

The primary aim of carefully developing the formulation for the active element admittance was to characterize planar phased array in the presence of metamaterials, which may be modeled as anisotropic materials. To implement the mathematically formulated model, a MATLAB code was written to compute the transmission and reflection performance of a planar array of circular waveguide apertures in the presence of one or more dielectric or anisotropic material layers.

By creating a MATLAB model we are able to calculate Y_{in} expeditiously. As an example, a full-wave solution (using *Ansoft* HFSS™) of the planar array topology of Figure 2.5 to obtain the results in Figure 2.12 expends fifty minutes of computation time, while the MATLAB code expends only five seconds when forty-nine free space modes and ten waveguide modes are included.

In the next chapter we examine the use of numerical optimization to determine anisotropic WAIM constitutive parameters that match the impedance of the phased array over a broad range of scan angles. The fast run time of the MATLAB model enables us to be able to perform such an optimization in a feasible amount of time, since we expect that the numerical optimization algorithm may need to run thousands of iterations of the MATLAB model before arriving at an optimal set of constitutive parameters values.

3

Using Anisotropic Materials to obtain Wide Angle Impedance Matching in Planar Phased Array Antennas

In the previous chapter, we discussed the methodology used to accurately compute the active element admittance of a waveguide-fed planar phased array antenna. We also discussed the use of this approach to characterize the transmission performance of a planar phased array antenna in the presence of a stack of dielectric or anisotropic impedance matching material. The use of dielectric layers on planar arrays to address reflections at the array surface was first introduced by Magill [39] and is a common approach used to optimize the power transmission ratio as a function of scan.

Ideally, the desired power transmission ratio for a planar phased array antenna is obtained when all the power fed into the phased array antenna is radiated out into free space, leading to a zero reflection coefficient ($|\Gamma(\theta, \phi)|$) for all scan conditions. However, due to mutual coupling between antenna elements, it is difficult, if not impossible, to achieve $|\Gamma(\theta, \phi)|$ of zero at all combinations of elevation and azimuthal scan angles. To improve the impedance match over a broad range of scan angles, an intervening set of thin dielectric layers can be introduced on the surface of the array.

The number of layers, their thicknesses and placement are all optimized to provide the best possible match over as broad an angular scan range as possible.

Wide-angle impedance matching (WAIM) structures constructed from layers of dielectric materials are beneficial in addressing the impedance mismatch associated with phased array antennas. However, currently available materials exhibit a fairly restricted range of dielectric constants and it is expected that access to a larger range of constitutive properties—including magnetic permeability values—would offer further advantages in the design of WAIM layers.

Metamaterials, or structured materials, have the advantage that they can be designed with permittivity and permeability values over a continuum of values [14, 15], and provide access to material properties such as anisotropy that are not readily available in most usable WAIM dielectric materials. This wider range of material properties presents opportunities to obtain more comprehensive impedance matching for phased array antennas. Heuristically, anisotropic materials, implementable using metamaterials, should improve the ease of matching array antennas over a broader range of scan angles.

The goal of this chapter is present a systematic technique to design anisotropic wide angle impedance matching layers that may be implementable using metamaterials. The multimodal model developed in Chapter 2 is used to generate anisotropic material parameters that provide wide angle impedance matching for a given phased array configuration. The existing method of dielectric WAIM layer optimization is extended to allow for (i) a wider range of values for ϵ, (ii) non-unity permeability μ, and, (iii) to accommodate anisotropic values of ϵ and μ. These configurations can be accomplished using metamaterials.

In the next sections, the methodology used to prescribe optimal anisotropic WAIMs and the proper design rules that must be followed are discussed. Several examples of the use of a uniaxial anisotropic layer(s) to optimize the array power

transmission ratio are also presented. At the end of this chapter, the results of a numerical and experimental analysis are used to examine the feasibility of using a metamaterial as an anisotropic WAIM over a phased array surface. Finally, some of the challenges associated with using metamaterials in the phased array WAIM context, are also discussed.

3.1 Optimization of Anisotropic Impedance Matching Layers

The purpose of using anisotropic WAIMs is to minimize $|\Gamma(\theta, \phi)|$ over a very broad range of scan angles. From the multi-modal technique discussed in Chapter 2 (refer to Appendix A for complete derivation), we implemented a MATLAB code to compute the active element admittance and reflection coefficient. By optimizing the design variables of the anisotropic WAIM layer(s), the reflection coefficient can be minimized. We can therefore express the desired goal of the optimization to be:

$$\texttt{minimize} \int_{\phi=0^\circ}^{90^\circ} \int_{\theta=0^\circ}^{90^\circ} \left| \frac{Y_{TE_{11}} - Y_{\text{in}}(\phi, \theta)}{Y_{TE_{11}} + Y_{\text{in}}(\phi, \theta)} \right|^2 d\theta d\phi \tag{3.1}$$

Note that the integrand of (3.1) is $|\Gamma(\theta, \phi)|^2$, which is the parameter that we aim to minimize over all scan angles. To minimize this function, the active element admittance at the array surface (at the aperture discontinuity) must equal the admittance of the waveguide fundamental propagating mode (TE_{11} mode). This condition can be expressed as:

$$Y_{\text{in}}(\theta, \phi) = Y_{TE_{11}} \tag{3.2}$$

for all θ and ϕ between zero degrees and ninety degrees.

3.1.1 Implementation of Optimization in MATLAB

Because the function $|\Gamma(\theta, \phi)|^2$ is not expressed in closed form, we choose to numerically optimize this objective function using a built-in computational optimization algorithm (`fmincon`). MATLAB's `fmincon` function is a constrained optimization routine that can be used to minimize the objective function of (3.1). `fmincon` accepts a variety of inputs: it accepts the parameterized function that needs to be optimized, the domain of design variables (for a uniaxial anisotropic layer these parameters are: μ_x, μ_z, ϵ_x, ϵ_z, and the thickness d_1 of the layer). A constrained optimization routine is used because we limit the search domain for μ, ϵ and thickness. `fmincon` uses line-search, quasi-newton, and sequential programming algorithms to numerically find the minimum from a given starting point seed which must be provided for each design variable.

To prescribe optimal anisotropic layers, the multi-modal model was interfaced with `fmincon` and optimized in MATLAB over several iterations. For each iteration the optimization function increments or decrements the values of the design variables such that the objective function is further reduced in value. A set of starting values for the design variables from which the optimization can begin its search are defined, but different starting values may yield different optimization results. We use a Monte-Carlo optimization scheme to stochastically generate sets of starting values for the design variables to alleviate such dependence. The Monte-Carlo scheme generates several sets of starting values and results in as many sets of optimized design variables as there are sets of starting values. Because many of the optimized design values will only be local minima, the smallest minimum of all the resulting minima is assumed to be the absolute minimum of the objective function. Specifically, 500 sets of design variables starting points (i.e. 500 sets of μ_x, μ_z, ϵ_x, ϵ_z, and the thickness) are randomly generated using a multivariate uniform probability density function. A

flow chart of the optimization with and without the Monte-Carlo scheme is shown in Figures 3.1 and 3.2.

One important detail that should not be overlooked in Figure 3.1 is the definition of the initial variables and terms at the beginning of the flowchart sequence. The placement of the definition of these terms is very important. For instance, the dependence of circular waveguide Fourier transform terms ($\xi_{\psi}(\mathbf{u}_{\circ pq})$ and $\xi_{\rho}(\mathbf{u}_{\circ pq})$) on Bessel functions implies that, since the evaluation of Bessel functions is computationally expensive, placing them within the optimization loop would significantly slow down the execution of each iteration of the multi-modal code runtime. We have found that the evaluation of the Fourier transform terms is responsible for 85% to 95% of the multi-modal model code runtime. Therefore, predefining these terms before executing the optimization routine can dramatically reduce the runtime of each iteration invoked by `fmincon`. In addition, because the multi-modal model uses a large number of spatial harmonic and waveguide mode terms we found it necessary to eliminate the use of loops to expedite run time. For example, to calculate $\mathrm{Y_{in}}$ for, say, fourteen waveguide modes, forty-nine spatial harmonic terms, eighty elevation scan angles, and three azimuthal planes, one would otherwise have to deal with over 2.3×10^6 loops! (i.e. $7 \times 7 \times 14 \times 14 \times 81 \times 3$). Writing a program that leverages the multi-processor platform of contemporary computers entails replacing loops with large multidimensional matrices that enable the use of parallel processing to perform the computations.

Using the optimization methodology previously discussed, we choose to optimize the phased array antenna of Figure 2.5 over all azimuthal planes. Since the H, D, and E-planes ($\phi = 0°$, $\phi = 45°$ and $\phi = 90°$, respectively) provide an estimation of the performance of phased array systems [54] over most azimuthal planes (due to symmetry), we attempt to simultaneously optimize at these three azimuthal planes for a given number of dielectric and anisotropic layers over the array surface. We

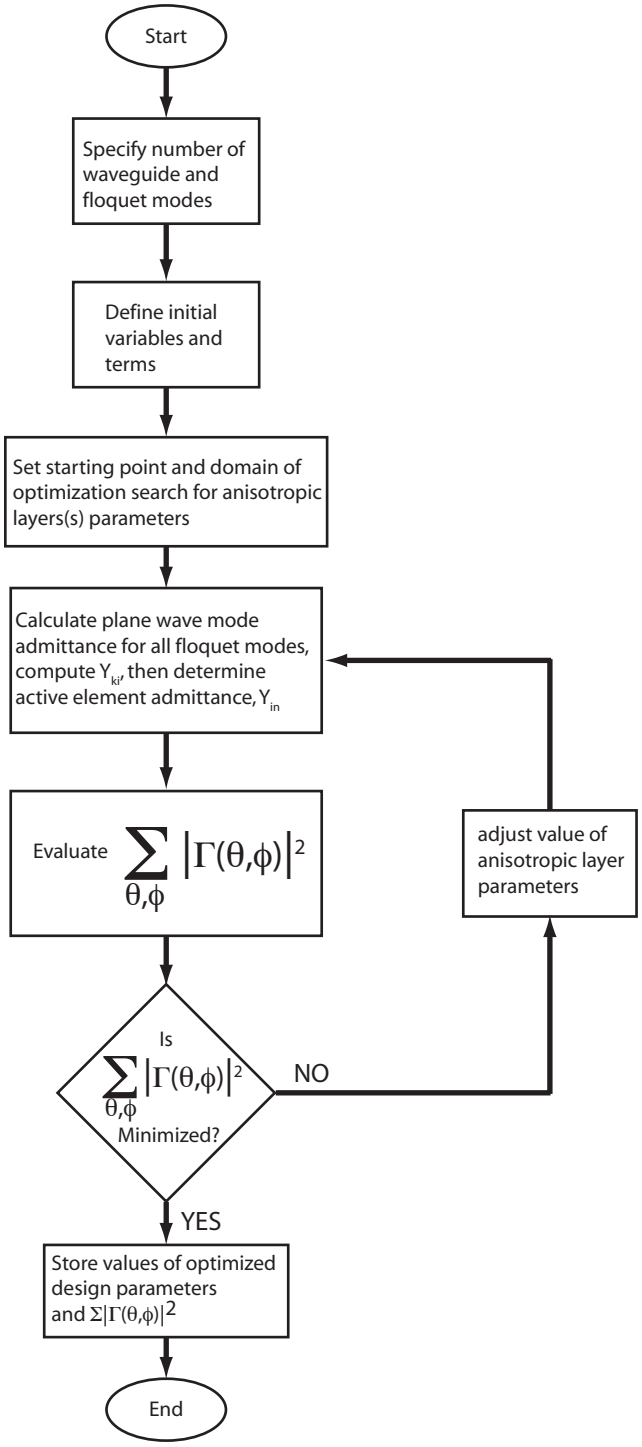

FIGURE 3.1: Flowchart illustrating operations in the MATLAB optimization model for anisotropic WAIM optimization.

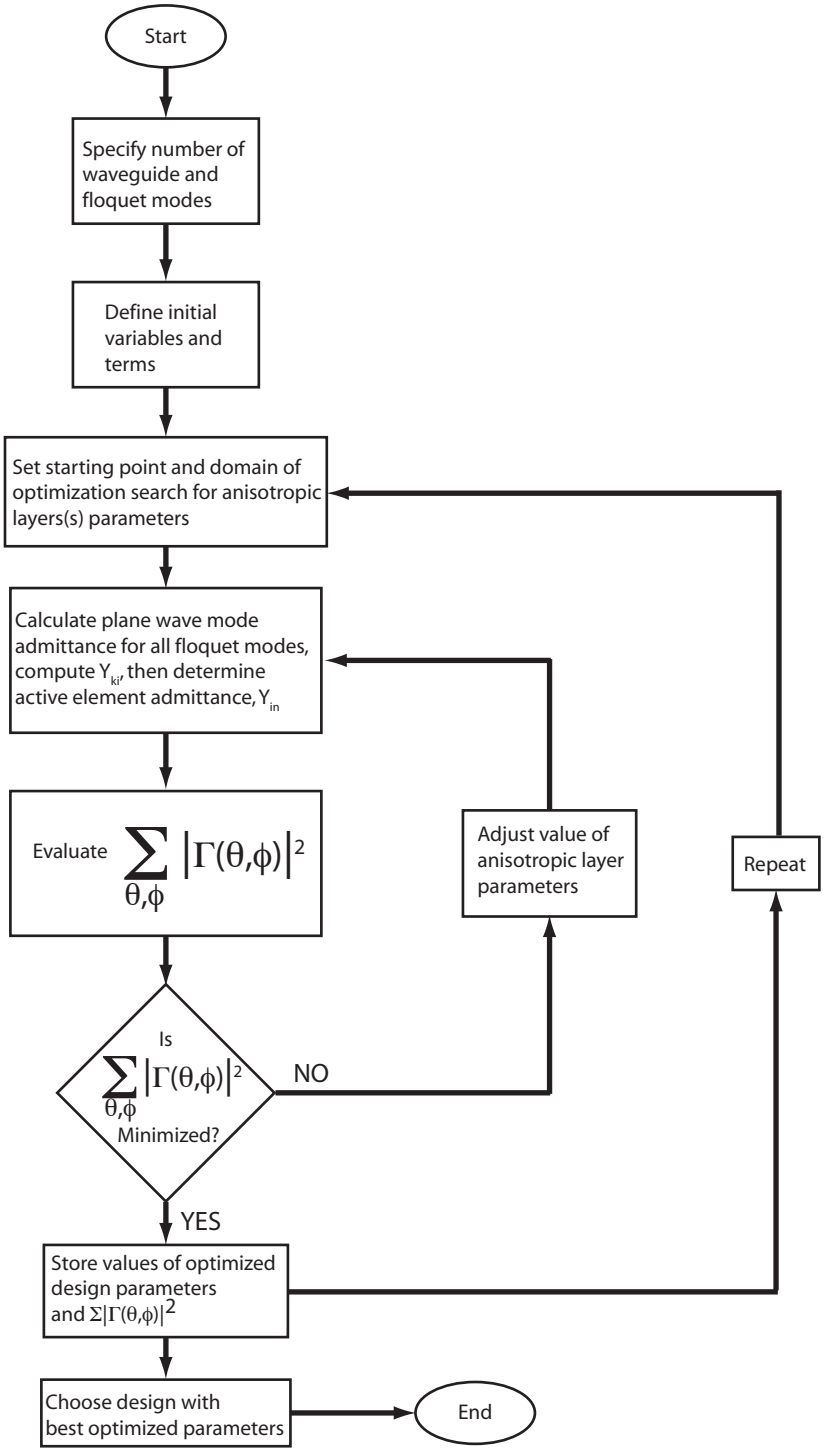

FIGURE 3.2: Flowchart illustrating operations in the MATLAB Monte-Carlo optimization model for anisotropic WAIM optimization.

modify the objective function of (3.1) to the discretized version as follows:

$$\texttt{minimize} \sum_{b=0}^{b=2} \sum_{\theta=0^\circ}^{80^\circ} \left| \frac{Y_{\mathrm{TE}_{11}} - Y_{\mathrm{in}}(45b^\circ, \theta)}{Y_{\mathrm{TE}_{11}} + Y_{\mathrm{in}}(45b^\circ, \theta)} \right|^2 \tag{3.3}$$

In addition, we reduce the scan range from $\theta = 0^\circ - 90^\circ$ to $\theta = 0^\circ - 80^\circ$ to represent the range of angles over which transmission is feasible. As discussed in Chapter 2, it is extremely to transmit or receive with the planar antenna at angles close to ninety degrees given the effective aperture reduction term $f(\theta)$ displayed in (2.1) of Chapter 2.

3.1.2 Design Rules for the Optimization of Planar Phased Arrays using Anisotropic Materials

The use of a numerical optimization approach to prescribe design variables for anisotropic impedance matching layers requires us to specify the domain of values from which the optimization algorithm can search for optimal design parameter values. Since we herein use homogenous anisotropic layers to describe metamaterials, the constitutive characteristics of these anisotropic layers must be in agreement with what is practically achievable using metamaterials.

We eliminate design variable values that would can only be implemented using extremely lossy metamaterials. The domain of permittivity and permeability values within 0.2 and 5 have been implemented successfully using metamaterials. We restrict the optimization scheme to only consider anisotropic materials with constitutive parameters within this range (i.e. ϵ or μ in the x, y or z directions may not be outside this range).

More detailed justifications for restricting the range of allowed ϵ and μ are:
(i). It is very difficult to obtain extremely high values of ϵ or μ with metamaterials

without operating within an extremely dispersive or lossy regime.

(ii). It is important to stay away from negative values of ϵ or μ because obtaining these values through metamaterials will result in highly lossy anisotropic materials.

(iii). We do not consider from constitutive parameter values that are too close to zero because these values can be difficult to fabricate because a small margin of error in fabrication may result in a large percentage difference in the effective constitutive parameter value for the metamaterial.

The above three design rules dictate the optimization search domain, while the following set of design rules are used to simplify the optimization of planar phased array antennas using anisotropic material layers. These are:

(i). It is not advisable to use indefinite anisotropic media [52] as anisotropic WAIMs because at angles in which these materials are cutoff, the excitation of a large number of evanescent modes is likely, thus potentially leading to the propagation of surface waves. The self- and cross-grating lobe series of the multimodal model converges very slowly when an unusually large number of spatial harmonic modes have to be considered.

(ii). The use of all-negative anisotropic materials is avoided because although these materials may in simulation appear to provide superior impedance matching, this result is unreliable because of very high losses. Large losses imply a large imaginary part of ϵ or μ, which leads to an inaccurate estimate of the impedance matching given that losses are assumed to be small in the implemented model and optimization scheme.

(iii). We find it computationally convenient to assume the use of uniaxial anisotropic layers of the form $\epsilon_x = \epsilon_y \neq \epsilon_z$ and $\mu_x = \mu_y \neq \mu_z$ for impedance matching, especially given that this anisotropic configuration is particularly compatible with the formulation of the multi-modal model discussed in Chapter 2.

Another variable that must be considered when performing an anisotropic WAIM

optimization is the thickness of each anisotropic layer. Unlike conventional materials that can have arbitrary thicknesses, metamaterials have thicknesses which increase discretely for a pre-determined unit cell size. For instance, the thickness of a metamaterial consisting of just one layer of a two-dimensional array of structures would be the height of the constituent metamaterial cell. Thus, the thickness of anisotropic layers that model metamaterials will have thicknesses that are an integer multiple of the height of one unit cell, and since one unit cell is typically between $\frac{\lambda}{10}$ and $\frac{\lambda}{6}$ in each direction (in order to be truly electrically small), we can assume that any value within this range or an integer multiple of any value within this range is acceptable as the thickness, d_1, of the anisotropic metamaterial layer.

For instance, for the 15.25GHz planar array in Figure 2.5, the only possible anisotropic layer thickness(es) must be within $1.96mm$ and $3.3mm$, or an integer multiple thereof. We thus constrain the thickness d_1 variable in the optimization program accordingly. Figure 3.3 illustrates the discretized nature of metamaterial layers.

3.1.3 Example: Optimization of Phased Array Performance on $\phi = 0^\circ$ Plane using a Single Anisotropic Layer

Before delving into the optimization of the planar phased array over multiple azimuthal planes, we shall first attempt to optimize the performance of the planar array at a single plane ($\phi = 0^\circ$), i.e., minimizing:

$$\sum_{\theta=0^\circ}^{80^\circ} \left| \frac{Y_{\mathrm{TE}_{11}} - Y_{\mathrm{in}}(0^\circ, \theta)}{Y_{\mathrm{TE}_{11}} + Y_{\mathrm{in}}(0^\circ, \theta)} \right|^2 \tag{3.4}$$

Since the goal of this optimization is not as ambitious as (3.3), we examine the feasibility of using just one anisotropic material layer with optimized design variables to achieve the desired wide angle impedance-matched performance on the $\phi = 0^\circ$

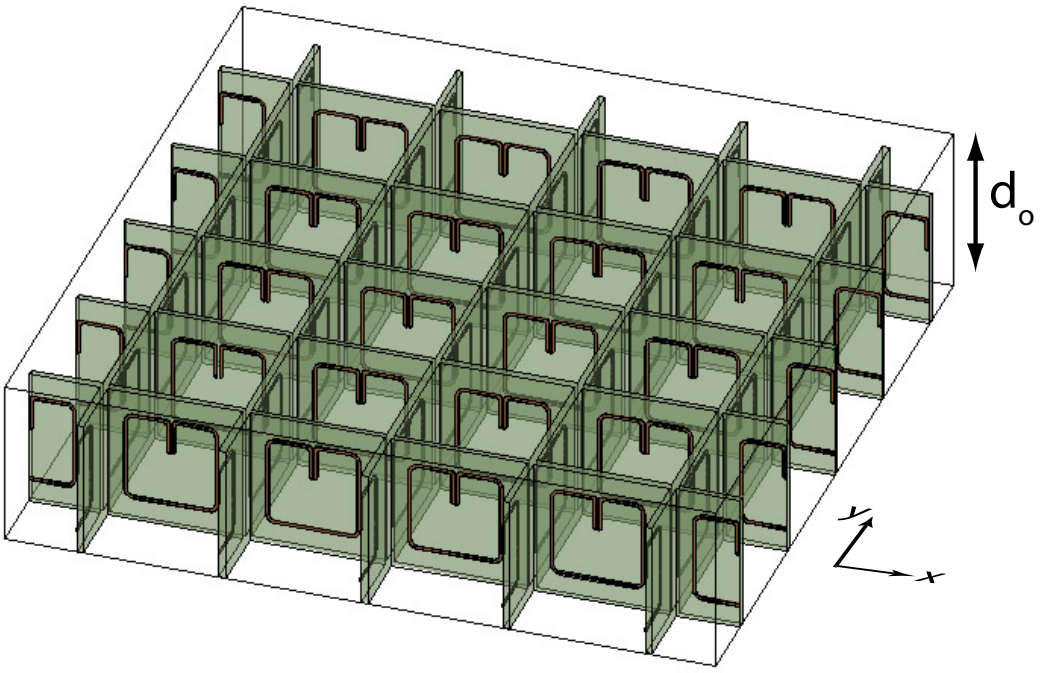

FIGURE 3.3: Single layer of metamaterial consisting of SRR particles of thickness $d_1 = d_\circ$ in the z-direction. Increments in d_1 take the form of an integer multiple of $d_\circ$.

azimuthal plane. By varying the parameters fed into the multi-modal model and calculating (3.4) at the end of each iteration (see Figure 3.1), `fmincon` arrives at a set of design variables that result in the minimum possible value for (3.4). Subsequently, the Monte-Carlo scheme illustrated in Figure 3.2 repeats the optimization process and we end up with more than one set of optimum design variables. In Figures 3.4 and 3.5, we show the transmission results obtained when an anisotropic material layer with parameters $\epsilon_x = \epsilon_y = 4.8$, $\epsilon_z = 0.5$, $\mu_x = \mu_y = 2.5$, $\mu_z = 1.3$, $d = 1.7mm$ (Figure 3.4) or with parameters $\epsilon_x = \epsilon_y = 1.95$, $\epsilon_z = 1$, $\mu_x = \mu_y = 1$, $\mu_z = 3.78$, $d = 4.1mm$ (Figure 3.5) is placed on the surface of the array surface. The reader will observe that the anisotropic parameters of the anisotropic layer used to obtain Figure 3.5 accomplishes the optimization goal by varying only $\epsilon_x = \epsilon_y$, μ_z and d_1

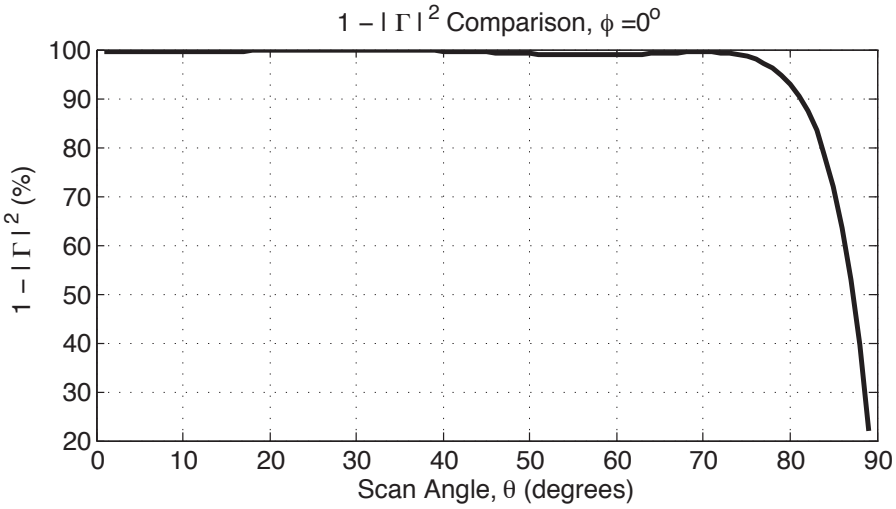

FIGURE 3.4: Optimization of phased array at $\phi = 0^\circ$ plane using anisotropic layer of parameters: $\epsilon_x = \epsilon_y = 4.8, \epsilon_z = 0.5, \mu_x = \mu_y = 2.5, \mu_z = 1.3, d = 1.7mm$.

(while keeping ϵ_z, μ_x, and μ_y fixed at 1), resulting in a design that is conceivably easier to actualize than that described by the design parameters required for the anisotropic material of Figure 3.4.

In Figure 3.6 is a plot of active element admittance $\mathrm{Y_{in}}$ of the array antenna in the presence of the anisotropic layer of Figure 3.4 in comparison with the $\mathrm{TE_{11}}$ mode admittance. We have attempted to match the active element admittance $\mathrm{Y_{in}}$ to $\mathrm{Y_{TE}}$. In accordance with (3.2) we note that there is good agreement between $\mathrm{Y_{in}}$ and $\mathrm{Y}_{TE_{11}}$ within the angular range of $\theta = 0^\circ$ and $\theta = 70^\circ$.

Thus we have shown that only one anisotropic material layer is sufficient to obtain a wide angle impedance matching on one azimuthal plane. In the next sections we explore the use of a single anisotropic layer configuration to match the array antenna at all azimuthal planes and elevation scan angles. We subsequently explore the use of a bi-layer of anisotropic materials to match the array antenna at all azimuthal planes and elevation scan angles.

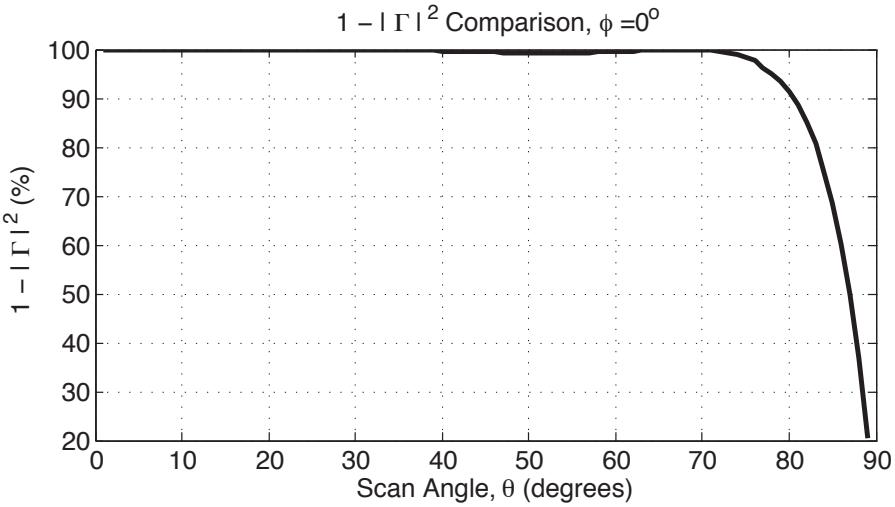

FIGURE 3.5: Optimization of phased array at $\phi = 0°$ plane using anisotropic layer of parameters: $\epsilon_x = \epsilon_y = 1.95, \epsilon_z = 1, \mu_x = \mu_y = 1, \mu_z = 3.78, d = 4.1mm$.

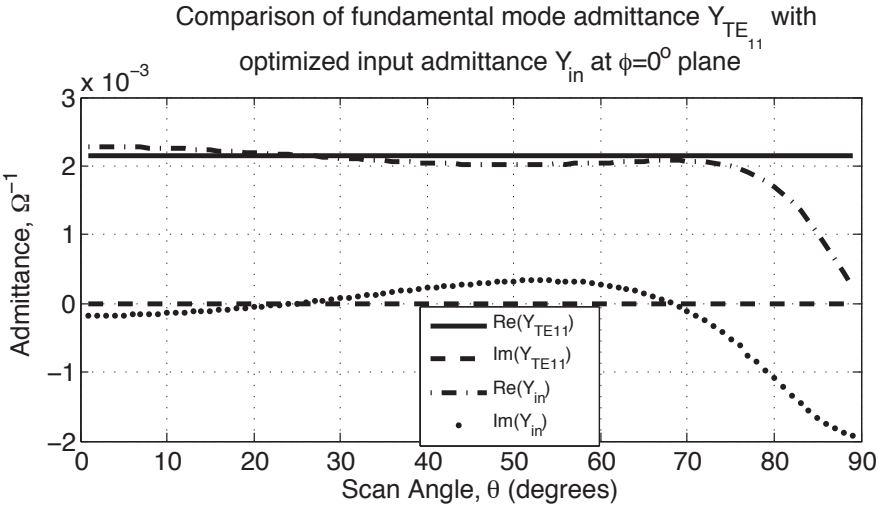

FIGURE 3.6: Comparison of $Y_{TE_{11}}$ with phased array active element admittance Y_{in} after wide angle impedance matching at $\phi = 0°$ plane using the anisotropic material of Figure 3.5.

3.2 Optimization of Phased Array Performance using Single Anisotropic Layer

The goal of this section is to examine the extent to which a single anisotropic layer can be used to match the performance of the phased array. The expression of (3.3), whose discrete summation is generally as effective but not as time-intensive as its continuous integral version in (3.1), is the objective function to be minimized. We perform the same optimization of (3.3) with a single dielectric layer we perform the same with an anisotropic layer. For the anisotropic layer, `fmincon` is allowed to vary the values of the design variables ϵ_x, ϵ_z, μ_x, μ_z between 0.2 and 5, and d_1 between $1mm$ and $5mm$ (optimum design variables with d_1 values within $\frac{\lambda}{10}$ and $\frac{\lambda}{6}$ or a multiple thereof are considered, all other sets of optimum design variables are discarded), whereas for the isotropic dielectric ϵ_r is allowed to vary from 1 to 10 and d_1 from $1mm$ to $10mm$. The range allowed for the isotropic dielectric spans the range of values of typical WAIM materials. In reality, nature does not provide the opportunity to design ϵ_r from a continuous range.

The results of the optimization for the anisotropic layer and that of the isotropic dielectric layer are shown in Figure 3.7. We find that a single anisotropic layer with design variables $\mu_x = \mu_y = 1.48$, $\mu_z = 1.97$, $\epsilon_x = \epsilon_y = 2.34$, $\epsilon_z = 0.74$, $d_1 = 3.1mm$, satisfactorily optimizes the performance of the array while for the single dielectric layer, $\epsilon_r = 2$ and $d_1 = 2mm$ are the optimum design variables. From an inspection of the results, we observe that the dielectric layer and the anisotropic layer both provide high transmission but the performance of the array with the isotropic WAIM drops off rapidly at $\theta = 30^\circ$ for the $\phi = 45^\circ$ and $\phi = 90^\circ$ planes while the dropoff occurs for the anisotropic layer at approximately $\theta = 80^\circ$ for all the azimuthal planes shown. The array transmission performance in the presence of the anisotropic and isotropic layer show significant differences: the anisotropic layer provides superior transmission.

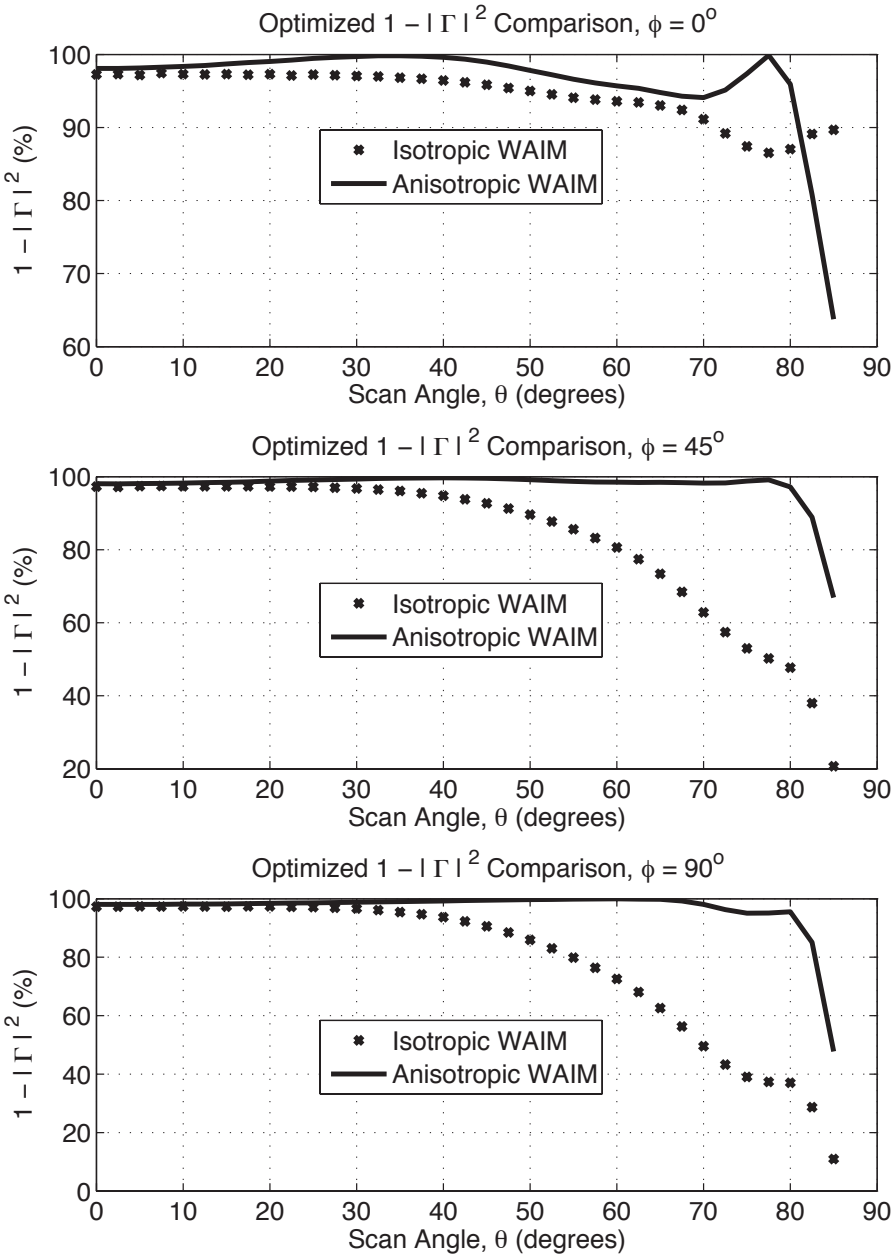

FIGURE 3.7: $(1-|\Gamma|^2)$ numerical results obtained using anisotropic WAIM material with optimized parameters $\epsilon_x = \epsilon_y = 1.95$, $\epsilon_z = 1$, $\mu_x = \mu_y = 1$, $\mu_z = 1$ and $d_1 = 4.1mm$, compared with results obtained using optimized isotropic material with parameters $\epsilon_r = 2$ and $d_1 = 2mm$. *(top)* $\phi = 0°$ (H-Plane) *(mid)* $\phi = 45°$ (D-Plane) *(bottom)* $\phi = 90°$ (E-Plane)

3.3 Optimization of Phased Array Performance using two Anisotropic Layers

Though the array performance in the presence of an optimized anisotropic material layer, as discussed in the previous section, provides better impedance matching, we explore the use of a stack of two anisotropic material layers to further improve impedance matching for the phased array. Using the previously discussed optimization scheme, the optimum design variables are $\mu_x = \mu_y = 1.43$, $\mu_z = 1$, $\epsilon_x = \epsilon_y = 2.94$, $\epsilon_z = 1.19$, $d = 2mm$ for the layer directly on the array surface, and $\mu_x = \mu_y = 1.36$, $\mu_z = 5$, $\epsilon_x = \epsilon_y = 1.4$, $\epsilon_z = 0.53$, $d = 2mm$ for the top layer. Given the use of multiple anisotropic layers, the performance of the array, as depicted in Figure 3.8, results in $(1 - |\Gamma|^2)$ values that are over 98% up to $\theta = 77^\circ$ for all the displayed azimuthal planes. It has been previously reported[1] that the best results obtainable using a multilayer stack of dielectric layers encounters a rapid dropoff in transmission at approximately $\theta = 60^\circ$. We can conclude that the use multiple anisotropic layers provides maximal performance at scan angles up to $\theta = 80^\circ$ at all azimuthal planes, compared with conventional dielectric layers.

3.4 Utilization of Metamaterials to Implement Anisotropic WAIMs over Phased Array Antenna

In Chapter 1, we presented applications of metamaterials in which a generated electric or magnetic response is used to create an artificial permittivity or permeability to implement functionalities such as negative refraction, cloaking, wave tunneling, beam steering, and beam focussing. These applications were implemented in an environment in which the polarization of the introduced electric (or magnetic) field is controlled. In addition, these experiments were set up such that the impinging

[1] For non-disclosure and intellectual property reasons, our commercial collaborator, Boeing Research and Technology, was not able to provide us with quantitative data to back up this claim of theirs.

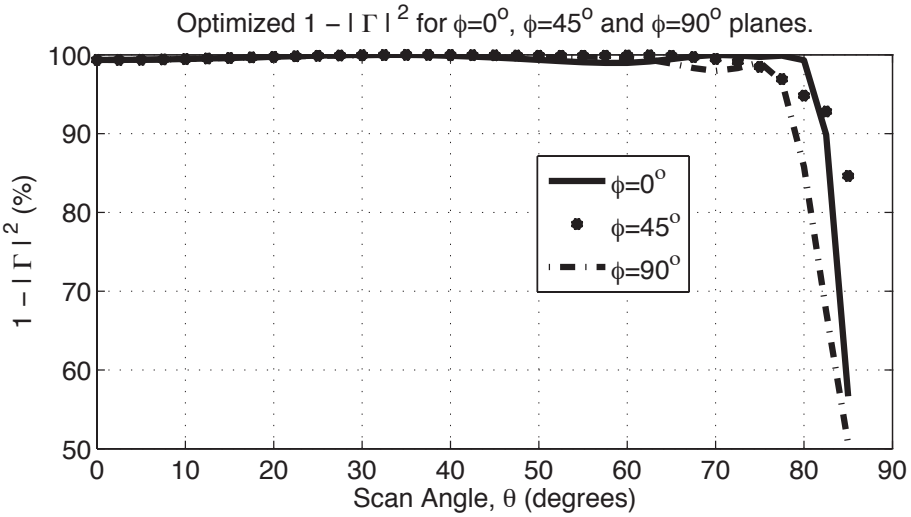

FIGURE 3.8: $(1 - |\Gamma|^2)$ numerical results obtained using two anisotropic WAIM material with optimized parameters $\epsilon_x = \epsilon_y = 2.94$, $\epsilon_z = 1.19$, $d = 2mm$, $\mu_x = \mu_y = 1.43$, $\mu_z = 1$ for the layer directly on the array surface, and $\mu_x = \mu_y = 1.36$, $\mu_z = 5$, $\epsilon_x = \epsilon_y = 1.4$, $\epsilon_z = 0.53$, $d_2 = 2mm$ for the top layer.

wave consisted primarily of homogeneous plane waves (i.e. the source is sufficiently far away from the metamaterial) thereby consistent with the parameter retrieval process[2].

The environment of the surface of a planar phased array is different from that used in the retrieval process, as the array surface harbors inhomogeneous plane wave modes (higher order spatial harmonics) that may interact differently with metamaterial structures than predicted by the retrieved anisotropic properties. Since we aim to demonstrate that a metamaterial layer can nonetheless be used as a valid anisotropic layer in the WAIM context, we perform fullwave simulations of an ELC metamaterial placed on a phased array and compare the resulting performance with the performance predicted using an effective anisotropic model.

[2] By introducing a normally incident TEM wave onto a unit metamaterial particle embedded in a PEC-PMC (or periodic boundary condition, depending on the periodic symmetry of the particles in the metamaterial) waveguide, the constitutive parameters are retrieved by performing an inversion on its reflection and transmission coefficients [7].

3.4.1 Implementation of Anisotropic WAIM using ELC Metamaterial Layer Example 1

To further verify the practicality of using an effective medium description to describe the behavior of resonant structure-based metamaterials over a phased array surface, we simulate an Electric L-C (ELC resonator) metamaterial layer designed (a detailed description of ELC resonators can be found in [8]) to have effective medium parameters of $\mu_r = 1$, $\epsilon_x = \epsilon_y = 2.58$, $\epsilon_z = 1$, and $d = 2.1mm$ at the array operating frequency of 15.25 GHz. (Superficially ELC structures may bear resemblance to the 4-legged FSS element [55], but conceptually they work in a different regime: the 4-legged FSS element is used in a manner that puts it more in the bandgap of the dispersion diagram as opposed to the ELC, which is used at much longer wavelengths relative to the unit cell size, such that homogenization applies.)

We compare these results with those from a simulation of an equivalently defined (in HFSS) homogeneous anisotropic material whose permeability and permittivity parameters are the same as that of the ELC metamaterial layer at 15.25 GHz.

Figure 3.9 shows the topology of the metamaterial WAIM setup simulated in HFSS (a square unit lattice of 10.5mm inter-element spacing is used here to computationally accommodate the square-shaped ELCs; all other operating characteristics are the same as 2.5), and also shows the constitutive parameter retrieval results for the ϵ_x and ϵ_y direction of the metamaterial. The retrieved results were derived from the scattering parameter matrix values using the method outlined in [7]. Though shaded differently in Figure 3.9, the ELC sheet is immersed in air (no substrate) and was placed at a distance $\frac{d_1}{2}$ above the aperture; the shaded region in which the metamaterial layer is immersed has a total thickness, d_1, and is used in the parameter retrieval shown in Figure 3.10. Note that ELCs are not placed directly on the array surface in order to prevent inhomogeneous plane waves and higher order waveguide

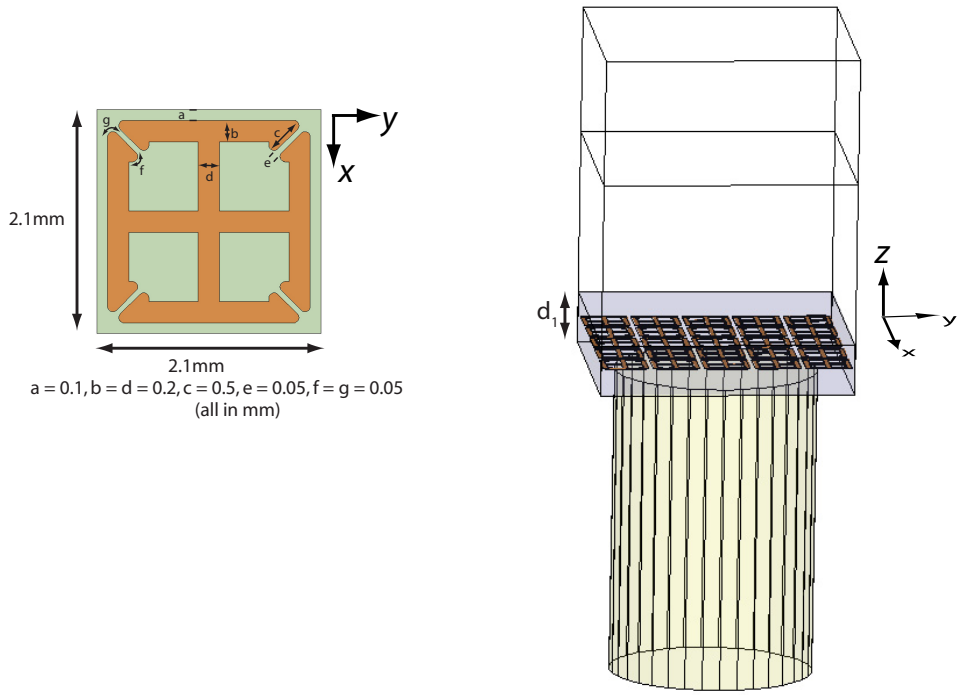

FIGURE 3.9: Topology of Phased Array Unit Lattice with ELC-based metamaterial layer. (a) Unit cell of ELC (b) Phased array unit lattice with ELC metamaterial WAIM covering; ELC sheet is placed $\frac{d_1}{2}$ away from the array surface and the effective medium homogenization is performed over d_1.

modes from strongly coupling with the ELC structures. We find that at least a 1mm gap region between the ELC and the array surface creates enough spacing for the higher order waveguide modes die out.

A comparison of the full-wave simulation of the array topology in Figure 3.9 and that of an equivalently assigned homogeneous anisotropic material is shown in Figure 3.11. There is reasonable agreement between the ELC metamaterial simulation results and the predicted results using the anisotropic model.

Example 2

In this second ELC example, an ELC-based metamaterial layer with parameters $\mu_r = 1$, $\epsilon_x = \epsilon_y = 1.9$, $\epsilon_z = 1$, and $d_1 = 2.1mm$ placed $2.1mm$ above the array is

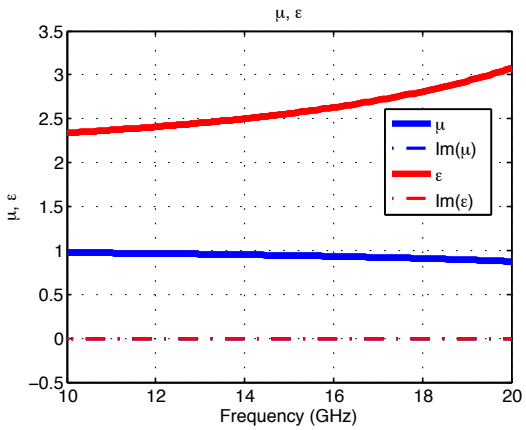

FIGURE 3.10: Parameter retrieval for ELC metamaterial shown in Figure 3.9

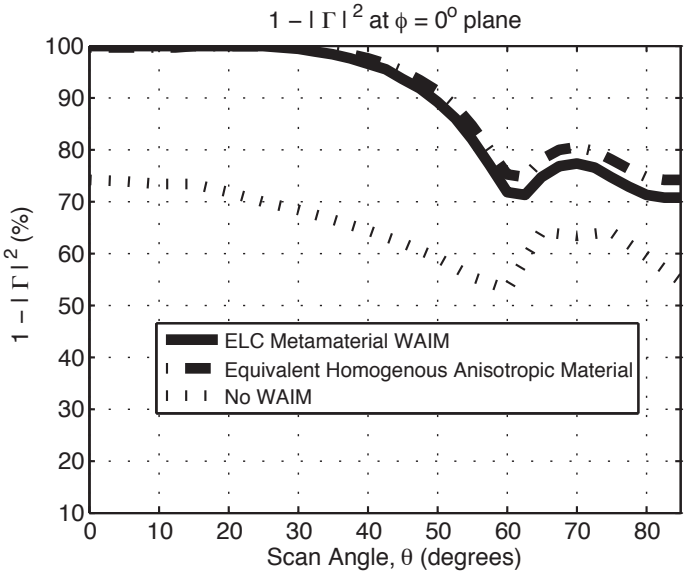

FIGURE 3.11: Comparisons of $1-|\Gamma|^2$ for metamaterial layer vs equivalent homogeneous anisotropic medium material ($\mu_r = 1$, $\epsilon_x = \epsilon_y = 2.58$, $\epsilon_z = 1$, and $d_1 = 2.1mm$) over array with square lattice.

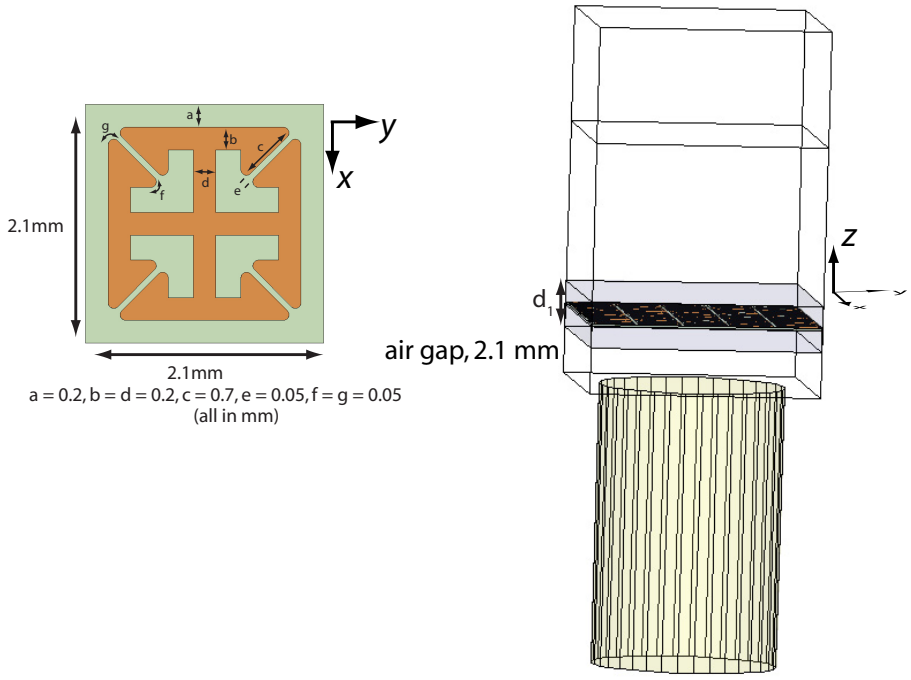

FIGURE 3.12: Phased Array Unit Lattice with ELC-based metamaterial layer (with air gap over array).

simulated and its results are compared to that of an equivalently assigned homogeneous anisotropic material. Figure 3.12 shows the setup and unit cell characteristics of the ELC layer used herein.

A comparison of the HFSS simulation results for the ELC metamaterial layer and the equivalently assigned bulk anisotropic material is shown in Figure 3.14. Note that the ELC array in this example is also made out of PEC and immersed an air substrate.

Figures 3.11 and 3.14 show agreement between the results obtained from the ELC WAIM simulations and the equivalent homogeneous anisotropic simulations. These results suggest that an effective medium model (homogenization of the metamaterial array) sufficiently describes the behavior of a metamaterial layer over the phased array.

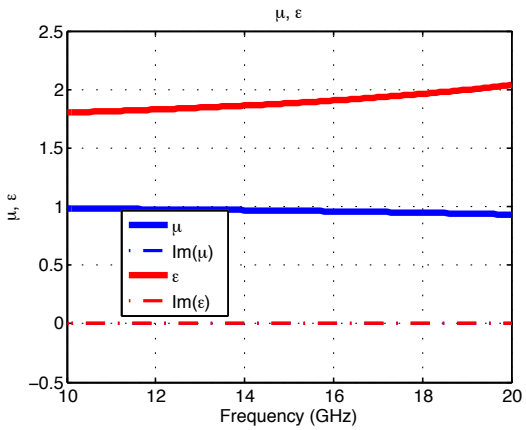

FIGURE 3.13: Parameter retrieval for ELC metamaterial shown in Figure 3.12

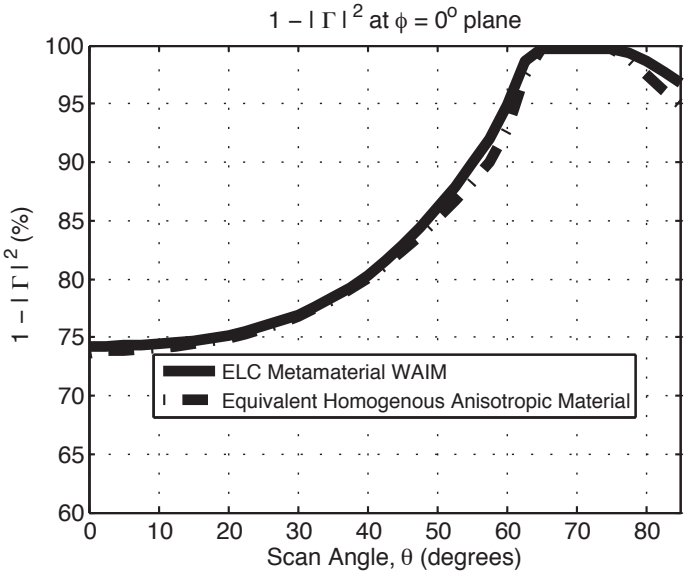

FIGURE 3.14: Comparisons of $1-|\Gamma|^2$ for metamaterial layer vs equivalent homogeneous anisotropic medium material ($\mu_r = 1$, $\epsilon_x = \epsilon_y = 1.9$, $\epsilon_z = 1$, and $d_1 = 2.1mm$) over array with square lattice.

3.5 Bandwidth

Since bandwidth is a critical figure of merit in microwave systems, it is important to consider the implications of metamaterial WAIMs over the entire bandwidth of phased array antennas. Depending on the frequency regime the permittivity or permeabilty of a metamaterial may change rapidly, especially at frequencies close to the metamaterial particle resonance. For the resonant ELC particles shown in Figures 3.9 and 3.12, the resonance frequency is located at 34 GHz and 36 GHz respectively. Due to the large separation of the resonance frequency from the 15.25 GHz antenna operation frequency, we can operate in a less frequency dispersive and less lossy regime of the metamaterial. For instance, in the narrowband application explored (15.25 GHz $\pm$500 MHz), the permittivity $\epsilon_x = \epsilon_y$ varies only from 1.88 to 1.89 for the ELC in Example 1 and from 2.56 to 2.59 for the ELC in Example 2, thus exhibiting minimal dispersion within the bandwidth of the antenna.

When very large or very small constitutive parameter values are needed in a metamaterial, it might be necessary to operate closer to the resonance frequency of the metamaterial, where high losses and strong frequency dispersion will be incurred. Based on these considerations, it is important to optimize the WAIM parameters such that the anisotropic constitutive parameters needed are not very high, not near zero, and not negative.

3.6 Experimental Characterization of Phased Array Antenna with Metamaterial WAIM Layer

Although we have demonstrated the use of simple metamaterial layer(s) to implement anisotropic WAIMs in simulation, we have yet to demonstrate this functionality in experiment. The motivation behind this section is to examine whether the radiation characteristics of a metamaterial-covered phased array antenna can be adequately

described if the metamaterial layer is replaced with its effective medium model. To this end, we present experimental results that show the radiation characteristics of a phased array antenna in the presence of a simple array of Electric-Inductive-Capacitive (ELC) resonators; we then compare the obtained experimental results with results obtained from numerical simulations wherein the ELC resonator metamaterial layer has been replaced with its anisotropic effective medium model. Being able to treat a metamaterial WAIM as an effective medium material would enable the engineer to systematize the design of the matched PA thus making it practical to design desired anisotropic WAIMs using metamaterials.

3.6.1 Full-Wave Simulation of 64-element Array

The use of the multi-modal model method described in detail in Chapter 2 is straightforward for infinite or very large arrays [44], for arrays smaller than 1000 elements however, more complicated analyses need to be done. It would have been considerably easier to perform our experiments on a very large array but due to the high cost of manufacturing these commercial devices (Very large phased array antennas of the kind in Figure 2.2 are known to cost in the hundreds of thousands of dollars), our research group was not able to gain access to one. As an alternative, we were provided access to a 64-element array with the general element topology of Figure 3.15. We adapt this antenna to our objective by using a full-wave simulator to simulate the setup depicted in Figures 3.15a & 3.15b. We utilize CST Microwave Studio for the simulation because finite-difference-time-domain (FDTD) solvers are more amenable to electrically large computational domains than finite-element-method (FEM) solvers. (In the previous sections, we used FEM-based HFSS to solve the infinite array problem by solving one unit lattice with periodic boundaries; here we shall use CST to simulate a sixty-four element planar phased array so that we can appropriately capture the edge effects that come with finite arrays).

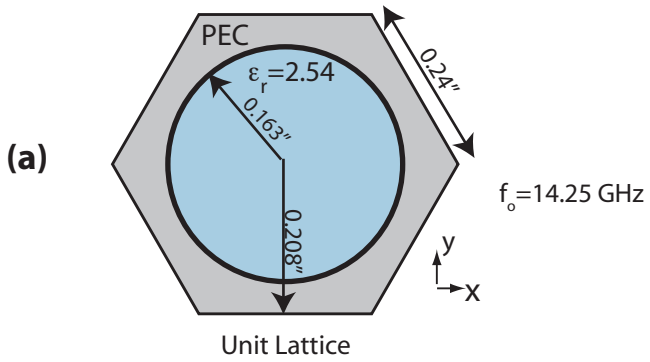

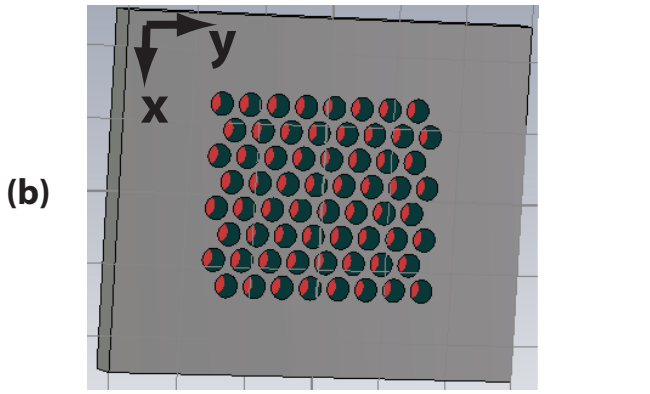

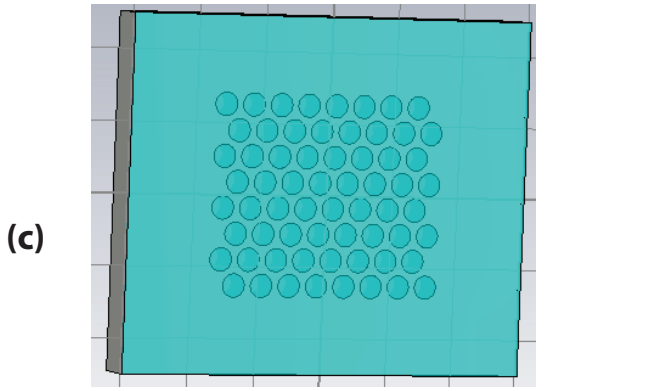

FIGURE 3.15: CST Microwave Studio simulation setup of (a) 64-element phased array (b) 64-element phased array covered with effective medium model of metamaterial WAIM. (c) Top view of unit lattice; center circular waveguide element is loaded with a $\epsilon_r = 2.54$ dielectric plug and is fed with an $\hat{x}$-polarized TE_{11} mode.

The CST model in Figure 3.15 was created by subtracting sixty-four cylindrical regions out of a rectangular conducting block of thickness at least λ_g of the propagating TE_{11} mode. The appropriate steering phasing conditions are ensured by incrementally setting the phase difference to be $\frac{2\pi}{\lambda} d_x \sin\theta\cos\phi$ and $\frac{2\pi}{\lambda} d_y \sin\theta\cos\phi$ between the respective waveguide antenna elements along the $\hat{x}$ and $\hat{y}$ directions respectively; d_x and d_y are the lattice constants in the $\hat{x}$ and $\hat{y}$ directions. Depicted in the unit lattice diagram of Figure 3.15c, $d_x = 2 \times 0.208"$ and $d_y = 2 \times 0.24"$.

The impact of the metamaterial WAIM was investigated by performing two sets of numerical simulations. The first set of simulations determined the power transmission profile of the array over a range of scan angles, in the absence of a WAIM covering (Figure 3.15a). The configuration for the second set of simulations was identical to the first, but included a layer of continuous material with constitutive parameters $\mu_x = \mu_y = 0.9, \mu_z = 1, \epsilon_x = \epsilon_y = 2.3, \epsilon_z = 1, d = 2.1mm$ (Figure 3.15b). This anisotropic material layer represents the homogenized parameters at 14.25 GHz of the metamaterial WAIM of the unit cell structure shown in Figure 3.16.

Depicted in Figure 3.17 is the radiation profile for seventeen scan conditions – from 0° to 85° in five-degree increments – along the $\phi = 90°$ azimuthal plane (the plane that slices down the middle of the array along the $\hat{y}$-direction). Note that due to the relatively low number of waveguide antenna elements, at large scan angles there is a noticeable disparity between the location of the peak of the main lobe and the intended scan angle. For instance, when the scan angle is 10°, the main lobe points at 10°, but when the scan angle is 70° the main lobe is centered at 63°. We also note that data for the power radiated in the presence of the anisotropic WAIM model has been normalized to the power radiated at broadside without any WAIM covering. The same amount of power is fed into the antenna array for all scan angles and configurations, and the received power is plotted as a function of scan angle. Figure 3.17 shows that the introduction of the homogeneous anisotropic

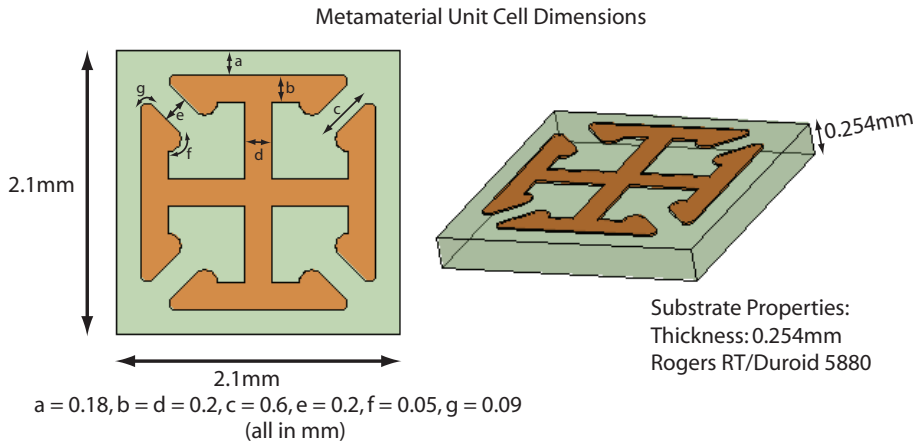

FIGURE 3.16: Metamaterial WAIM unit cell with effective medium properties $\mu_x = \mu_y = 0.9$, $\mu_z = 1$, $\epsilon_x = \epsilon_y = 2.3$, $\epsilon_z = 1$, $d = 2.1mm$ at the 14.25 GHz array operating frequency (a parameter retrieval was performed using the method outlined in [7]). The effective medium homogenization is performed assuming the above metamaterial particle is centered within a $2.1mm$ cubic region of air.

layer enables a higher power transmission the beam is steered away from $\theta = 0°$.

3.6.2 Experimental Measurements

To validate simulation results, we conducted two sets of experiments on a phased array of a similar topology as the simulated model. The first set of measurements were without a WAIM covering, and in the second set of measurements was with metamaterial layer of the particle displayed in Figure 3.16. Figure 3.18 shows a photograph of the fabricated metamaterial WAIM layer (approximately equivalent to the simulated, homogenous, anisotropic material), and the experimental phased array with and without the metamaterial WAIM covering. We note that the 64-element phased array used in the experiment is placed within an electrically large aluminum casing that we do not simulate due to computational limitations owing to its large dimension.

The measurements were done in a compact antenna range, with the array antenna

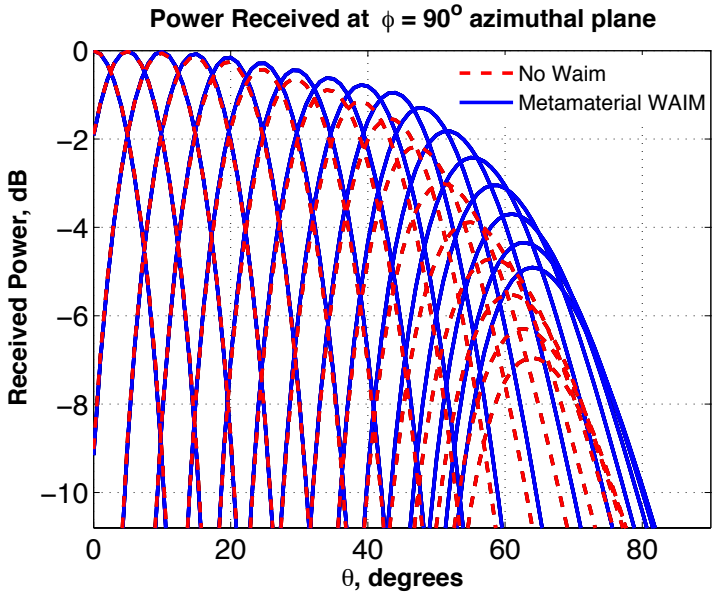

FIGURE 3.17: Numerical simulation results of power transmitted into the far field of 64-element array.

rotated around a stationary $\hat{x}$-polarized horn antenna to receive the radiated power. (All the power radiated in the far-field is contained in the x-polarization of the E-field, because of the strictly $\hat{x}$-polarized feed.) We note that the input power is fixed for all scan conditions and configurations. (The antenna is scanned in increments of 5°, from 0° to 85°) Depicted in Figure 3.19, we observe that the received power is enhanced by the presence of the metamaterial layer over the phased array.

3.6.3 Discussion and Comparison of Full-Wave and Experimental Results

In both Figures 3.17 and 3.19, we observe that the radiation performance is superior when the metamaterial WAIM or its effective medium model is placed over the surface of the phased array. Notwithstanding the differences between the experimental environment and simulation model, these figures show that the metamaterial sheet (of Figure 3.18) is qualitatively consistent with its approximate homogenized model (used in the CST setup of Figure 3.15b) in facilitating improved impedance matching

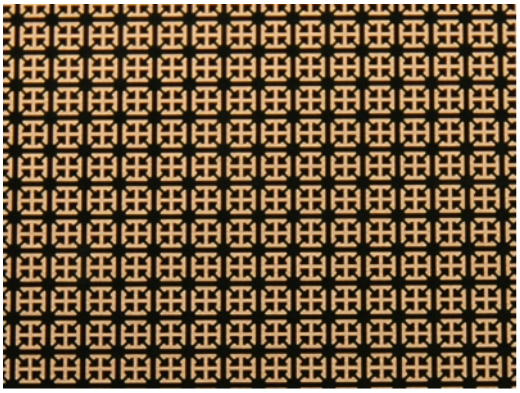

(a)

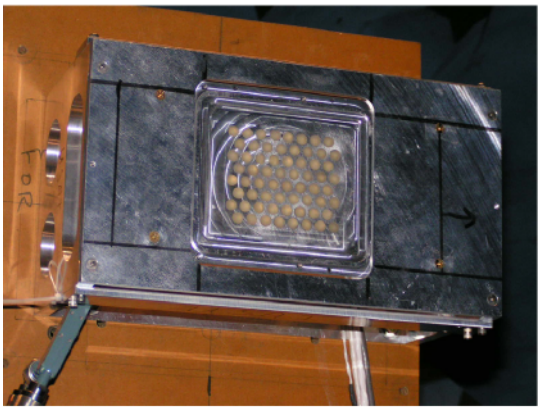

(b)

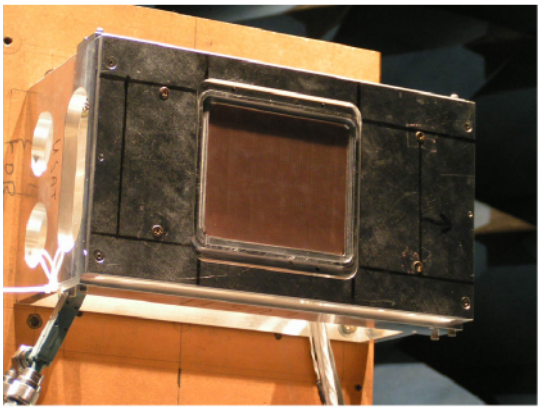

(c)

FIGURE 3.18: (a) Fabricated metamaterial WAIM sheet (b) 64-element array antenna without covering. (c) Same antenna, with metamaterial sheet placed over a $1mm$-thick foam (foam has approximately the same properties as air).

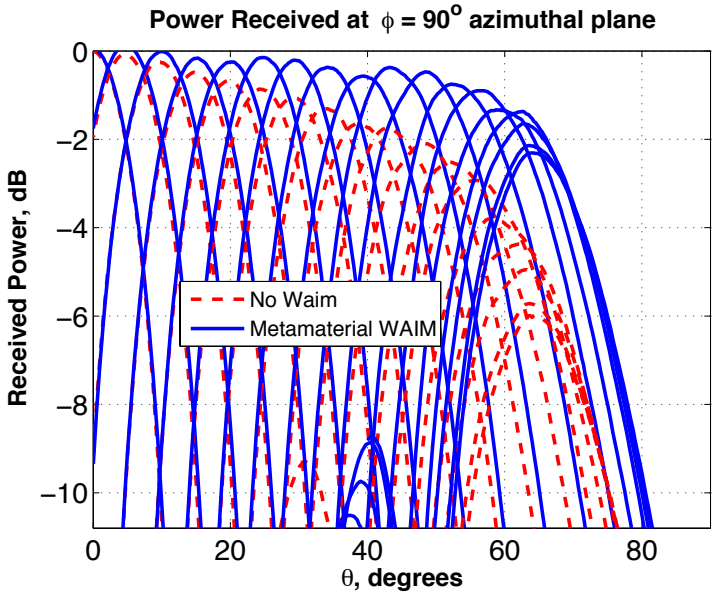

FIGURE 3.19: Experimental measurement results of power received in the far field for seventeen scanning conditions, with and without an ELC metamaterial layer of homogenized parameters: $\mu_x = \mu_y = 0.9$, $\mu_z = 1$, $\epsilon_x = \epsilon_y = 2.3$, $\epsilon_z = 1$, $d = 2.1mm$. (Each distinct concave-down graph represents a unique scanning condition.) The experimental setup is depicted in Figure 3.18.

for the phased array antenna over a broad range of angles.

Figure 3.20 depicts the increase in beam peak power for each scanning condition due to the placement – over the array surface – of the ELC metamaterial sheet (experiment) or its anisotropic model (simulation). The results show that the metamaterial WAIM (experiment) improves the magnitude of the radiated power as a function of scan. The effect was also seen in the full-wave simulation of the effective medium model. This suggests that the effective medium model of the metamaterial, obtained using standard retrieval procedures, provides a qualitative description of the metamaterial WAIM placed over a planar phased array antenna. We attribute the differences between the simulation and experimental results to the larger aluminum casing, and to the possibly reduced accuracy of the homogenized anisotropic model as the scan angle is steered away from broadside; this is not of primary concern

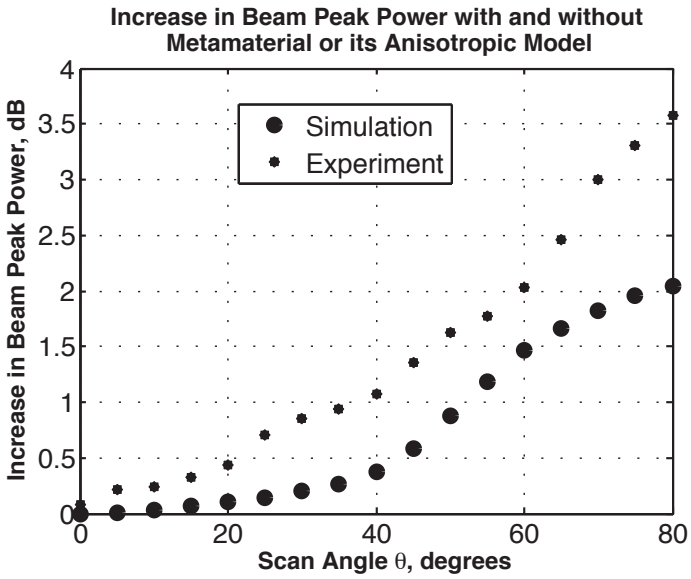

FIGURE 3.20: Increase in beam peak power due to placement of metamaterial WAIM sheet (experiment) or its anisotropic homogenized effective medium model(simulation) over planar phased array surface; horizontal axis represents the intended scan angle of phasing condition.

here however as experimental data corroborates the improved impedance matching simulated.

A further issue to consider is the influence of the metamaterial WAIM on array power measures such as directivity, bandwidth, sidelobe level, and far-field radiation pattern. To ascertain some of these power measures, we provide, in Figure 3.23, a full plot of the far field pattern at $\theta = 45^\circ$ with and without the metamaterial WAIM. A visual inspection of the far-field profile at this scan angle with and without the metamaterial layer reveals a similar directivity, sidelobe level, and overall radiation pattern, thereby suggesting that WAIMs made up of metamaterials may be employed as impedance matching materials without degrading these antenna power measures. The power profile for other scanning conditions are consistent with Figure 3.23.

Finally, we note that the use of metamaterial WAIMs is particularly suitable for inherently narrowband phased array applications because metamaterials are in-

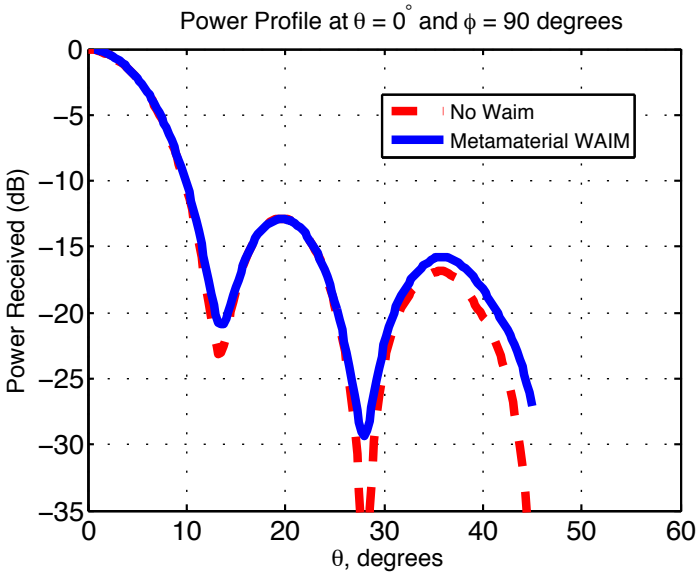

FIGURE 3.21: Experimentally measured far-field beam profile at 0° scan angle, with and without metamaterial Layer

trinsically narrowband when operated near resonance, but can be broadband when operated away from resonance or with broadband structures [**?**].

3.7 Challenges associated with Implementing Single or Bi-Layer Anisotropic WAIM Layer(s) using Metamaterials

With any new technology, there are a set of challenges that need to be completely understood and overcome. For metamaterials, one of these is the use of the effective medium model to constitutively describe metamaterial WAIMs: because homogenized effective medium parameters are obtained by inverting the scattering response of a metamaterial to a normally incident TEM wave, the effective medium parameters may not be accurate anymore when the metamaterial is illuminated obliquely with arbitrarily polarized waves. The reduced accuracy of the effective medium model for off-normal incidence and mixed-polarization waves may result in an inaccurate prediction of power transmission ratio as the scan angle θ is steered from broadside

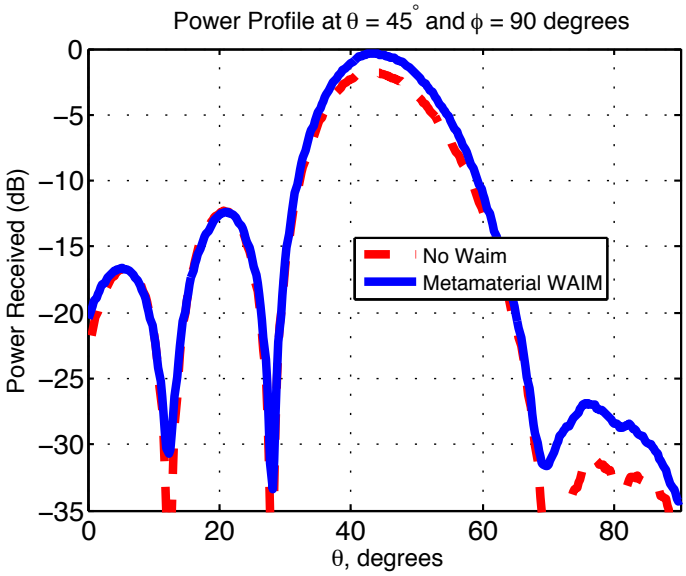

FIGURE 3.22: Experimentally measured far-field beam profile at 45° scan angle, with and without metamaterial Layer

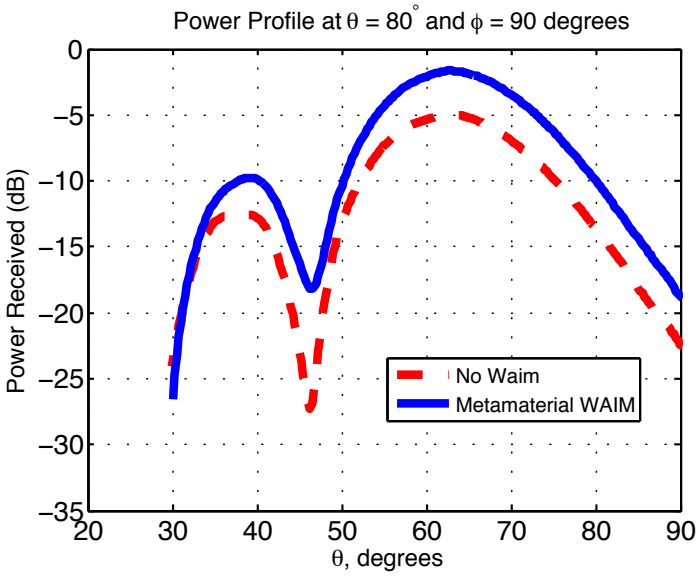

FIGURE 3.23: Experimentally measured far-field beam profile at 80° scan angle, with and without metamaterial Layer

to larger angles. This problem may be remedied by coming up with a paradigm – in place of the effective medium model – that describes metamaterials by accounting for all possible wave interactions. An approach of this nature would also enable the metamaterial to be placed directly over the array surface without having to use an intervening air gap (foam) layer.

When two layers of metamaterial WAIM layers are used to implement a bi-layer of anisotropic materials, each layer needs to be carefully designed because coupling between the metamaterial particles in the top and bottom layers could change such that the product of the transfer matrix of the separate layers would be different from the realized transfer matrix of the layers when stacked together. An approach to effectively describe the combination of both layers is to push the effect of the coupling into one of the layers. This can be implemented by dividing the realized transfer matrix of both layers by the separate transfer matrix of one of the layers; the resulting quotient contains the interlayer coupling and becomes the new transfer matrix of the second layer. From this new transfer matrix, the effective medium parameters of the second layer can be recalculated.

Cross-coupling between adjoining metamaterial layers can be remediated by using intervening dielectric layers to separate the metamaterial layers, or by utilizing metamaterial particles that are less prone to coupling outside of their unit cell. Another approach might be to use a paradigm that accounts for all possible interactions to describe the interaction between metamaterial layers. From a systematic design standpoint, this approach is difficult to implement because it will involve performing electromagnetic field interaction analysis on metamaterial layer combinations for all possible field configurations, thus slowing down the design process.

3.8 Future Work

We have suggested the use of anisotropic layers, implementable using metamaterials, to achieve wide angle impedance matching for phased array antennas. In order to successfully achieve wide angle impedance matching via this method, it is essential to be able to reliably design metamaterial layers with at least four degrees of freedom (uniaxial μ, uniaxial ϵ, variable thickness). For a reliable and predictable design to be achieved, further work will need to be done so as to develop metamaterial structures with minimized loss, cross-coupling and bi-anisotropic effects [56]. Additionally, it is important to utilize metamaterial structures that can be feasibly and realizably fabricated.

3.9 Conclusion

In this chapter, we have shown both computationally and experimentally that anisotropic materials, implementable using metamaterials, can be used as wide angle impedance matching layers for phased array antennas. In order to demonstrate this capability, we developed a MATLAB code to characterize the array performance in the presence of anisotropic layers, and then utilized a Monte-Carlo optimization scheme to prescribe optimal anisotropic material parameters that enable strong transmission from elevation angles from $\theta = 0^\circ$ to 80° for all azimuthal planes.

To implement anisotropic WAIMs from metamaterials, we performed simulations and experiments using a metamaterial layer made up of electric-inductive-capacitive particles which are primarily electrically resonant. Simulation results of both the ELC metamaterial WAIM and its homogenous anisotropic equivalent lead to similar results. Similarly, we were also able to show, using experimental measurements on a 64-element phased array, that the anisotropic description approximately describes the transmission performance of a phased array in the presence of an ELC metamaterial

WAIM. In our experiment, the ELC metamaterial WAIM layer engenders a phased array transmission behavior that is qualitatively similar to the prediction based on an anisotropic description of the metamaterial.

We also discussed some of the future work that would need to be done in order to be able to systematically design, fully understand, and ensure the performance of metamaterial WAIMs over phased arrays. In particular, we examined the role of coupling between higher order waveguide modes and metamaterial particles, and we also discussed cross-coupling between adjoining metamaterial layers in a multi-layer metamaterial stack. We highlighted that these issues can be circumvented by placing a foam layer (or an intervening dielectric layer) between the array surface and metamaterial, and also doing the same to separate adjoining metamaterial layers. A direct way to take cross-coupling and bianisotropic effects into account would be through a paradigm that takes into account all possible wave interactions with the metamaterial layer. The effective medium method, which has been shown in the literature to be accurate for homogeneous plane wave configurations, estimates the constitutive parameters of a metamaterial by inverting its scattering response to normally incident plane waves; the accuracy of this method reduces when off-normal waves with different polarizations are introduced onto the metamaterial.

Although the aforementioned factors need to be taken into account during the metamaterial WAIM implementation process, this work contributes to the foundational work needed to characterize arrays matched with anisotropic materials, and presents numerical data that validates the prospects of using metamaterials to achieve anisotropic WAIMs. We showed that it is possible to use a single anisotropic layer to implement a WAIM that is comprehensively matched (see Figure 3.7).

In summary, we have shown, using a simple metamaterial layer, that it is feasible to use metamaterials as anisotropic WAIMs in phased array applications without jeopardizing other array performance metrics. Since metamaterials provide the flex-

ibility to engineer constitutive parameters in several directions, their use in phased array applications may prove useful in obtaining impedance matched array antennas.

4

Design and Numerical Analysis of Metamaterial Composite for Radome Applications

In the previous chapters we discussed the use of metamaterials as wide-angle impedance matching layers on planar phased array antennas. In this chapter, we shall analyze the use of metamaterial inclusions to create materials that may be used as radome materials. An electromagnetic radome is a covering to protect an antenna from potentially detrimental elements such as wind perturbations, aerodynamic drag, and so forth. Radome are typically made from dielectric materials. In order to not disrupt radiated fields from and to the enclosed antenna, a radome, ideally, should be made from a fully transparent and non-refractive material. Radomes and other structures that enclose radiating systems are designed for their mechanical integrity, and they are typically made from ceramics or composites that have inherently high dielectric values. Due to differences in curvature between the inner and outer surfaces of radomes, refraction in radome materials introduces deflections to exiting local plane waves. Boresight error [40] [41] is a quantitative measure of such deflections. As illustrated in Figure 4.1, boresight error can be expressed as,

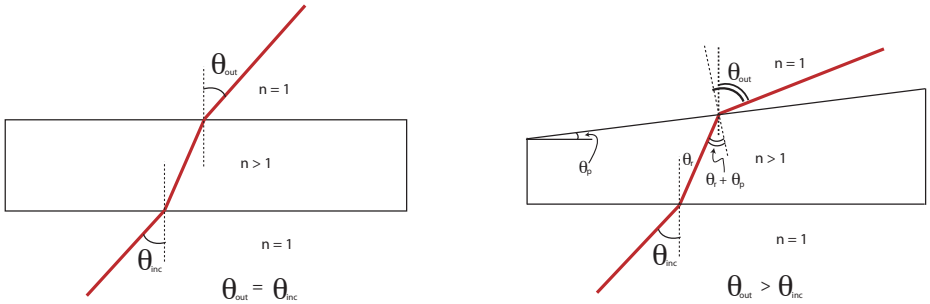

FIGURE 4.1: Illustration of bore sight error. (a) Refraction in rectangular slab, exiting angle equals incident angle because entry and exit surfaces are parallel (b) Refraction in prism, exit angle not equal incident angle because entry surface is not parallel to exit surface

$$\theta_{\mathrm{BSE}} = \theta_{\mathrm{out}} - \theta_{\mathrm{inc}} \tag{4.1}$$

A radome is non-refractive when its index is matched to air (n_{radome}=n_{air}) and is fully transparent when impedance-matched to air (Z_{radome}=Z_{air}). To exhibit both characteristics, the radome material would need to be impedance-matched and index-matched to free space for all angles of TE and TM-polarized local plane wave incidence. From an electromagnetic standpoint, the solution to this problem is trivial: make the radome out of air. Since such a solution precludes the presence of an actual radome, a more practical solution is necessary.

Previously, we discussed the use of a planar electric inductive-capacitive (ELC) resonator to artificially engineer permittivity. The ELC creates an anisotropic electric excitation as a strong electric response is only excited in the direction perpendicular the capacitive gap. The goal of is this chapter is to discuss the creation of a radome material that exhibits the electromagnetic properties of air in all directions. Our strategy is to create such a composite material by embedding an isotropic electric resonator particle into a host dielectric such that the presence of the isotropic electric resonator depresses the refractive index of the composite to unity at a frequency

of interest. A metamaterial with the electromagnetic properties of air would be maximally transmissive and minimally refractive. For this purpose we design a three-dimensionally resonant ELC particle which we refer to as the 3D-ELC. This chapter examines with the design and numerical analysis of the 3D-ELC resonator composite, and Chapter 5 presents an experimental analysis of the fabricated metamaterial composite.

The 3D-ELC repeated unit cell consists of two ELC elements that when put together may be used to generate responding electric dipole moments in the $\hat{x}$, $\hat{y}$, and $\hat{z}$ directions. When embedded inside a host material whose permittivity is significantly greater than unity, the repeated 3D-ELC metamaterial can be used to depress the effective dielectric constant of the resulting composite material to a near-unity value in all Cartesian directions. The concept of designing a unity-index metamaterial – with the properties of free space – may prove useful in creating mechanically durable materials for use as radomes or other enclosures for radiating structures.

4.1 Introduction

Electromagnetic metamaterials have attracted significant research interest because they can be used to form structures with electromagnetic or optical properties not readily available in conventional materials. Metamaterials are composed of a collection of sub-wavelength inclusions, whose composite electromagnetic properties may be accurately described by continuous, bulk constitutive parameters, such as the electric permittivity or magnetic permeability [15] [14].

Over the past several years many applications of metamaterials have been proposed [24] [57]. What these applications have in common is the need to engineer independent constitutive responses of the metamaterial in multiple Cartesian directions. A metamaterial whose constitutive response can be easily adjusted in all three Cartesian directions would provide additional control as well as further expand the

range of applications in which the metamaterials can be useful. Both isotropic metamaterials, as well as metamaterials with controlled anisotropy are of interest, since both can usefully manage the polarization and other properties of electromagnetic waves. Likewise, metamaterials in which the constitutive properties are controlled spatially [30] have found enormous potential application when coupled with the emergent design technique of transformation optics [31].

The concept of creating a metamaterial element excitable in multiple directions has been explored for certain structures [58] [59]. The ideal goal here is the design of an isotropic electric metamaterial composite, whose constitutive parameters are equivalent to those of free space over some range of frequencies. The particular design herein is based on the combination of multiple electric-LC resonators, or ELCs, which provide an adjustable electric response in all directions. The ELC, introduced by Schurig et al. [8], is a metamaterial element that exhibits a resonant electric dipolar response to applied electromagnetic fields. Although the resonant nature of the ELC implies bandwidth limitations ultimately on the constitutive properties of the composite, there should be nevertheless a small range of frequencies where the overall index and impedance (normalized to Z_{air}) of the dielectric host plus ELC inclusions can be made equal to unity. This design has practical implications, since radomes and other structures that enclose radiating systems are designed for their mechanical integrity, and typically make use of ceramics or composites that have inherently high dielectric values [40]. For such radome applications, a tradeoff usually has to be made between the mechanical properties and the electromagnetic properties. By contrast, the use of 3D-ELC inclusions to modify the electromagnetic properties of an enclosure can reduce the aberrations or other detrimental scattering associated with the radome, and may even be useful for adding specified electromagnetic functionality to the overall system.

To illustrate the utility of the 3D-ELC, we consider a composite metamaterial

formed by embedding the 3D-ELCs into a dielectric host material whose dielectric constant is significantly greater than unity. By engineering the parameters of the 3D-ELC, we seek to find a frequency range over which the composite is strongly transmissive and weakly refractive over a wide range of incident angles and polarizations. Conceptually, the 3D-ELC inclusions depress the effective permittivity from that of the host material to close to ϵ_r=1 in the $\hat{x}$, $\hat{y}$ and $\hat{z}$ directions. Comparison materials that possess similar electromagnetic properties are foams or aerogels, which are not useful as structural components. While in some cases it is possible to design the thickness of a radome to make use of constructive interference to achieve good transmission, the large dielectric value still causes refraction at the interfaces and can still introduce aberrations and distortion into the communications channel. Nevertheless, we provide comparisons of the simulated performance of the 3D-ELC composite with the simulated performance of a dielectric optimized for Fabry-Perot resonance to show that similar transmission performance can be achieved in the two structures for both polarizations and a broad range of incident angles.

4.2 3D Implementation of ELC

4.2.1 ELC Overview

The ELC is an electrically coupled resonator composed of a capacitive region flanked by a pair of symmetric inductive loops. The constitutive response of the ELC is purely electric, since the currents flowing in the inductive loops have opposite sense and the induced magnetic fields in each section are opposed. Figure 4.2a depicts the described ELC structure, while Figure 4.2b shows a variant that has two gaps on the exterior of the ELC. The dual gap ELC design typically couples more strongly to the applied electric field. Though a magnetic resonance is allowed in this structure (there is a capacitive/inductive path around the circumference of the ELC), the magnetic resonance occurs at a higher frequency and contributes little response near the lower

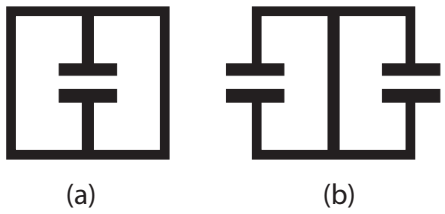

FIGURE 4.2: (a) ELC proposed by Schurig [8] and (b) Electrically similar configuration. The outer loops of both structures carry currents in opposite directions thus harboring no net magnetic moment.

electric resonance. The 3D-ELC, discussed in the next subsection, is inspired by the ELC structure of Figure 4.2b .

4.2.2 3D-ELC

Although there is wide flexibility in designing a 3D version of the ELC, we have in mind the production of a relatively thin sheet of composite material that is ultimately compatible with commercial fabrication. A particular convenient fabrication approach based on multilayer circuit board techniques was introduced by Starr et al. [60], who demonstrated a negative index composite based on in-plane lithographically patterned wires with out-of-plane split ring resonators (SRRs) utilizing vias. Though we present only simulation results here, the design of our ELC is strongly motivated by the potential for realization by these commercially available circuit board methods.

The three-dimensional implementation of the 3D-ELC in Figure 4.3a is made up of two structures: a planar isotropic ELC structure and a larger four-legged 3D structure whose center wire is connected to four symmetrical loops, each with a capacitive gap breaking the loop.

The vertical four-legged structure in Figure 4.3b is a superposition of two orthogonal ELCs that both have four-fold rotational symmetry in the x-y plane. This

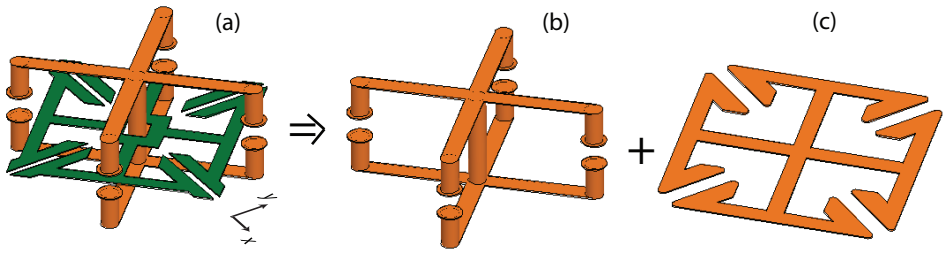

FIGURE 4.3: Three-dimensional ELC and its constituent particles. (a) Three dimensionalized ELC, excitable by an electric field polarized in any and all directions (b) Vertical 4-legged inclusion, primarily excitable by E_z. (c) Planar inclusion (similar to structure in [9]), excitable by E_x, E_y, or a combination of both.

symmetry implies the response of the element will be the same when illuminated by waves traveling from $\hat{x}$ or $\hat{y}$. The fundamental mode of this structure couples strongly to an E-field along $\hat{z}$, but negligibly to a magnetic field piercing the loops.

The planar ELC structure in Figure 4.3c is a two-dimensionalized version of the planar ELC in Figure 4.2b such that an electric excitation is possible in two directions, as opposed to just one. Also possessing 90° symmetry, the fundamental mode of the two-dimensionalized planar ELC particle couples strongly to electric fields with in-plane components ($\hat{x}$ or $\hat{y}$ directions). Qualitatively, a wave polarized with E-field components strictly in the $\hat{x}$ or $\hat{y}$ direction would equally primarily excite only two capacitive gaps, thus inducing current directions shown in Figure 4.4a. Another illustrative scenario is if the particle were excited with a wave whose E-field is polarized equally in the $\hat{x}$ and $\hat{y}$ directions (i.e. $\vec{E} = \hat{x}\frac{1}{\sqrt{2}}E_\circ + \hat{y}\frac{1}{\sqrt{2}}E_\circ$). An E-field orientation of this nature would excite all four gaps on opposite sides of the structure (see Figure 4.4b). These two scenarios demonstrate that the structure may be excited by an electric field polarized with $\hat{x}$ or $\hat{y}$ components or a combination. For the most part, the strength of the electric dipole moment generated in the direction of E-field polarization for both Figures 4.4a and 4.4b would be similar. For E-field configurations where ϕ is between 0° and 45° (or equivalently between 45° and 90°), the total

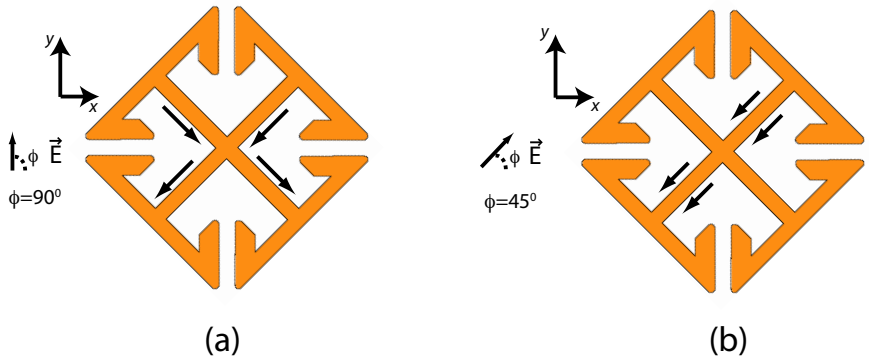

FIGURE 4.4: Depiction of first-order approximation of current flow within planar inclusion given (a) $\vec{E} = \hat{y}E_\circ$ (b) $\vec{E} = \hat{x}\frac{1}{\sqrt{2}}E_\circ + \hat{y}\frac{1}{\sqrt{2}}E_\circ$. Direction of current flow is an indication of direction of electric dipole moment.

electric dipole moment generated in the direction of E-polarization due to all four capacitive gaps may vary slightly, thus we may term the planar two-dimensionalized ELC structure of Figure 4.4 to be approximately isotropic. The particle may be made anisotropic, making the dimensions of any two diagonal capacitive gap pairs in the ELC dissimilar from those of the remaining two capacitive gaps.

In order to utilize a combination of the out-of-plane and in-plane ELCs to obtain a desired isotropic response, we first adjust the geometrical parameters of each inclusion individually (in the absence of the other) to achieve the desired permittivity, and subsequently perform additional refinements in the presence of the other inclusion. The incorporation of both inclusions into the same unit cell slightly alters the response curve of either inclusion, due to their mutual coupling. By performing this analysis and optimizing, we thereafter arrive at an optimized metamaterial design that we refer to as the 3D-ELC. A combination of the planar and four-legged structures (which together make up the 3D-ELC) ensures an electric response in the $\hat{x}$, $\hat{y}$, and $\hat{z}$ directions, thereby enabling a consistent electric response at several polarizations and angles of incidence. In Figure 4.5 is shown a depiction of a 3D-ELC

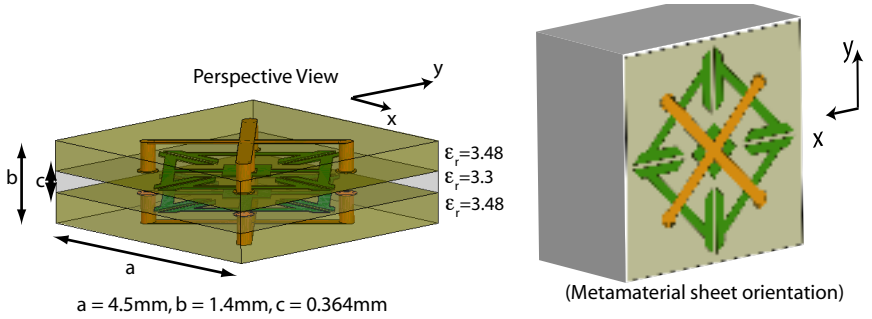

FIGURE 4.5: Constituent unit cell of simulated 3D-ELC. The particle is embedded into a host material of $\epsilon_r = 3.48$.

particle embedded into a material stack that consists two $\epsilon_r = 3.48$ dielectric layers and one middle $\epsilon_r = 3.3$ dielectric layer. The dielectric values and thicknesses are selected to match commercially available circuit board materials. The dimensions of the embedded 3D-ELC are also consistent with commercial fabrication capabilities, and result in an effective dielectric permittivity of close to unity along the three Cartesian directions.

As a means of numerically characterizing the 3D-ELC metamaterial, a metamaterial layer composed of an array of the Figure 4.5 unit cells was numerically simulated for its transmission and reflection properties over a range of incident angles and TE_z/TM_z polarizations. We first present the results obtained for normal incidence; Figure 4.6 shows the reflection and transmission plots and the parameter retrieval plots over the 9-12 GHz frequency range of interest. At normal incidence, the wave that propagates along the $\hat{z}$ direction is polarized TE_z. Around 10.6 GHz, ϵ_r and μ_r are both close to unity (n and Z matched to air), and a pass band is observed in the S_{21} of Figure 4.6 at the same frequency.

It should be noted that a TM_z-polarized wave propagating along the plane of incidence would predominantly excite an electric response in the planar inclusion while a wave of oblique incidence will excite both the planar and four-legged vertical

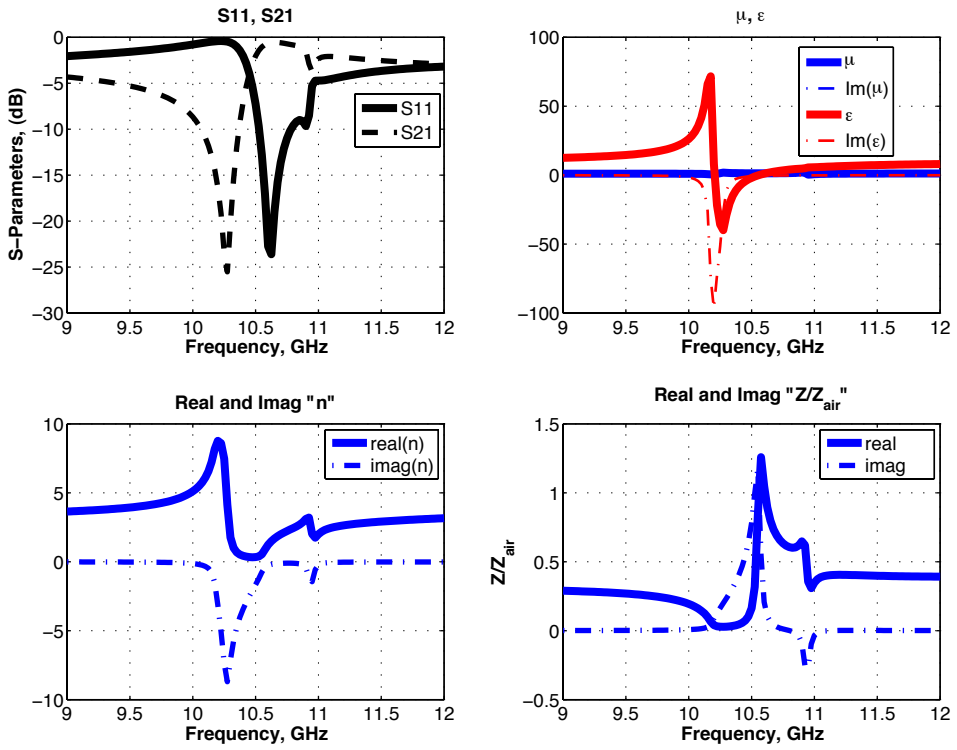

FIGURE 4.6: Parameter retrieval characteristics of the designed 3D-ELC metamaterial at normal Incidence.

inclusion due to the presence of $\hat{x}$ and $\hat{z}$ components in the oblique plane wave. A TE_z polarized wave propagating along the same plane of incidence would primarily excite an effective electric response in the $\hat{z}$ direction within the planar inclusion. The geometrical parameters of the 3D-ELC inclusion shown in Figure 4.5 were adjusted so that the response of the 3D-ELC metamaterial is uniform in all directions regardless of angle of incidence when impinged on by a wave propagating along the $\hat{x}$-$\hat{z}$ plane.

4.3 Numerical Simulations

4.3.1 Oblique Incidence Simulations of embedded 3D-ELC

Using a technique similar to the *waveguide simulator* approach, the 3D-ELC metamaterial sheet is analyzed by placing a number of its unit cells into a PEC-PMC

waveguide wherein multiple TE_{m0} or TM_{m0} waveguide modes are simultaneously excited [61]. Because the field distribution of these waveguide modes is similar in form to a superposition of two plane waves propagating in the $-\hat{x}$ and $+\hat{x}$ direction (see Figure 4.7), the reflection and transmission properties for a set of angles and frequencies can be obtained by performing simulations on several PEC-PMC waveguide widths, where each variation of the waveguide width is an integer multiple of the 3D-ELC metamaterial unit cells. For each excited TE_{m0} mode, the field at the ports of the PEC-PMC waveguide takes the form:

$$\vec{E} = 2\hat{y}\cos(k_x x)e^{-jk_z z} \tag{4.2}$$

$$\vec{H} = \frac{2}{\omega\mu}[-\hat{x}k_z\cos(k_x x) + \hat{z}jk_x x\sin(k_x x)]e^{-jk_z z} \tag{4.3}$$

The $\cos(k_x x)$ term decomposed to $e^{-jk_x x} + e^{jk_x x}$ represents two superimposed propagating plane waves, where k_x for a width a of the PEC-PMC waveguide corresponds to Equation 4.4 which shows the relationship between the waveguide width, mode order, and angle of incidence of the superimposed plane waves.

$$k_x = \frac{m\pi}{a} = \frac{\omega\sin\theta}{c} \tag{4.4}$$

More details on the oblique incidence simulation method used can be found in [61].

Because the 3D-ELCs are resonant, the metamaterial sheet is inherently narrowband. The geometrical parameters of the 3D-ELC metamaterial are engineered such that the effective permittivity of the metamaterial medium is depressed from around $\epsilon_r = 3.4$ (the host dielectric) to $\epsilon_r = 1$ at the 10.7 GHz frequency of interest. For the parameters chosen, the 3D-ELCs have a resonance frequency at 10.3 GHz, so that we expect the region where the composite is matched to occur at slightly

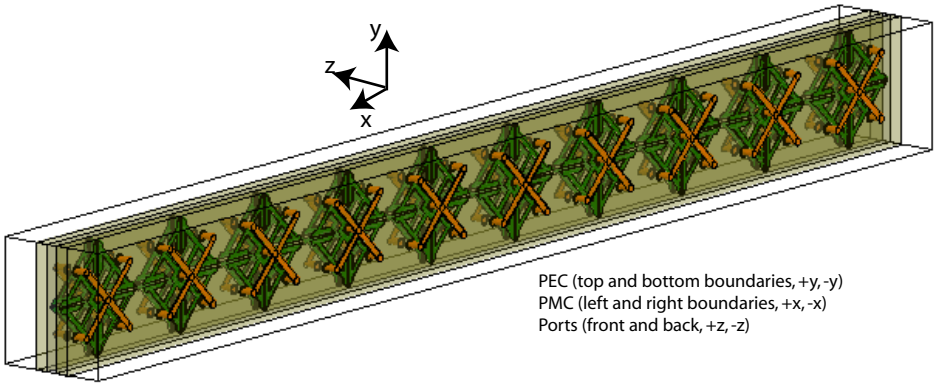

FIGURE 4.7: Representative PEC-PMC waveguide configuration for oblique incidence plane wave simulation. Setup shows ten 3D ELC unit cells, similar simulations are performed for 11, 14, 17, 18, 19, 20, 21 and 22 3D ELC cells, and six higher order TE_{m0} modes are excited for TE plane wave simulation. For TM simulations, the PEC and PMC boundary assignments are interchanged, and TM_{m0} modes are excited instead.

higher frequencies. Indeed, observation of the transmission and reflection properties between 9-12 GHz reveals a pass band at 10.7 GHz where we expect the structure to be matched.

To obtain a sufficient amount of angular data from 9-12 GHz for TE polarization, we perform simulations (using Ansoft HFSS^{TM}) of several PEC-PMC waveguides with widths corresponding to 10, 11, 14, 17, 18, 19, 20, 21 and 22 3D-ELC cells. Six higher order TE_{m0} waveguide modes are excited for each waveguide simulation. Figure 4.7 shows a configuration of the unit cells within a simulated PEC-PMC waveguide, the depicted configuration containing ten unit cells. A similar set of simulations are performed in order to obtain numerical data for TM-polarized incidence, in which case the assignment of the PEC and PMC boundaries would interchanged so that TM_{m0} modes are excited instead. The obtained S_{11} and S_{21} of the discussed higher order waveguide mode simulations were organized and interpolated to produce the transmission and reflection plots shown in Figure 4.8.

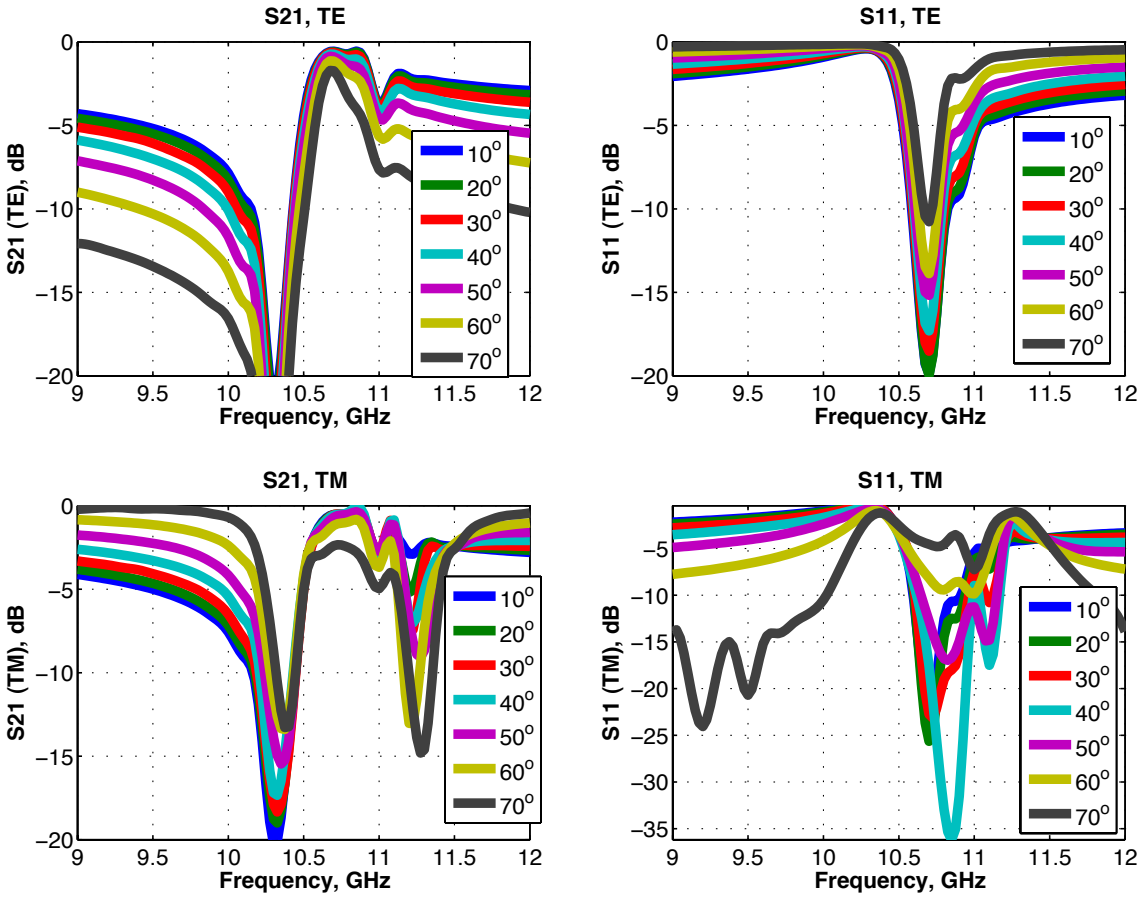

FIGURE 4.8: Simulated S_{11} and S_{21} for TE_z and TM_z incidence on material made up of the 3D-ELC unit cell configuration shown in Figure 4.5.

4.3.2 Comparison of 3D-ELC Metamaterial with Dielectric Optimized for Fabry-Perot Resonance at 10.7 GHz

The reflection and transmission performance of the 3D-ELC metamaterial whose unit element is shown in Figure 4.5 was compared with the performance of an optimized $\epsilon_r = 3.4$, $d = 7.6mm$ dielectric designed to be strongly transmissive at its 10.7 GHz Fabry-Perot resonance. A $\epsilon_r = 3.4$ material is selected because of its dielectric similarity to the 3D-ELC metamaterial host dielectrics. Radome materials are typically designed to have a thickness that enable a Fabry-Perot resonance at a frequency of

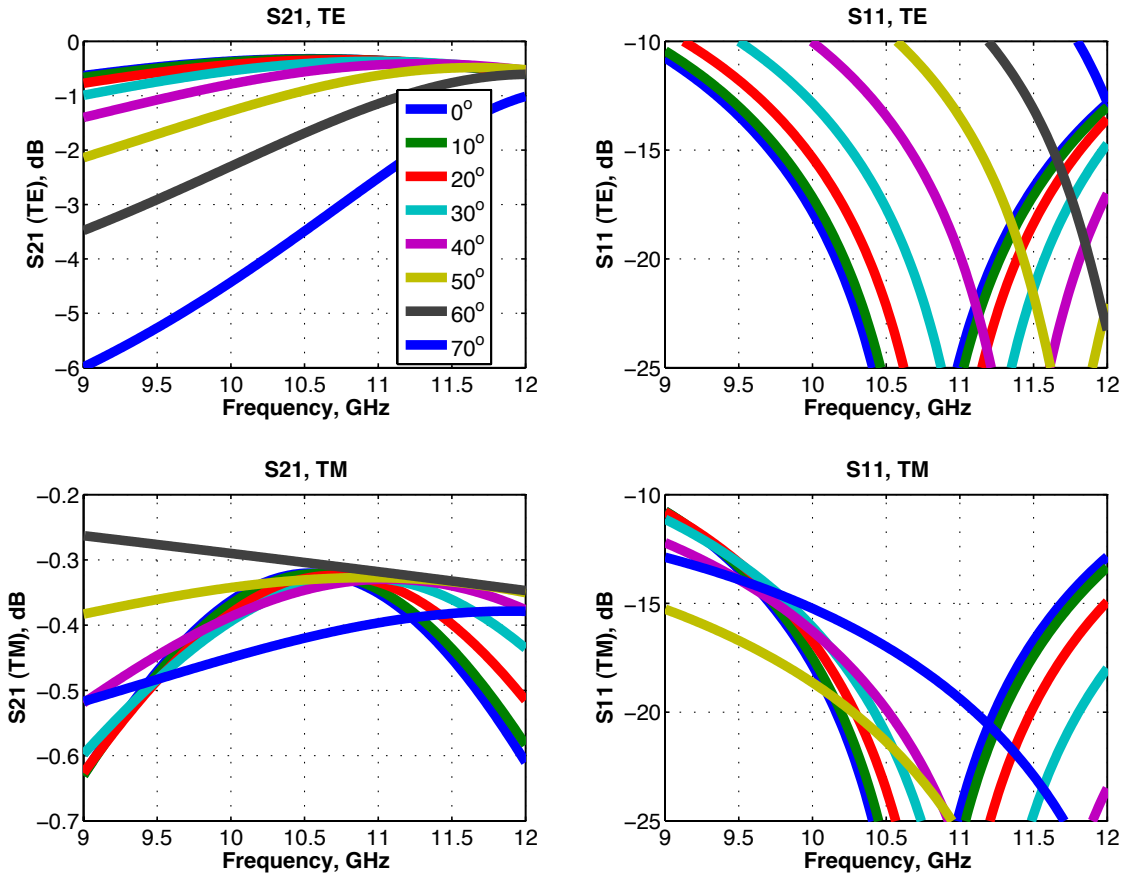

FIGURE 4.9: Oblique incidence S_{11} and S_{21} performance of a $\epsilon_r = 3.4$ ($\tan\delta = 0.02$) material designed to be strongly transmissive at its 10.7 GHz Fabry-Perot resonance.

interest and incident angle (transmission performance may degrade at other angles of incidence). The performance of the aforementioned Fabry-Perot dielectric material – our idealized (non-metamaterial) radome material – is shown in Figure 4.9.

The design of the 3D-ELC metamaterial enables strong transmissive and index-matching features that are for the most part retained as a function of angle of illumination, irrespective of the polarization. This provides the advantage of reducing boresight error, a refractive error that occurs due to the conformal and index-mismatched nature of radomes. Boresight error is a measure of the beam deflection that occurs

when the interface at which an electromagnetic beam enters a material is not parallel to the plane of the interface at which the same beam exits the material. The simplest illustration of boresight error is the deflection introduced to local plane waves exiting a triangular prism after having been illuminated with normally incident plane waves at an opposite boundary interface not parallel to the interface of the exiting plane waves.

Table 4.1: S_{11} and S_{21} at 10.7 GHz, TE Polarization

	FABRY-PEROT		3D-ELC	
Angle	S_{11} (dB)	S_{21} (dB)	S_{11} (dB)	S_{21} (dB)
0°	-34.1	-0.32	-24.0	-0.57
10°	-33.2	-0.32	-19.9	-0.56
20°	-27.5	-0.34	-20.0	-0.59
30°	-20.9	-0.38	-18.5	-0.64
40°	-15.4	-0.49	-17.3	-0.73
50°	-10.9	-0.78	-15.2	-0.89
60°	-7.0	-1.48	-13.9	-1.15
70°	-3.6	-3.10	-10.8	-1.73

Table 4.2: S_{11} and S_{21} at 10.7 GHz, TM Polarization

	FABRY-PEROT		3D-ELC	
Angle	S_{11} (dB)	S_{21} (dB)	S_{11} (dB)	S_{21} (dB)
0°	-34.1	-0.32	-24.0	-0.57
10°	-35.6	-0.32	-22.9	-0.54
20°	-28.9	-0.32	-25.6	-0.52
30°	-24.2	-0.33	-22.8	-0.53
40°	-21.9	-0.34	-17.6	-0.56
50°	-22.8	-0.33	-12.8	-0.68
60°	-36.3	-0.31	-8.2	-1.18
70°	-17.9	-0.41	-4.6	-2.39

Tables 4.1 and 4.2 show at 10.7 GHz a tabulation of the transmission and reflection off of the 3D-ELC metamaterial (Figure 4.8) and the Fabry-Perot dielectric (Figure 4.9). At 10.7 GHz, the table shows similarities between the transmission and reflection performance of the metamaterial and the Fabry-Perot dielectric. For both

polarizations, the S_{11} for the 3D-ELC metamaterial is less than -10 dB at the angles shown except at 60° TM and 70° TM. The Fabry-Perot dielectric shows less than -10 dB for all TE angles as well except for 60° TE and 70° TE. The case is similar for S_{21} as both materials have similar transmissive properties overall.

These results suggest that embedded inclusions inside a host dielectric may be used to create strong transmission over a range of angles and polarizations by engineering its permittivity and index to be near-unity along the main cartesian directions. As shown for the 3D-ELC metamaterial in Tables I and II, this approach provides transmissive properties comparable to counterpart radome materials, and introduces the added advantage of reducing refraction-induced boresight errors.

4.4 Conclusion

In this chapter we have explored the general concept of utilizing embedded three-dimensionalized ELC metamaterial inclusions to obtain materials with strongly transmissive but weakly refractive properties. In the design of, for instance, radome materials where mechanical viability is often emphasized at the expense of electromagnetic viability, the use of embedded inclusions to modify electromagnetic imperfections may prove useful in improving performance without jeopardizing mechanical viability. The content of this chapter has been primarily based on numerical simulations and analysis. The next chapter investigates experimentally the transmission, reflection, and refractive index characteristics of the metamaterial composite discussed in this chapter.

5

Experimental Characterization of Metamaterial Composite for Radome Applications

In Chapter 4, we analyzed the design of a three-dimensionalized electric resonator particle termed a three-dimensionalized electric inductive-capacitive (3D-ELC) resonator. In this chapter we present angle-resolved transmission and reflection experimental measurements of a composite material composed of 3D-ELC metamaterial particles embedded inside a host dielectric.

By embedding electrically resonant metamaterial particles inside a host dielectric, the permittivity of the composite material (inclusions + host dielectric) can be adjusted to desired values of interest. As discussed in the previous chapter, the isotropic electric resonance of the three-dimensionalized electric inductive-capacitive (3D-ELC) metamaterial particle is used to depress the permittivity of the metamaterial composite to a value less than the host dielectric, but close to air. The modification of the permittivity of the composite material may enable the realization of a material that is – at a certain frequency or small range of frequencies – both index-matched and impedance-matched to free space in all directions.

Radomes are made from a limited range of dielectric materials because mechanical viability is the chief desired feature. Typically, the thickness of the radome dielectric is adjusted so that it is perfectly impedance-matched (Fabry-Perot resonance) at a certain angle of incidence and acceptably matched at other angles. Index matching is thus traded off for impedance matching thereby resulting in a highly transmissive radome with boresight error features.

Later in this chapter, it will be shown that transmission and reflection measurements on the fabricated 3D-ELC metamaterial composite of Chapter 4 show that at a certain frequency the composite responds identically to TM and TE-polarized as well as to obliquely incident waves. These results, coupled with a parameter retrieval on normal incidence measurements, suggests that the refractive index of the metamaterial composite is depressed in all directions thereby enabling reduced refractive errors and strong transmission.

5.1 Introduction

Research in the field of metamaterials has led to several proposed applications in which electromagnetic properties not achievable with conventional materials are obtained. Metamaterials provide the ability to artificially control permittivity and permeability in ways previously impossible, thereby loosening the restrictions on the electromagnetic properties that can be realized. For example, structured materials have been designed with a wide range of permittivity and permeability values [19] [13], with anisotropic properties [62] [52] [58], and compelling devices such as the invisibility cloak have been designed and implemented [24] [5].

We proposed [10] that by embedding metamaterial inclusions into conventional materials, it is possible to depress the index of the composite to lower values while maintaining a low reflection coefficient. In this work, we present experimental results on a metamaterial composite composed of embedded three-dimensionalized electric-

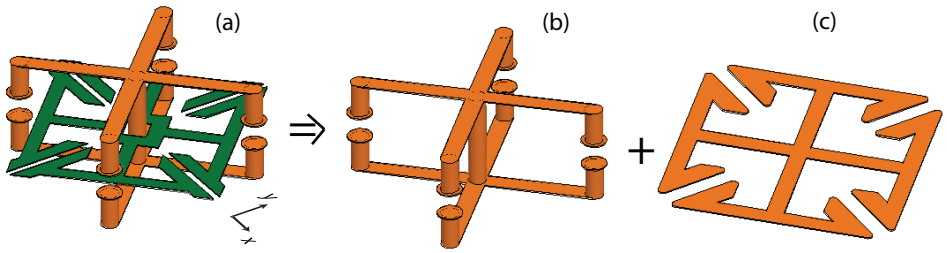

FIGURE 5.1: (a) Unit cell of three-dimensionalized ELC; can excite strong electric dipole moment in $\hat{x}$, $\hat{y}$, and/or $\hat{z}$ directions. (b) Outer 4-legged inclusion; excites strong electric dipole moment in $\hat{z}$ direction. (c) Planar inclusion; excites strong electric dipole moment in $\hat{x}$ and/or $\hat{y}$ direction(s). From [10]

inductive capacitive (3D-ELC) structures designed to excite an electric resonance in the $\hat{x}$, $\hat{y}$, and $\hat{z}$ directions for both TM and TE polarizations. The excitation of an electric response in all directions may enable the use of this particle to depress or adjust the refractive index of the composite to a more desirable value.

5.2 Embedded 3D-ELC Metamaterial Composite

Previously, the concept of reducing bore sight error by utilizing embedded three-dimensionalized ELC [8] inclusions to depress the permittivity of a composite material was introduced. Using this approach, the strong electric response of the 3D-ELC structure of Figure 5.1a was used to adjust the permittivity of the composite in all three directions, thereby reducing refraction and maintaining a strong transmission coefficient at a certain frequency for TE or TM-polarized waves incident at a wide range of angles.

Side by side in Figure 5.2 is the simulated unit cell and close-up view of the fabricated sheet of the metamaterial composite. The sample was fabricated using the multilayer approach proposed by Starr et al. [60]. The metamaterial composite was designed to be resonant within the X-band, and was made by embedding 3D-ELC inclusions into a dielectric composite consisting of Rogers RO4450-dx and RO4350$^{\text{TM}}$

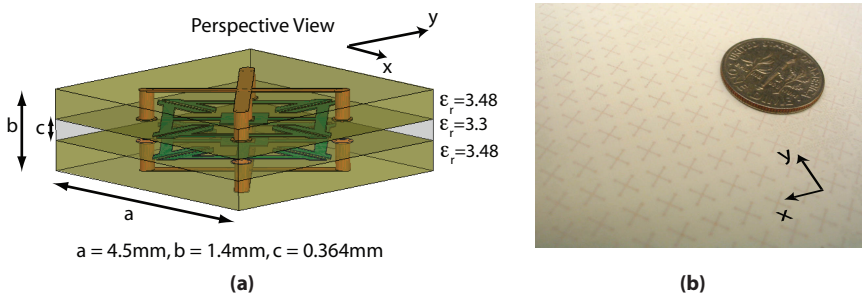

FIGURE 5.2: (a) Simulative model of 3D-ELC unit cell embedded into a dielectric composite. (b) Fabricated 3D-ELC metamaterial composite sheet

material; this multilayer stackup simplifies the manufacturing of the metamaterial composite. The fabricated board was 1.4mm thick and measured 6×9 in^2 in external dimensions. Each embedded metamaterial unit cell occupies a 4.5×4.5×1.4 mm^3 volume.

5.3 Experiment

We performed transmission (S_{21}) and specular reflection (S_{11}) measurements on the sample using the experimental setup of Figure 5.3. Transmission measurements were taken for TE and TM-polarized incidence from 0° to 60° and reflection measurements were taken from 25° to 60°. The effective permittivity and permeability (in the direction of polarization) of the metamaterial composite can be directly calculated from normal incidence measurements [7]. It is much more complicated to perform meaningful parameter retrievals for transmission and reflection measurements at off-angles, therefore, to estimate the isotropic characteristic of the 3D-ELC, we compare the off-angle transmission and reflection measurements to the normal-incidence transmission and reflection measurements. Since the aim of using the 3D-ELC is to excite an electric resonance in all directions, we expect the transmission and re-

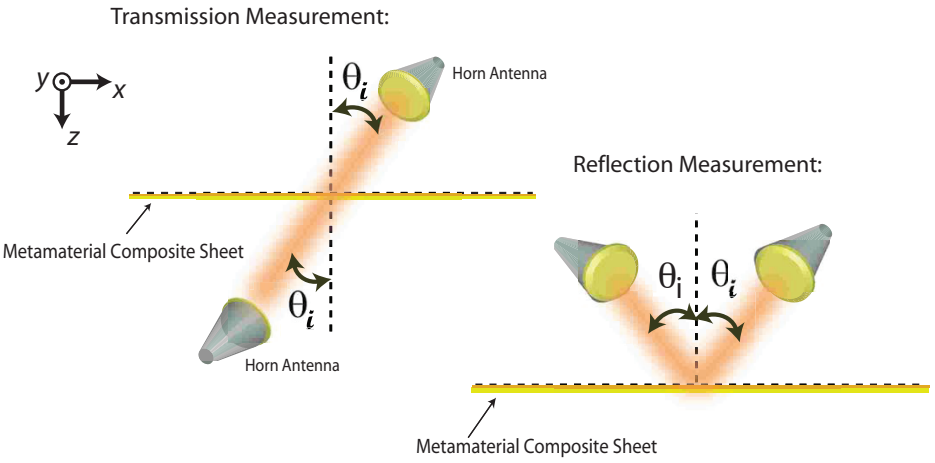

FIGURE 5.3: Experimental setup of oblique incidence transmission and specular reflection measurements. For TE-polarized incidence, the electric field is strictly $\hat{y}$-polarized for all angles of incidence, while for TM-polarized incidence, the magnetic field is strictly $\hat{y}$-polarized. (From [11])

flection measurements at off-angles to possess an equally strong resonance at the same frequency. An equally strong resonance at the same frequency implies that the electric response may be employed to depress the permittivity to local plane waves incident from oblique angles as well as from the normal. The off-angle transmission and reflection results are discussed in detail in Section 5.4.

As shown in the experimental setup depicted in Figure 5.3, two dielectric lens horn antennas each positioned a focal length from the sample were used to take transmission and reflection measurements. For transmission measurements, the antennas were placed within the same line of sight, and the sample was placed halfway between the beam path. For reflection measurements, the both horns were placed at specular angles away from the board. The lens horn antennas, each with a 2.5-inch wide FWHM focal spot one foot away from the horn aperture, were connected to an Agilent N5230A network analyzer, and were mounted on rotatable rails which

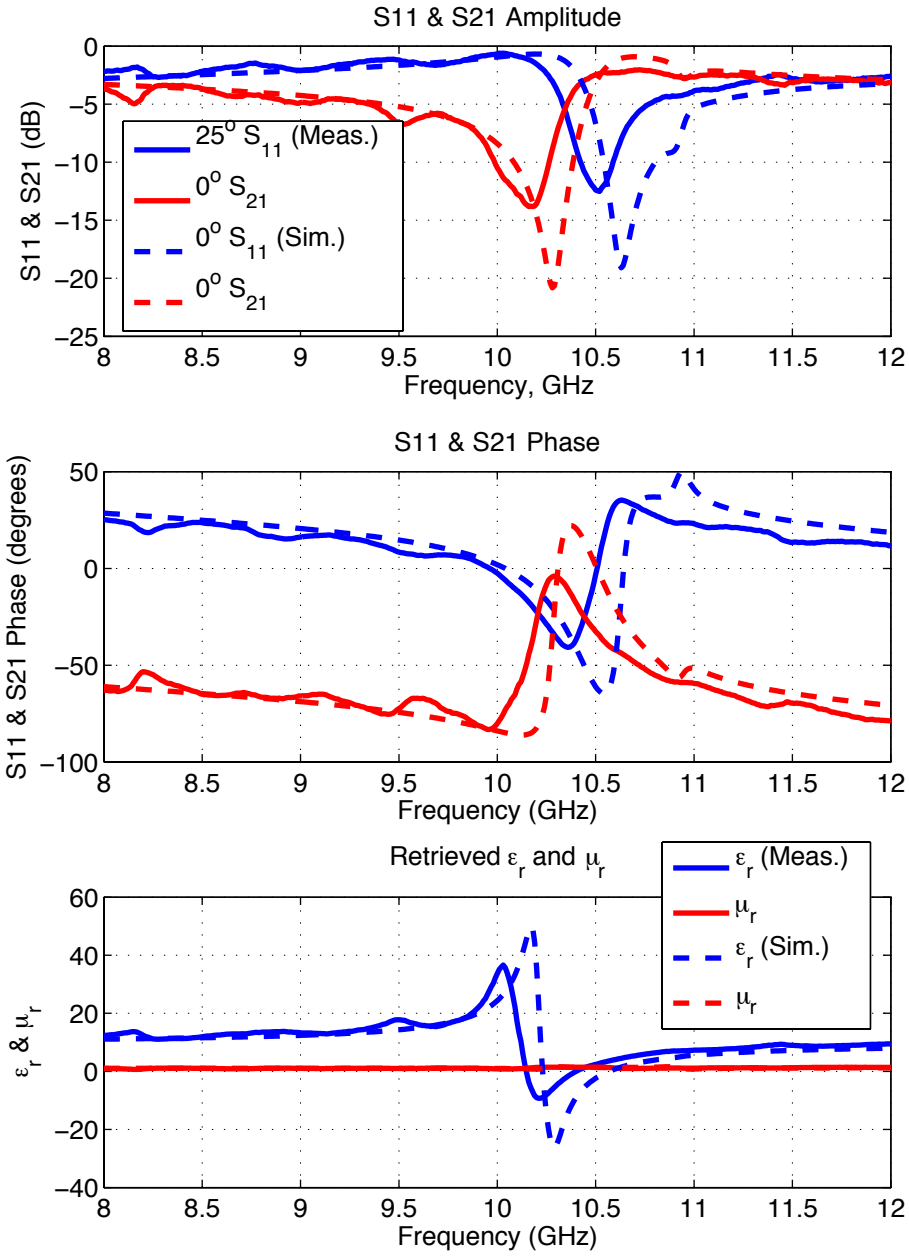

FIGURE 5.4: Measured data compared with data obtained from numerical simulations at normal incidence. The comparisons are done for a normal incidence ($\theta = 0$) configuration (see Figure 5.3). *(top)* S-parameter amplitude *(middle)* S_{11} and S_{21} phase *(bottom)* Constitutive parameter retrieval.

allowed for a rotation of the antennas around the fixed sample. For every rotation of the horns, the network analyzer was calibrated to remove any decalibration that may have been introduced to the system. The frequency range of interest was between 8-12GHz.

In order to be able to perform parameter retrievals we found it important to acquire very accurate phase information from measurements. We found that reflection measurements are more prone to phase errors. Reflection measurements were taken after calibrating the reflection setup with an aluminum sheet of roughly the same dimensions as the metamaterial composite sheet. The aluminum sheet is then replaced with the sample. In order to obtain accurate phase information, it was important for the location of the surface of the calibrating aluminum sheet be the same as the location of the surface of the introduced metamaterial sample. At 10GHz, for instance, a 2mm shift in the location of the metamaterial sample surface introduces a 48° phase error into the reflection measurements. (A 2mm shift in the surface location introduces a 4mm roundtrip path length to the measured results, which impresses an errorneous $\pm\frac{2mm}{\lambda_{10GHz}}\cdot 360^\circ$ phase onto S_{11}.) Such a large error significantly reduces the accuracy of the parameter retrieval. In addition, to correct for the 180° phase introduced by the aluminum calibration sheet, we multiply the obtained reflection results by e^{j180°. A sturdy frame was designed to hold the sample such that the plane of the surface of metamaterial composite would be at the appropriate location during each reflection and transmission measurement.

For transmission measurements at each incidence angle, the transmission setup was first calibrated without the sample in the path of the horn antennas. This calibration scheme normalizes out the path loss and path length between the horn antennas from the transmission data. Furthermore, because the transmission measurement ought to be referenced to the front and back surface of the sample, we multiply the transmission results by $e^{jk_\circ d}$ to remove the phase due to the region

of free space occupied by the sample. The sample thickness is d. For both reflection and transmission measurements, we were able to reduce the VSWR between the measurement horns by covering the surface of the both horn lens with foam dampers.

5.4 Results and Discussion

In Figure 5.4 we present transmission and reflection measurements taken at normal incidence, and compare these with simulation results. (Due to limitations in our apparatus we can only take reflection measurements from 25° to 60°, but not at normal incidence; the normal incidence reflection simulation results in Figure 5.4 are directly compared with 25° incidence angle measurements.) The displayed simulation results, as discussed in the previous paper [10], were simulated using Ansoft HFSS$^{\text{TM}}$ by simulating the 3D-ELC of Figure 5.2 in a PEC-PMC waveguide in which only normally incident plane waves can propagate.

A comparison of measured and simulated transmission and reflection data shows very close agreement. We observe that there is a frequency shift in the measured results, and we owe this to the tolerance of the fabrication process. We also notice that the fabricated sample has a weaker resonance in the S_{11} and S_{21} plots, and in the retrieved ϵ and μ plots; this indicates that there more losses in the fabricated sample than was accounted for in simulation. The frequency at which both ϵ and μ intersect is the frequency (outside of resonance) at which there is an index match. If at the intersection frequency both ϵ and μ are unity, then the material is simultaneously index-matched and impedance matched. For simulation data, the index match occurs at 10.61GHz, at which $\epsilon = \mu = 1.35$. From experimental data an index match of $\epsilon = \mu = 1.43$ occurs at 10.45GHz. We must note that the experimental values are probably lower since we substituted reflection measurements at 25° in place of normal incidence reflection measurements. In the absence of 3D-ELC metamaterial inclusions, the refractive index of the material of Figure 5.1a is $\sqrt{3.48} = 1.87$ whereas

with metamaterial inclusions it is between 1.35 and 1.43. The lower index results in a material with reduced refraction. Though the original motivation behind the metamaterial composite was to design a $\epsilon = \mu = 1$ composite, our results at normal incidence demonstrates that the refractive index and permittivity can be depressed with the use of inclusions. The measured reflection coefficient of the metamaterial composite at the index-match frequency (from Figure 5.4) is a low reflection coefficient of -12.4 dB. This experimentally demonstrates that low reflection and refraction can be attained with the use of metamaterial inclusions.

The off-angle measurements shown in Figure 5.5 were taken in order to demonstrate that the 3D-ELC particle excites a similar electric resonance at oblique angles of incidence. The consistence of these measurements with normal incidence measurements indicates how much the performance of the material changes at off-angles. The measured data shows a consistently strong electric resonance for both TE and TM polarized incident waves and at all angles of incidence. At resonance, the reflection coefficient is consistently below -10dB for TE and TM polarizations and at all angles of incidence, except at $\theta = 60^\circ$ for TE polarization. A low reflection coefficient at the resonance frequency indicates a very strong electric resonance. These results suggests that the electric field vector continues to excite a strong electric response in the metamaterial composite even at other polarizations and at off-angles. (Regular ELCs do not excite a response for TM-polarized waves [11]). A strong electric resonance at off-angles suggests that the metamaterial composite has an effective constitutive response that varies similar to the normal incidence constitutive response. As exemplified in the normal incidence experimental data, this implies that the metamaterial composite may be used to depress the effective index of refraction for TE and TM-polarized waves at oblique angles of local plane wave incidence.

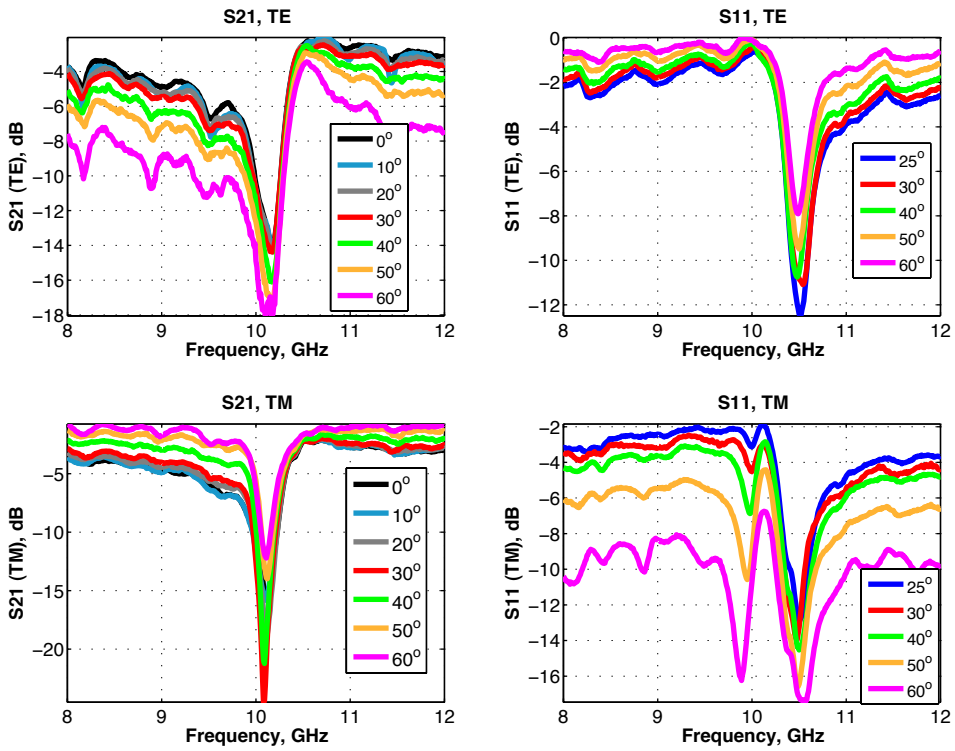

FIGURE 5.5: Experimental data of specular reflection and transmission of composite metamaterial sheet for various angles and TE and TM polarizations.

5.5 Conclusion

In this chapter we have demonstrated the use of metamaterial inclusions to adjust the refractive index of a host composite in all cartesian directions. We posit that this capability will prove useful in applications such as the electromagnetic radome. We have shown that metamaterial inclusions may be used to depress the permittivity of the composite (inclusions + host material) to a lower magnitude, and we have presented that this response can be sustained over a range of angles and polarizations. With additional optimization and refinements, this capability can be used to obtain materials which are simultaneously index-matched and impedance-matched to free space at all angles, or to obtain materials that meet a desired set of requirements

over a range of angles and polarizations.

6

Summary and Future Work

6.1 Metamaterials Wide-Angle Impedance Matching Layers

6.1.1 Summary

In this dissertation, we showed that anisotropic materials enable maximum impedance matching for planar phased array antennas over a broad range of scan angles. We also presented data showing that the performance of a planar phased array with a simple metamaterial covering may be modeled using an anisotropic description.

6.1.2 Future Work

We have suggested the use of anisotropic layers, implementable using metamaterials, to achieve wide angle impedance matching for phased array antennas. In order to successfully achieve wide angle impedance matching via this method, it would be essential to be able to reliably design metamaterial particles with four degrees of constitutive freedom ($\mu_x = \mu_y$, $\epsilon_x = \epsilon_y$, μ_z and ϵ_z). For a reliable and predictable design to be achieved, further work will need to be done to develop metamaterial structures with minimized loss, cross-coupling and bi-anisotropic effects. Additionally, it would be important to utilize metamaterial structures that can be fabricated.

6.2 Metamaterial Radome

6.2.1 Summary

In this work, we introduced a strategy through which the permittivity and refractive index of a mechanically viable dielectric radome material may be adjusted. We presented data showing that by embedding three-dimensionalized electric inductive-capacitive resonators – electrically excitable in all directions – into a host dielectric, the permittivity (or refractive) of the composite material (dielectric + inclusions) may be depressed to TE and TM-polarized waves of various incident angles, thus reducing refraction-induced beam deflection and maintaining high transmissive properties.

6.2.2 Future Work

For the proposed strategy to be implemented in actual radomes, future work will need to be done to characterize the boresight characteristics of a conical shell or spherical shell prototype composed of embedded metamaterial inclusions. The role of bandwidth in maintaining the desirable properties of the metamaterial radome will also need to be quantified, depending on the operating characteristics of the enclosed antenna.

Appendix A

Multimodal Derivation of Active Element Admittance

In this appendix, the active element admittance of a waveguide aperture planar phased array is derived using the multi-modal approach discussed in the literature. Presented by Borgiotti [49], this derivation enforces the electric and magnetic boundary conditions at the surface of the array plane, and thus incorporates both the contribution of higher order waveguide modes in the waveguide and higher order evanescent free space modes just above the array surface. It is assumed from the waveguide geometry and operating frequency that all modes but the fundamental mode are cutoff.

A.1 Analytical formulation of the Problem

We begin by assuming that the surface of the array (see Fig. A.1 for depiction of unit cell) resides on the $z = 0$ plane. The lattice is represented by the lattice vectors $\mathbf{s}_1$ and $\mathbf{s}_2$, and the reciprocal lattice as $\mathbf{t}_1$ and $\mathbf{t}_2$. Further, the scan direction θ and ϕ of the array is represented in the reciprocal space by the vector $\mathbf{u}_\circ$, the position

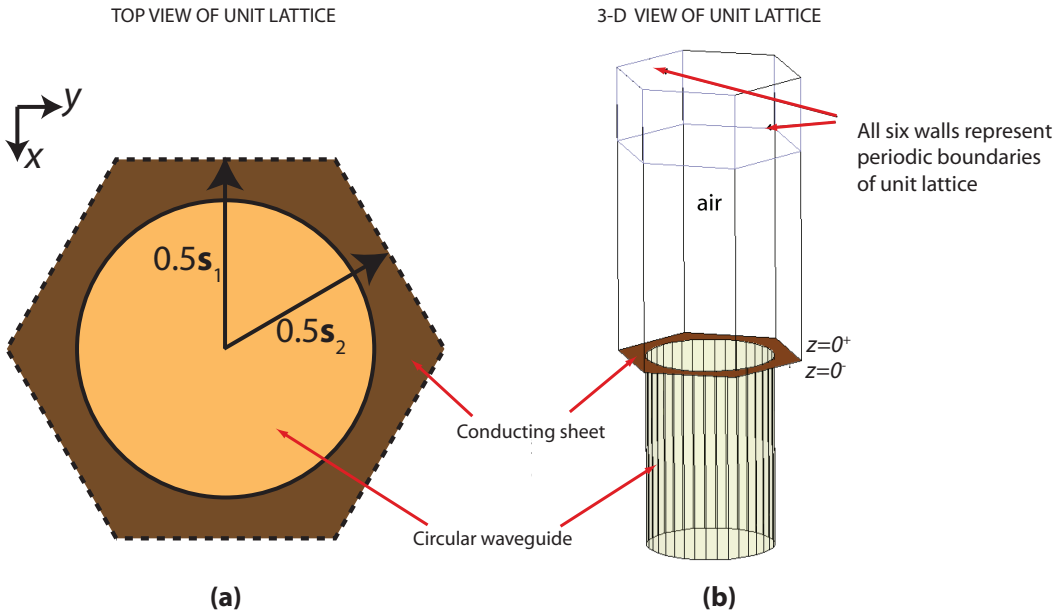

FIGURE A.1: (a) Top view of phased array unit cell, with lattice position vectors $\mathbf{s}_1$ and $\mathbf{s}_2$ (b) 3D rendering of phased array unit cell; plane of waveguide opening is the $z = 0$ plane.

vector along the x,y plane as $\mathbf{x}$, and the index of waveguide elements by the scalars p and q such that the reference voltage across the center element of the array is $\mathbf{V}_{00}$. Additionally, we shall define the surface area of the hexagonal lattice surface as A, and the circular aperture surface area as C.

The aforementioned can be comprehensively expressed as

$$\mathbf{t}_1 = 2\pi \frac{\mathbf{s}_2 \times \mathbf{s}_3}{\mathbf{s}_1 \cdot \mathbf{s}_2 \times \mathbf{s}_3} \qquad \mathbf{t}_2 = 2\pi \frac{\mathbf{s}_3 \times \mathbf{s}_1}{\mathbf{s}_1 \cdot \mathbf{s}_2 \times \mathbf{s}_3} \tag{A.1}$$

$$V_{pq} = V_0 e^{\mathbf{u}_\circ \cdot (p\mathbf{s}_1 + q\mathbf{s}_2)} \tag{A.2}$$

$$\mathbf{x} = \hat{x}x + \hat{y}y \tag{A.3}$$

$$\mathbf{u}_\circ = \hat{x}\frac{2\pi}{\lambda_0}\sin\theta\cos\phi + \hat{y}\frac{2\pi}{\lambda_0}\sin\theta\sin\phi \tag{A.4}$$

We also define a new term to represent the lattice of grating lobes formed on the

array surface, just above the aperture. This term is related to the phasing vector and will be referred to as the *lattice of grating lobes*, $\mathbf{u}_{\circ pq}$.

$$\mathbf{u}_{\circ pq} = \mathbf{u}_{\circ} + p\mathbf{t}_1 + q\mathbf{t}_2 \tag{A.5}$$

We can express the tangential fields at the array surface in two ways: (i) as consisting of a summation of the field distribution of an infinitum of waveguide modes, and (ii) as consisting of a summation of the field distribution of free space modes excited at the aperture. We will express these summation symbolically and equate them in order to enforce the tangential electric and magnetic field boundary conditions at the array surface (i.e. the $z = 0$ plane).

Using a bidimensional Floquet expansion (2D counterpart of Bloch's theorem), the tangential waveguide electric fields at $z = 0^+$ can be represented as an excited spectrum of spatial harmonics weighted by vector coefficients $\mathbf{A}(\mathbf{u}_{\circ pq})$:

$$\mathbf{E}_t(\mathbf{x}) = \sum_{p=-\infty}^{+\infty} \sum_{q=-\infty}^{+\infty} \mathbf{A}(\mathbf{u}_{\circ pq}) e^{-j\mathbf{u}_{\circ pq}\cdot\mathbf{x}} \tag{A.6}$$

Representing the field distribution of waveguide mode i as $\mathbf{e}_i$, the tangential electric fields excited at $z = 0^-$ can be written as a sum of an infinitum of waveguide field distributions weighted by mode amplitudes V_i:

$$\mathbf{E}_t(\mathbf{x}) = \sum_{i=0}^{\infty} V_i \mathbf{e}_i(\mathbf{x}) \tag{A.7}$$

The indices of waveguide modes start from $i = 0$ (the fundamental lone propagating waveguide mode), through $i = 1$ (the first higher order mode), to $i = \infty$ (the higher order mode at infinity). To enforce the boundary condition on the tangential electric fields at the array surface, the expression (A.6) for $z = 0^+$ must equal (A.7) for $z = 0^-$. For a unit waveguide element, this takes the form:

$$\mathbf{E}_t(\mathbf{x}) = \sum_{i=0}^{\infty} V_i \mathbf{e}_i(\mathbf{x}) = \sum_{p=-\infty}^{+\infty} \sum_{q=-\infty}^{+\infty} \mathbf{A}(\mathbf{u}_{\circ pq}) e^{-j\mathbf{u}_{\circ pq}\cdot\mathbf{x}} \tag{A.8}$$

As shown in (A.9), the same can be done for the tangential magnetic fields. For the sake of notational brevity, we refer to the active element admittance as Y_{in} instead of $\mathrm{Y}_{in}(\theta, \phi)$.

$$\hat{z} \times \left[Y_{\mathrm{in}} V_0 \mathbf{e}_{\circ}(\mathbf{x}) - \sum_{i=1}^{\infty} Y_i V_i \mathbf{e}_i \right] = \sum_{p=-\infty}^{+\infty} \sum_{q=-\infty}^{+\infty} \mathbf{B}(\mathbf{u}_{\circ pq}) e^{-j\mathbf{u}_{\circ pq}\cdot\mathbf{x}} \tag{A.9}$$

The right hand side of (A.9) is an analog to (A.6) but with the E-field spatial harmonic vector coefficients $\mathbf{A}(\mathbf{u}_{\circ pq})$ replaced with magnetic field spatial harmonic vector coefficients $\mathbf{B}(\mathbf{u}_{\circ pq})$, and the left hand side is written as such because it expresses the magnetic field based on an admittance paradigm (e.g. for a wave with $\mathbf{E} = \hat{x}E_x$ propagating normally in the $\hat{z}$ direction, $\mathrm{H}_y = \hat{z} \times \mathrm{E}_x$). The purpose of the expression of (A.9) is to find Y_{in} since clearly $Y_{\mathrm{in}} \neq Y_0$. The reader may ask, why isn't the tangential magnetic field expressed as $\hat{z} \times [\sum_{i=0}^{\infty} Y_i V_i \mathbf{e}_i(\mathbf{x})]$? The magnetic field due to the fundamental mode is $Y_{\mathrm{in}} V_0 \mathbf{e}_{\circ}(\mathbf{x})$ and not $Y_{\circ} V_0 \mathbf{e}_{\circ}(\mathbf{x})$ because the fundamental mode faces the radiation admittance Y_{in}.

We would like to solve for (A.10) but we cannot because of the infinite nature of the sums therefore we truncate the i at N and p and q as well.

$$\sum_{i=0}^{\infty} V_i \mathbf{e}_i(\mathbf{x}) - \sum_{p=-\infty}^{+\infty} \sum_{q=-\infty}^{+\infty} \mathbf{A}(\mathbf{u}_{\circ pq}) e^{-j\mathbf{u}_{\circ pq}\cdot\mathbf{x}} = 0 \tag{A.10}$$

Using reaction theorem we relate in (A.11) and (A.13) the truncated sum of waveguide basis functions with the truncated sum of spatial harmonics basis functions.

That is,

$$\iint_C \left[\sum_{i=0}^{N-1} V_i \mathbf{e}_i(\mathbf{x}) - \sum_{\mathbf{u}_{\circ pq}} \mathbf{A}(\mathbf{u}_{\circ pq}) e^{-j\mathbf{u}_{\circ pq}\cdot\mathbf{x}} \right] \times \hat{z} \cdot \hat{q} e^{\mathbf{u}_{\circ mn}\cdot\mathbf{x}} d\mathbf{x} = 0 \tag{A.11}$$

where

$$\sum_{\mathbf{u}_{\circ pq}} \quad \text{is written to represent} \sum_{p=-p_{\max}}^{+p_{\max}} \sum_{q=-q_{\max}}^{+q_{\max}} \tag{A.12}$$

Note that the integral is taken over the unit lattice surface area A but since the tangential electric field over the conducting part of the unit cell lattice is zero, the relevant area of integration is the aperture area, C. In addition, $\hat{q}$ is a unit vector with arbitrary direction on the $x-y$ plane.

The expression of (A.11) can be understood using reaction theorem. From reaction theorem, $\iint_S (\mathbf{E}_1 \cdot \mathbf{J}_2 - \mathbf{H}_1 \cdot \mathbf{M}_2) d\mathbf{x} = \iint_S (\mathbf{E}_2 \cdot \mathbf{J}_1 - \mathbf{H}_2 \cdot \mathbf{M}_1) d\mathbf{x}$ describes the coupling between the fields $\mathbf{E}_1$ and $\mathbf{H}_1$ (produced by surface sources $\mathbf{M}_1$ and $\mathbf{J}_1$) on the surface sources $\mathbf{J}_2$ and $\mathbf{M}_2$ which produce $\mathbf{E}_2$ and $\mathbf{H}_2$.

Applying this to the expression of (A.11), we assign the magnetic current error induced by the truncation of the waveguide mode sum and spatial harmonics sum (i.e. $\mathbf{E}_{z=0^+} - \mathbf{E}_{z=0^-} \neq 0$) to $\mathbf{M}_1$ and the electric current error ($\mathbf{H}_{z=0^+} - \mathbf{H}_{z=0^-}$) to $\mathbf{J}_2$.

For an electric field discontinuity, a magnetic current is induced at the aperture surface, and can be written as $-(\mathbf{E}_{z=0^+} - \mathbf{E}_{z=0^-}) \times \hat{z}$. We surmise that this magnetic current may excite a magnetic field spatial harmonic, which takes the form $e^{\mathbf{u}_{\circ mn}\cdot\mathbf{x}}$ with a direction on the $x-y$ plane; since we require this magnetic current to excite an orthogonal magnetic field spatial harmonic (in the mathematical sense), we force $-\iint_C \mathbf{M}_1 \cdot \mathbf{H}_2 dxdy$ equal zero, thus the expression in (A.11).

Similarly, for the magnetic field discontinuity, we require that $-\iint_C \mathbf{J}_2 \cdot \mathbf{E}_1 dxdy$ equal zero ($\mathbf{E}_1$ takes the form of excited waveguide modes $\mathbf{e}_k$), thus

$$\iint_A \left\{ \hat{z} \times \left[Y_{\text{in}} V_0 \mathbf{e}_\circ(\mathbf{x}) - \sum_{i=1}^{N-1} Y_i V_i \mathbf{e}_i \right] - \sum_{\mathbf{u}_{\circ pq}} \mathbf{B}(\mathbf{u}_{\circ pq}) e^{-j\mathbf{u}_{\circ pq}\cdot\mathbf{x}} \right\} \times \hat{z} \cdot \mathbf{e}_k(\mathbf{x}) d\mathbf{x} = 0 \tag{A.13}$$

Enforcing the truncated the boundary conditions in (A.11) and (A.13) with a finite number, N, of waveguide modes, ensures that the difference between the right hand side and left hand side to be very small by, according to Borgiotti [49], *requiring them to be orthogonal to the subspaces spanned by the selected waveguide modes and spatial harmonics.* The effect of is that all the modes taken into account should each be fully taken into account such that the modes not included are the ones not incorporated into our active element admittance calculation. In other words, a selection of $N = 2$ would take include only two waveguide modes. The errors of the truncation would then all be pushed into the waveguide modes that are not taken into account. Picking $|p|_{\max} = |q|_{\max} = 2$ for the spatial harmonics, for instance, would push all the errors associated with the truncation into the spatial harmonic modes that are not taken into account. In essence, we have made our basis functions have physical meaning.

We must keep in mind that (A.11) and (A.13) each represent a set of equations.

We shall now proceed to derive the active element admittance, Y_{in}, by solving (A.11) and (A.13).

A.2 Solving for $\mathbf{A}(\mathbf{u}_{\circ pq})$ and $\mathbf{B}(\mathbf{u}_{\circ pq})$

We pick the direction of $\hat{q}$ in (A.11) to coincide with the direction of $-(\mathbf{E}_{z=0^+} - \mathbf{E}_{z=0^-}) \times \hat{z}$, thereby yielding,

$$\iint_A \left[\sum_{i=0}^{N-1} V_i \mathbf{e}_i(\mathbf{x}) e^{j\mathbf{u}_{\circ mn}\cdot\mathbf{x}} - \sum_{\mathbf{u}_{\circ pq}} \mathbf{A}(\mathbf{u}_{\circ pq}) e^{j(\mathbf{u}_{\circ mn}-\mathbf{u}_{\circ pq})\cdot\mathbf{x}} \right] d\mathbf{x} = 0 \tag{A.14}$$

Due to the orthogonality of the spatial harmonic basis functions, the second term of the integrand in (A.14) equals zero if $e^{\mathbf{u}_{\circ mn}} \neq e^{\mathbf{u}_{\circ pq}}$, and equal unity when $e^{\mathbf{u}_{\circ mn}} = e^{\mathbf{u}_{\circ pq}}$. Thus we further simplify (A.14) to:

$$\sum_{i=0}^{N-1} V_i \iint_A \left[\mathbf{e}_i(\mathbf{x}) e^{j\mathbf{u}_{\circ pq}\cdot\mathbf{x}} \right] d\mathbf{x} = \mathbf{A}(\mathbf{u}_{\circ pq}) C \tag{A.15}$$

Letting the Fourier transform of a waveguide mode field distribution $\mathbf{e}_i$ be represented by $\xi_i(\mathbf{u})$, where by definition $\xi_i(\mathbf{u}) = \frac{1}{2\pi} \iint_A \mathbf{e}_i(\mathbf{x}) e^{\mathbf{u}\cdot\mathbf{x}} d\mathbf{x}$, then (A.15) becomes

$$2\pi \sum_{i=0}^{N-1} V_i \xi_i(\mathbf{u}_{\circ pq}) = \mathbf{A}(\mathbf{u}_{\circ pq}) C \tag{A.16}$$

which can be re-arranged as:

$$\mathbf{A}(\mathbf{u}_{\circ pq}) = \frac{2\pi}{C} \sum_{i=0}^{N-1} V_i \xi_i(\mathbf{u}_{\circ pq}) \tag{A.17}$$

For a circular (or rectangular) waveguide, $\xi_i(u_{\circ pq})$ can be decomposed to radial and circumferential components and thus written as:

$$\xi_i(\mathbf{u}_{\circ pq}) = \xi_{i\rho}(\mathbf{u}_{\circ pq})\hat{\rho} + \xi_{i\psi}(\mathbf{u}_{\circ pq})\hat{\psi} \tag{A.18}$$

thereby enabling us to re-express (A.17) in the convenient form:

$$\mathbf{A}(\mathbf{u}_{\circ pq}) = \frac{2\pi}{C} \sum_{i=0}^{N-1} V_i [\xi_{i\rho}(\mathbf{u}_{\circ pq})\hat{\rho} + \xi_{i\psi}(\mathbf{u}_{\circ pq})\hat{\psi}] \tag{A.19}$$

Since $\mathbf{A}(\mathbf{u}_{\circ pq})$ represents electric field coefficients, we can relate it to the magnetic field coefficients in (A.11) and (A.9) by introducing the relevant spatial harmonics admittance parameters, yielding

$$\mathbf{B}(\mathbf{u}_{\circ pq}) = \frac{2\pi}{C} \sum_{i=0}^{N-1} V_i[-\xi_{i\psi}(\mathbf{u}_{\circ pq}) Y_{TE}(|\mathbf{u}_{\circ pq}|)\hat{\rho} + \xi_{i\rho}(\mathbf{u}_{\circ pq}) Y_{TM}(|\mathbf{u}_{\circ pq}|)\hat{\psi}] \quad \text{(A.20)}$$

Note that the first term of the addition is obtained from the inter-relationship between magnetic fields, transverse admittance, and perpendicular electric fields. In particular, the radial and circumferential components of the magnetic field are derived from that of the electric field, as in: $\mathrm{H}_\rho = -\mathrm{Y}_{TE}\mathrm{E}_\psi$, and $\mathrm{H}_\psi = \mathrm{Y}_{TM}\mathrm{E}_\rho$. A derivation of the transverse admittances Y_{TE} and Y_{TM} in the presence of dielectric or anisotropic layers can be obtained from Maxwell's equations as presented in Appendix B.

We have now expressed $\mathbf{A}(\mathbf{u}_{\circ pq})$ and $\mathbf{B}(\mathbf{u}_{\circ pq})$ in terms of the waveguide mode field distribution and spatial harmonic admittances.

A.3 Solving for Y_{in}

Rewriting (A.13), we obtain

$$\iint_A \left[Y_{\mathrm{in}} V_0 \mathbf{e}_\circ(\mathbf{x}) - \sum_{i=1}^{N-1} Y_i V_i \mathbf{e}_i \right] \cdot \mathbf{e}_k(\mathbf{x}) d\mathbf{x} = \sum_{\mathbf{u}_{\circ pq}} \mathbf{B}(\mathbf{u}_{\circ pq}) \times \hat{z} \iint_A e^{-j\mathbf{u}_{\circ pq}\cdot\mathbf{x}} \cdot \mathbf{e}_k(\mathbf{x}) d\mathbf{x} \quad \text{(A.21)}$$

Solving for the right hand side of (A.21), we can write

$$RHS = \sum_{\mathbf{u}_{\circ pq}} \mathbf{B}(\mathbf{u}_{\circ pq}) \times \hat{z}\xi_k(-\mathbf{u}_{\circ pq})$$

$$= 2\pi \sum_{\mathbf{u}_{\circ pq}} \mathbf{B}(\mathbf{u}_{\circ pq}) \times \hat{z}[\xi^*_{k\rho}(\mathbf{u}_{\circ pq})\hat{\rho} + \xi^*_{k\psi}(\mathbf{u}_{\circ pq})\hat{\psi}] \tag{A.22}$$

Substituting (A.20) into (A.22) and evaluating the cross-product yields

$$RHS = \frac{4\pi^2}{C} \sum_{\mathbf{u}_{\circ pq}} \sum_{i=0}^{N-1} V_i[\xi_{i\rho}(\mathbf{u}_{\circ pq})\xi^*_{k\rho}(\mathbf{u}_{\circ pq})Y_{TM}(|\mathbf{u}_{\circ pq}|) +$$

$$\xi_{i\psi}(\mathbf{u}_{\circ pq})\xi^*_{k\psi}(\mathbf{u}_{\circ pq})Y_{TE}(|\mathbf{u}_{\circ pq}|)] \tag{A.23}$$

If we define

$$Y_{ki}(\mathbf{u}_\circ) = \frac{4\pi^2}{C} \sum_{\mathbf{u}_{\circ pq}} [\xi_{i\rho}(\mathbf{u}_{\circ pq})\xi^*_{k\rho}(\mathbf{u}_{\circ pq})Y_{TM}(|\mathbf{u}_{\circ pq}|) +$$

$$\xi_{i\psi}(\mathbf{u}_{\circ pq})\xi^*_{k\psi}(\mathbf{u}_{\circ pq})Y_{TE}(|\mathbf{u}_{\circ pq}|)] \tag{A.24}$$

then we may rewrite (A.23) as

$$RHS = \sum_{i=0}^{N-1} V_i Y_{ki}(\mathbf{u}_\circ) \tag{A.25}$$

We shall now solve for the left hand side of (A.21)

$$LHS = Y_{\text{in}} V_0 \iint_A \mathbf{e}_\circ(\mathbf{x}) \cdot \mathbf{e}_k(\mathbf{x}) d\mathbf{x} - \sum_{i=1}^{N-1} Y_i V_i \iint_A \mathbf{e}_i(\mathbf{x}) \cdot \mathbf{e}_k(\mathbf{x}) d\mathbf{x} \tag{A.26}$$

The results of (A.26) differ depending on the value of k. There are two cases: (i) $k = 0$, and (ii) $k = i$.

Case 1: When $k = 0$, the integrand of the first integral goes to one, while the second integral goes to zero ($k = 0$ requires $i = 0$ for a nonzero result, but i begins from 1), yielding:

$$\text{Case 1:} \quad LHS = Y_{\text{in}} V_0 \tag{A.27}$$

Case 2: For $k \neq 0$, the first integral in (A.26) is zero, but since i must equal k for (A.26) to be nonzero, we evaluate for $i = k$, yielding:

$$\text{Case 2:} \quad LHS = -Y_k V_k \tag{A.28}$$

Equating the right hand side [see (A.25)] to the left hand side [see (A.27) and (A.28)], we obtain the set of simultaneous equations:

$$\begin{aligned} Y_{\text{in}} V_0 - \sum_{i=0}^{N-1} V_i Y_{0i}(\mathbf{u}_\circ) = 0 \\ Y_k V_k + \sum_{i=0}^{N-1} V_i Y_{ki}(\mathbf{u}_\circ) = 0 \end{aligned} \tag{A.29}$$

From these equations the active element admittance, Y_{in} may be estimated. An application of this formulation is done in Section 2.2.2 of Chapter 2.

A.4 General Expressions for the Fourier Transform of Circular Waveguide Modes

From [49], the Fourier transform of the field distribution of a TE_{mn} circular waveguide mode, in cylindrical coordinates is:

$$\xi_\rho(\mathbf{k}_t) = m j^{(m-1)} \frac{\sqrt{2/\pi}}{\sqrt{(x'_{mn})^2 - m^2}} \cdot \frac{\sin m\gamma}{|\mathbf{k}_t|} J_m(r|\mathbf{k}_t|) \tag{A.30}$$

$$\xi_{\psi}(\mathbf{k}_t) = j^{(m-1)} \frac{\sqrt{2/\pi}}{\sqrt{(x'_{mn})^2 - m^2}} \cdot \frac{a \cos m\gamma}{1 - (\frac{a|\mathbf{k}_t|}{x_{mn}})^2} \cdot J'_m(a|\mathbf{k}_t|) \tag{A.31}$$

and for TM_{mn} circular waveguide modes, the Fourier transforms in cylindrical coordinates are:

$$\xi_{\rho}(\mathbf{k}_t) = -j^{(m-1)} \sin m\gamma \frac{|\mathbf{k}_t|\sqrt{2/\pi}}{(\frac{x_{mn}}{a})^2 - |\mathbf{k}_t|^2} J_m(r|\mathbf{k}_t|) \tag{A.32}$$

$$\xi_{\psi}(\mathbf{k}_t) = 0 \tag{A.33}$$

Where,

$$\cos m\gamma = \mathrm{Re}\left[\left(\frac{\hat{x} \cdot \mathbf{k}_t + \hat{y} \cdot j\mathbf{k}_t}{|\mathbf{k}_t|}\right)^m\right] \tag{A.34}$$

$$\sin m\gamma = \mathrm{Im}\left[\left(\frac{\hat{x} \cdot \mathbf{k}_t + \hat{y} \cdot j\mathbf{k}_t}{|\mathbf{k}_t|}\right)^m\right] \tag{A.35}$$

For cross-polarized TE_{mn} modes or TM_{mn}, $\sin m\gamma$ and $cosm\gamma$ are instead:

$$\text{Cross-polarized modes:} \quad \cos m\gamma = \mathrm{Re}\left[\left(\frac{\hat{x} \cdot \mathbf{k}_t + \hat{y} \cdot j\mathbf{k}_t}{|\mathbf{k}_t|}\right)^m e^{j\frac{180^\circ}{2m}}\right] \tag{A.36}$$

$$\sin m\gamma = \mathrm{Im}\left[\left(\frac{\hat{x} \cdot \mathbf{k}_t + \hat{y} \cdot j\mathbf{k}_t}{|\mathbf{k}_t|}\right)^m e^{j\frac{180^\circ}{2m}}\right] \tag{A.37}$$

Note that x_{mn} and x'_{mn} represent the n^{th} root of Bessel functions J_m and J'_m. $\mathbf{k}_t$ is the effective transverse wavenumber at the surface of the waveguide array.

Appendix B

Derivation of the Admittance of Plane Wave Modes in Anisotropic Media

From Maxwell's equations,

$$\begin{aligned}
\frac{\partial E_z}{\partial y} - \frac{\partial E_y}{\partial z} &= -\mu_\circ \mu_x \frac{\partial H_x}{\partial t} & \qquad \frac{\partial H_z}{\partial y} - \frac{\partial H_y}{\partial z} &= \epsilon_\circ \epsilon_x \frac{\partial E_x}{\partial t} \\
\frac{\partial E_x}{\partial z} - \frac{\partial E_z}{\partial x} &= -\mu_\circ \mu_y \frac{\partial H_y}{\partial t} & \qquad \frac{\partial H_x}{\partial z} - \frac{\partial H_z}{\partial x} &= \epsilon_\circ \epsilon_y \frac{\partial E_y}{\partial t} \\
\frac{\partial E_y}{\partial x} - \frac{\partial E_x}{\partial y} &= -\mu_\circ \mu_z \frac{\partial H_z}{\partial t} & \qquad \frac{\partial H_y}{\partial x} - \frac{\partial H_x}{\partial y} &= \epsilon_\circ \epsilon_z \frac{\partial E_z}{\partial t}
\end{aligned} \tag{B.1}$$

B.1 TM-polarized wave

For a TM-polarized wave propagating on the $x - z$ plane of incidence, only E_x, E_z and H_y exist, while $\frac{\partial}{\partial y} = 0$; thus (B.1) reduces to the following:

$$\frac{\partial E_x}{\partial z} - \frac{\partial E_z}{\partial x} = \mu_\circ \mu_y \frac{\partial H_y}{\partial t}$$
$$-\frac{\partial H_y}{\partial z} = \epsilon_\circ \epsilon_x \frac{\partial E_x}{\partial t}$$
$$\frac{\partial H_y}{\partial x} = \epsilon_\circ \epsilon_z \frac{\partial E_z}{\partial t} \tag{B.2}$$

all of which can be rewritten as:

$$-jk_z E_x + jk_x E_z = -j\omega\mu_\circ \mu_y H_y$$
$$jk_z H_y = j\omega\epsilon_\circ \epsilon_x E_x$$
$$-jk_x H_y = j\omega\epsilon_\circ \epsilon_z E_z \tag{B.3}$$

Plugging in the third equation of (B.3) into the second, yields:

$$k_z E_x + \frac{k_x^2 H_y}{\omega\epsilon_\circ \epsilon_z} = \omega\mu\mu_y H_y \tag{B.4}$$

By combining (B.4) and the second equation of (B.3), the dispersion relation below is obtained,

$$\frac{k_z^2}{\omega\epsilon_\circ \epsilon_x} + \frac{k_x^2}{\omega\epsilon_\circ \epsilon_z} - \omega\mu_\circ \mu_y = 0 \tag{B.5}$$

and solving for k_z from (B.5) yields:

$$k_z = \sqrt{\omega^2 \epsilon_\circ \mu_\circ \epsilon_x \mu_y - \frac{\epsilon_x k_x^2}{\epsilon_z}} \tag{B.6}$$

From (B.3), the transverse admittance of a plane propagating within a half space of an anisotropic media is realized.

$$Y_{\mathrm{TM}} = \frac{H_y}{E_x} = \frac{\omega\epsilon_\circ\epsilon_x}{k_z} = \left[\sqrt{\frac{\mu_\circ\mu_y}{\epsilon_\circ\epsilon_x} - \frac{k_x^2}{\omega^2\epsilon_\circ^2\epsilon_x\epsilon_z}}\right]^{-1} \tag{B.7}$$

Similarly, the transverse admittance for a TM-polarized plane wave mode in an isotropic dielectric medium is:

$$Y_{\mathrm{TM}} = \frac{H_y}{E_x} = \frac{\omega\epsilon_\circ\epsilon_r}{k_z} = \left[\sqrt{\frac{\mu_\circ}{\epsilon_\circ\epsilon_r} - \frac{k_x^2}{\omega^2\epsilon_\circ^2\epsilon_r^2}}\right]^{-1} \tag{B.8}$$

B.2 TE-polarized wave

For a TE-polarized wave propagating on the $x-z$ plane of incidence, only H_x, H_z and E_y exist, while $\frac{\partial}{\partial y} = 0$; thus (B.1) reduces to the following:

$$\begin{aligned} -\frac{\partial E_y}{\partial z} &= -\mu_\circ\mu_x\frac{\partial H_x}{\partial t} \\ \frac{\partial H_x}{\partial z} - \frac{\partial H_z}{\partial x} &= \epsilon_\circ\epsilon_y\frac{\partial E_y}{\partial t} \\ \frac{\partial E_y}{\partial x} &= -\mu_\circ\mu_z\frac{\partial H_z}{\partial t} \end{aligned} \tag{B.9}$$

all of which can be rewritten as:

$$\begin{aligned} k_x E_y &= -\omega\mu_\circ\mu_x H_x \\ -k_z H_x + k_x H_z &= \omega\epsilon_\circ\epsilon_y E_y \\ k_x E_y &= \omega\mu_\circ\mu_z H_z \end{aligned} \tag{B.10}$$

We then obtain the dispersion relation for TE-polarized plane waves as:

$$\frac{k_z^2}{\omega\mu_\circ\mu_x} + \frac{k_x^2}{\omega\mu_\circ\mu_z} - \omega\epsilon_\circ\epsilon_y = 0 \tag{B.11}$$

From (B.10), k_z is obtained to be:

$$k_z = \sqrt{\omega^2 \mu_\circ \epsilon_\circ \mu_x \epsilon_y - \frac{\mu_x k_x^2}{\mu_z}} \tag{B.12}$$

and $\mathrm{Y_{TE}}$ as,

$$Y_{\mathrm{TE}} = \frac{-H_x}{E_y} = \frac{k_z}{\omega \mu_\circ \mu_x} = \sqrt{\frac{\epsilon_\circ \epsilon_y}{\mu_\circ \mu_x} - \frac{k_x^2}{\omega^2 \mu_\circ^2 \mu_x \mu_z}} \tag{B.13}$$

Similarly, the transverse admittance for a TE-polarized plane wave mode in an isotropic dielectric medium is:

$$Y_{\mathrm{TE}} = \frac{-H_x}{E_y} = \frac{k_z}{\omega \mu_\circ} = \sqrt{\frac{\epsilon_\circ \epsilon_r}{\mu_\circ} - \frac{k_x^2}{\omega^2 \mu_\circ^2}} \tag{B.14}$$

Bibliography

[1] B. J. Justice, J. J. Mock, L. Guo, A. Degiron, D. Schurig, and D.R. Smith. Spatial mapping of the internal and external electromagnetic fields of negative index metamaterials. *Optics Express*, 14(19), Sept. 2006.

[2] Ruopeng Liu, Qiang Cheng, Thomas Hand, Jack J. Mock, Tie Jun Cui, Steven A. Cummer, and David R. Smith. Experimental demonstration of electromagnetic tunneling through an epsilon-near-zero metamaterial at microwave frequencies. *Phys. Rev. Lett.*, 100(2):023903, Jan 2008.

[3] Ruopeng Liu, Qiang Cheng, Jessie Y. Chin, Jack J. Mock, Tie Jun Cui, and David R. Smith. Broadband gradient index microwave quasi-optical elements based on non-resonant metamaterials. *Opt. Express*, 17(23):21030–21041, 2009.

[4] Jensen Li and J. B. Pendry. Hiding under the carpet: A new strategy for cloaking. *Phys. Rev. Lett.*, 101(20):203901, Nov 2008.

[5] R. Liu, C. Ji, J. J. Mock, J. Y. Chin, T. J. Cui, and D. R. Smith. Broadband Ground-Plane Cloak. *Science*, 323(5912):366–369, 2009.

[6] L. Parad. The input admittance to a slotted array with or without a dielectric sheet. *Antennas and Propagation, IEEE Transactions on [legacy, pre - 1988]*, 15(2):302–304, Mar 1967.

[7] D. R. Smith, S. Schultz, P. Markoš, and C. M. Soukoulis. Determination of effective permittivity and permeability of metamaterials from reflection and transmission coefficients. *Phys. Rev. B*, 65(19):195104, Apr 2002.

[8] D. Schurig, J. J. Mock, and D. R. Smith. Electric-field-coupled resonators for negative permittivity metamaterials. *Applied Physics Letters*, 88(4):041109, 2006.

[9] J. F. O'Hara, E. Smirnova, H. Chen, A. J. Taylor, R. D. Averitt, C. Highstrete, M. Lee, and W. J. Padilla. Properties of planar electric metamaterials for novel

terahertz applications. *Journal of Nanoelectronics and Optoelectronics*, 2(1):90–95, Apr 2007.

[10] S. Sajuyigbe, B. J. Justice, A. F. Starr, and D. R. Smith. Design and analysis of three-dimensionalized elc metamaterial unit cell. *Antennas and Wireless Propagation Letters, IEEE*, 8:1268–1271, 2009.

[11] Thomas H. Hand, Jonah Gollub, Soji Sajuyigbe, David R. Smith, and Steven A. Cummer. Characterization of complementary electric field coupled resonant surfaces. *Applied Physics Letters*, 93(21):212504, 2008.

[12] Constantine A. Balanis. *Advanced Engineering Electromagnetics*. John Wiley & Sons, 1989.

[13] Willie J. Padilla, Dimitry N. Basov, and David R. Smith. Negative index metamaterials. *Materials Today*, 9(7-8), July-August 2006.

[14] J.B. Pendry, A.J. Holden, D.J. Robbins, and W.J. Stewart. Magnetism from conductors and enhanced nonlinear phenomena. *Microwave Theory and Techniques, IEEE Transactions on*, 47(11):2075–2084, Nov. 1999.

[15] J. B. Pendry, A. J. Holden, W.J. Stewart, and I. Youngs. Extremely low frequency plasmons in metallic microstructures. *Phys. Rev. Lett.*, 76:4773–6, 1996.

[16] R. A. Shelby, D. R. Smith, and S. Schultz. Experimental Verification of a Negative Index of Refraction. *Science*, 292(5514):77–79, 2001.

[17] V. G. Veselago. The electrodynamics of substances with simultaneously negative values of ϵ and μ. *(also in Russian, Usp. Fiz. Nauk., vol. 92, pp. 517- 526, 1967), Soviet Phys. Uspekhi*, 10(4):509–514, 1968.

[18] Ruopeng Liu, Aloyse Degiron, Jack J. Mock, and David R. Smith. Negative index material composed of electric and magnetic resonators. *Applied Physics Letters*, 90(26):263504, 2007.

[19] D. R. Smith, Willie J. Padilla, D. C. Vier, S. C. Nemat-Nasser, and S. Schultz. Composite medium with simultaneously negative permeability and permittivity. *Phys. Rev. Lett.*, 84(18), 2000.

[20] David R. Smith and Normal Kroll. Negative refractive index in left-handed metamaterials. *Phys. Rev. Lett.*, 85(14), 2000.

[21] Steven A. Cummer and Bogdan-Ioan Popa. Wave fields measured inside a negative refratrive index metamaterial. *Appl. Phys. Lett.*, 85(20), 2004.

[22] Mário Silveirinha and Nader Engheta. Tunneling of electromagnetic energy through subwavelength channels and bends using ϵ-near-zero materials. *Phys. Rev. Lett.*, 97(15):157403, Oct 2006.

[23] D. Schurig, J. J. Mock, B. J. Justice, S. A. Cummer, J. B. Pendry, A. F. Starr, and D. R. Smith. Metamaterial Electromagnetic Cloak at Microwave Frequencies. *Science*, 314(5801):977–980, 2006.

[24] D. Schurig, J. J. Mock, B. J. Justice, S. A. Cummer, J. B. Pendry, A. F. Starr, and D. R. Smith. Metamaterial Electromagnetic Cloak at Microwave Frequencies. *Science*, 314(5801):977–980, 2006.

[25] Bogdan-Ioan Popa, Jeffery Allen, and Steven A. Cummer. Conformal array design with transformation electromagnetics. *Applied Physics Letters*, 94(24):244102, 2009.

[26] Marco Rahm, David Schurig, Daniel A. Roberts, Steven A. Cummer, David R. Smith, and John B. Pendry. Design of electromagnetic cloaks and concentrators using form-invariant coordinate transformations of maxwell's equations. *FUNDAM.APPLIC.*, 6:87, 2008.

[27] Jeffery Allen, Nathan Kundtz, Daniel A. Roberts, Steven A. Cummer, and David R. Smith. Electromagnetic source transformations using superellipse equations. *Applied Physics Letters*, 94(19):194101, 2009.

[28] N. Kundtz, D. A. Roberts, J. Allen, S. Cummer, and D. R. Smith. Optical source transformations. *Opt. Express*, 16(26):21215–21222, 2008.

[29] D. A. Roberts, N. Kundtz, and D. R. Smith. Optical lens compression via transformation optics. *Opt. Express*, 17(19):16535–16542, 2009.

[30] D. R. Smith, J. J. Mock, A. F. Starr, and D. Schurig. Gradient index metamaterials. *Physical Review E (Statistical, Nonlinear, and Soft Matter Physics)*, 71(3):036609, 2005.

[31] J. B. Pendry, D. Schurig, and D. R. Smith. Controlling Electromagnetic Fields. *Science*, 312(5781):1780–1782, 2006.

[32] Marco Rahm, Steven A. Cummer, David Schurig, John B. Pendry, and David R. Smith. Optical design of reflectionless complex media by finite embedded coordinate transformations. *Phys. Rev. Lett.*, 100(6):063903, Feb 2008.

[33] Marco Rahm, David Schurig, Daniel A. Roberts, Steven A. Cummer, David R. Smith, and John B. Pendry. Design of electromagnetic cloaks and concentrators using form-invariant coordinate transformations of maxwell's equations. *Photonics and Nanostructures - Fundamentals and Applications*, 6(1):87 – 95, 2008. The Seventh International Symposium on Photonic and Electromagnetic Crystal Structures - PECS-VII.

[34] Andrea Alù and Nader Engheta. Multifrequency optical invisibility cloak with layered plasmonic shells. *Phys. Rev. Lett.*, 100(11):113901, Mar 2008.

[35] Jason Valentine, Jensen Li, Thomas Zentgraf, Guy Bartal, and Xiang Zhang. An optical cloak made of dielectrics. *Nature Materials*, 8:568–571, Apr 2009.

[36] Nathan Kundtz and David R. Smith. Extreme-angle broadband metamaterial lens. *Nature Materials*, 9:129–132, 2010.

[37] Jr. Farrell, G. and D. Kuhn. Mutual coupling in infinite planar arrays of rectangular waveguide horns. *Antennas and Propagation, IEEE Transactions on [legacy, pre - 1988]*, 16(4):405–414, Jul 1968.

[38] B. Diamond. Resonance phenomena in waveguide arrays. In *Antennas and Propagation Society International Symposium, 1967*, volume 5, pages 110–115, Oct 1967.

[39] E. Magill and H. Wheeler. Wide-angle impedance matching of a planar array antenna by a dielectric sheet. *Antennas and Propagation, IEEE Transactions on [legacy, pre - 1988]*, 14(1):49–53, Jan 1966.

[40] K. Siwiak, T. Dowling, and L. Lewis. Boresight errors induced by missile radomes. *Antennas and Propagation, IEEE Transactions on*, 27(6):832–841, Nov 1979.

[41] Shung-Wu Lee, M. Sheshadri, V. Jamnejad, and R. Mittra. Wave transmission through a spherical dielectric shell. *Antennas and Propagation, IEEE Transactions on*, 30(3):373–380, May 1982.

[42] Louis Stark. Microwave theory of phased-array antennas-a review. *Proceedings of the IEEE*, 62(12):1661–1701, December 1974.

[43] H. Wheeler. The grating-lobe series for the impedance variation in a planar phased-array antenna. *Antennas and Propagation, IEEE Transactions on [legacy, pre - 1988]*, 14(6):707–714, Nov 1966.

[44] A. Fenn, G. Thiele, and B. Munk. Moment method analysis of finite rectangular waveguide phased arrays. *Antennas and Propagation, IEEE Transactions on*, 30(4):554–564, Jul 1982.

[45] C.P. Wu N. Amitay, V. Galindo. *Theory and Analysis of Phased Array Antennas*. Wiley Interscience, 1972.

[46] Robert J. Mailloux. *Phased Array Antenna Handbook*. Artech House, 2nd edition, 2005.

[47] L. Stark. Radiation impedance of a dipole in an infinite planar phased array. *Radio Sci.*, 3:361–375, 1966.

[48] Ben A. Munk. *Finite Antenna Arrays and FSS*. Wiley Interscience, 1st edition, 2003.

[49] G.V. Borgiotti. Modal analysis of periodic planar phased arrays of apertures. *Proceedings of the IEEE*, 56(11):1881–1892, Nov. 1968.

[50] Max Born and Emil Wolf. *Principles of Optics*. Cambridge University Press, 7th (expanded) edition, 1999.

[51] D. R. Smith, D. C. Vier, Th. Koschny, and C. M. Soukoulis. Electromagnetic parameter retrieval from inhomogeneous metamaterials. *Phys. Rev. E*, 71(3):036617, Mar 2005.

[52] D. R. Smith and D. Schurig. Electromagnetic wave propagation in media with indefinite permittivity and permeability tensors. *Phys. Rev. Lett.*, 90(7):077405, Feb 2003.

[53] Liangbin Hu and S. T. Chui. Characteristics of electromagnetic wave propagation in uniaxially anisotropic left-handed materials. *Phys. Rev. B*, 66(8):085108, Aug 2002.

[54] G. Borgiotti. Radiation and reactive energy of aperture antennas. *Antennas and Propagation, IEEE Transactions on [legacy, pre - 1988]*, 11(1):94–95, Jan 1963.

[55] Ben A. Munk. *Frequency Selective Surfaces*. Wiley Interscience, 1st edition, 2000.

[56] Ricardo Marqués, Francisco Medina, and Rachid Rafii-El-Idrissi. Role of bianisotropy in negative permeability and left-handed metamaterials. *Phys. Rev. B*, 65(14):144440, Apr 2002.

[57] J. B. Pendry. Negative refraction makes a perfect lens. *Phys. Rev. Lett.*, 85(18):3966–3969, Oct 2000.

[58] J. D. Baena, L. Jelinek, R. Marqués, and J. Zehentner. Electrically small isotropic three-dimensional magnetic resonators for metamaterial design. *Applied Physics Letters*, 88(13):134108, 2006.

[59] M.G. Silveirinha and C.A. Fernandes. Homogenization of 3-d-connected and nonconnected wire metamaterials. *Microwave Theory and Techniques, IEEE Transactions on*, 53(4):1418–1430, April 2005.

[60] A. F. Starr, P. M. Rye, D. R. Smith, and S. Nemat-Nasser. Fabrication and characterization of a negative-refractive-index composite metamaterial. *Phys. Rev. B*, 70(11):113102, Sep 2004.

[61] D. Schurig. Off-normal incidence simulations of metamaterials using fdtd. *International Journal of Numerical Modelling: Electronic Networks, Devices and Fields*, 19(2):215–228, 2006.

[62] Philippe Gay-Balmaz and Olivier J. F. Martin. Efficient isotropic magnetic resonators. *Applied Physics Letters*, 81(5):939–941, 2002.

[63] A.A. Kishk R. Chair and K.F. Lee. Experimental investigation for wideband perforated dielectric resonator antenna. *IEEE Electronics Letters*, 33(6), February 2006.

[64] A. Alu and N. Engheta. Pairing an epsilon-negative slab with a mu-negative slab: resonance, tunneling and transparency. *Antennas and Propagation, IEEE Transactions on*, 51(10):2558–2571, Oct. 2003.

[65] G. Borgiotti and Q. Balzano. Modal analysis of an infinite periodic phased array of circular apertures. In *Antennas and Propagation Society International Symposium, 1968*, volume 6, pages 142–150, Sep 1968.

[66] Eli Brookner. *Microwave Journal*, 49(1):24–46, 2006.

[67] G.V. Eleftheriades, A.K. Iyer, and P.C. Kremer. Planar negative refractive index media using periodically l-c loaded transmission lines. *Microwave Theory and Techniques, IEEE Transactions on*, 50(12):2702–2712, Dec 2002.

[68] A. Lai, T. Itoh, and C. Caloz. Composite right/left-handed transmission line metamaterials. *Microwave Magazine, IEEE*, 5(3):34–50, Sept. 2004.

[69] Maria Lanne. An analysis of a finite array using infinite array data. Technical report, Chalmers University of Technology, Ericsson Microwave Systems AB.

[70] Stanislav Maslovski and Sergei Tretyakov. Phase conjugation and perfect lensing. *Journal of Applied Physics*, 94(7):4241–4243, 2003.

[71] David M. Pozar. *Microwave Engineering*. Wiley Publishers, 3rd edition, 2005.

[72] R. A. Shelby, D. R. Smith, S. C. Nemat-Nasser, and S. Schultz. Microwave transmission through a two-dimensional, isotropic, left-handed metamaterial. *Appl. Phys. Lett.*, 78(4), 2001.

[73] Schultz Et. Al. Radome compensation using matched negative index or refraction materials. *United States Patent, 6,788,273*, Sept 7 2004.

[74] D. R. Smith, Willie J. Padilla, D. C. Vier, S. C. Nemat-Nasser, and S. Schultz. Composite medium with simultaneously negative permeability and permittivity. *Phys. Rev. Lett.*, 84(18):4184–4187, May 2000.

[75] D. R. Smith, D. C. Vier, N. Kroll, and S. Schultz. Direct calculation of permeability and permittivity for a left-handed metamaterial. *Appl. Phys. Lett.*, 77(14), 2000.

[76] V. G. Veselago. Electrodynamics of materials with negative index of refraction. *PHYS-USP*, 46(7):764–768, 2003.

[77] D. Schurig. Off-normal incidence simulations of metamaterials using fdtd. *International Journal of Numerical Modelling: Electronic Networks, Devices and Fields*, 19(2):215–228, 2006.

Biography

Adésọjí Ṣájuyìgbé was born and lived his first $17\frac{1}{2}$ years of life in Lagos (Nigeria), a city-state situated on the shores of the West African end of the Atlantic Ocean. He spent his six years of primary education at Olúwákẹmi Nursery and Primary School in the Ọgbà suburbs of Lagos from 1986-1992. Between 1992-1998, he went to secondary school on the outskirts of Lagos at Government College Kétu, a public boarding school near the lagoon fishing town of Èpé, where he completed his junior secondary (JS) and senior secondary (SS) stints, three years each. For the next year and half, he took short courses and ventured into taking the SAT and TOEFL after an initial coincidence of events. He began college in 2000 at Abilene Christian University, Abilene, TX, majoring in Pre-Enginering, and in 2001 transfered to San Jose State University, San Jose, CA, where in 2005 he obtained the B.S. degree in Electrical Engineering, having been lured away from the kind collegial atmosphere of Abilene by the allure of Silicon Valley technology and fancy. He moved in 2005 to Duke University in Durham, NC, for graduate studies, earning in 2007 the M.S. degree, and in 2010 the Ph.D. degree, both in Electrical Engineering.

Following is a list of his academic publications:

Gollub, J.; Hand T. H.; Sajuyigbe, S.; Mendonca, S.; Cummer, S. and Smith D.R. "Characterizing the effects of disorder in metamaterial structures," *Applied Physics Letters* , 91, 162907 (2007)

Landy, N.I.; Sajuyigbe, S.; Mock J.J.; Smith, D.R.; Padilla W.J.; , "Perfect Metamaterial Absorber," *Physical Review Letters* , 100, 207402 (2008)

Hand T. H.; Gollub, J.; Sajuyigbe, S.; Smith D.R.; and Cummer, S. A.; , "Characterization of complementary electric field coupled resonant surfaces," *Applied Physics Letters* , 93, 212504 (2008)

Sajuyigbe, S.; Cummer, S.A.; Smith, D.R.; , "Utilization of metamaterials for wide angle impedance matching (WAIM) in phased array antennas," *Antennas and Propagation Society International Symposium, 2009. APSURSI '09. IEEE* , vol., no., pp.1-4, 1-5 June 2009

Sajuyigbe, S.; Ross, M.; Geren, P.; Cummer, S.A.; Tanielian, M. H.;Smith, D.R., "Wide Angle Impedance Matching of Phased Array Antennas, using Metamaterials," Submitted to *IET Microwaves, Antennas and Propagation*, 2009

Sajuyigbe, S.; Lam, T. A.; Tanielian, M. H.; Smith, D.R.; "Experimental Characterization of Phased Array Antenna with a Metamaterial Matching Layer," Submitted to *Antennas and Wireless Propagation Letters, IEEE*, 2010

Sajuyigbe, S.; Justice, B.J.; Starr, A.F.; Smith, D.R.; , "Design and Analysis of Three-Dimensionalized ELC Metamaterial Unit Cell," *Antennas and Wireless Propagation Letters, IEEE* , vol.8, no., pp.1268-1271, 2009

Sajuyigbe, S.; Justice, B.J.; Starr, A.F.; Overfelt, P. L.; Smith, D.R.; , "Experimental Characterization of Metamaterial Composite with Embedded Three-Dimensionalized ELC Inclusions," Submitted to *Antennas and Wireless Propagation Letters, IEEE*,

2010